RICE UNIVERSITY

Complex Plasmonic Nanostructures: Symmetry Breaking and Coupled Systems

by

J. Britt Lassiter

A THESIS SUBMITTED
IN PARTIAL FULLFILLMENT OF THE
REQUIREMENTS FOR THE DEGREE

Doctor of Philosophy

APPROVED, THESIS COMMITTEE:

Naomi J. Halas (Director)
Stanley C. Moore Professor of Electrical and Computer Engineering
Professor of Physics and Astronomy

Jason H. Hafner (Chair)
Associate Professor of Physics and Astronomy
Associate Professor of Chemistry

Douglas Natelson
Professor of Physics and Astronomy
Professor of Electrical and Computer Engineering

Bruce R. Johnson
Distinguished Faculty Fellow in Chemistry

HOUSTON, TEXAS
MAY 2012

Abstract

Complex Plasmonic Nanostructures:

Symmetry Breaking and Coupled Systems

By

J. Britt Lassiter

Metallic nanostructures support resonant oscillations of their conduction band electrons called localized surface plasmon resonances. Plasmons couple efficiently to light and have enabled a new class of technology for the manipulation of light at the nanoscale. Nanostructures that support plasmon resonances have the potential for a wide range of applications such as enhanced optical spectroscopy techniques for chemical- and bio-sensing, cancer diagnosis and therapy, metamaterials, and energy harvesting. As the field of plasmonics has progressed, these applications have become more sophisticated, requiring increasingly complex nanostructures. For example, coupled nanostructures of two or more nanoparticles are used extensively in plasmon-enhanced spectroscopy techniques because they exhibit extremely large optical field enhancements. Asymmetric nanostructures, such as nanocups (metallic semishells), have been shown to support magnetic modes that could be used in metamaterials applications. This class of complex plasmonic nanostructures holds great potential for both the observation of new physical phenomena and practical applications.

This thesis will focus on the fabrication and characterization of several examples of these complex nanostructures using darkfield spectroscopy. The plasmon modes of a dimer consisting of two nanoshells are investigated in both the separated and

conductively overlapping regimes and are interpreted using the plasmon hybridization model. Next, coupled nanoclusters of seven particles arranged in a hexagonal pattern are studied. It is found that these nanoclusters support Fano resonances due to the coupling and interference of degenerate subradiant and superradiant plasmon modes. These structures are found to have an extremely high sensitivity to the local dielectric environment, making them attractive for biosensing applications. Variations on the nanocluster geometry are then explored, and it is observed that by adding more particles and varying their sizes, the lineshape of the Fano resonance can be precisely engineered. The underlying subradiant and superradiant modes are then analyzed using cathodoluminescence imaging and spectroscopy. Finally the plasmon modes of asymmetric nanostructures are measured. Nanoeggs (nanoshells with an offset core) and nanocups (metallic semishells) are fabricated by electron beam induced ablation, and their plasmon modes are measured. The plasmon modes of nanocups are studied in detail, and nanocups are found to support both electric and magnetic plasmons.

Dedication

In Loving Memory of My Mother

Gale Britt Lassiter

1954 - 2009

Acknowledgements

I would like to express my deep gratitude to everyone who has helped me throughout my time in graduate school. First, I wish to thank Professor Naomi Halas, my advisor, for her support and mentorship. Dr. Halas has a wealth of ideas and insights both concerning science and how to conduct science. She has taught me how to formulate new and creative ideas, how to pursue them, and when to abandon bad ideas. She has taught me how to be a professional researcher, from effective writing and presentation skills to self-assessment and career development. Dr. Halas's style of mentorship and the culture of her research group has been a perfect fit for me, and I do not think I could have been nearly as successful in any other research group.

I must also thank all of the Halas group members with whom I have worked, past and present: Ciceron Ayala-Orozco, Rizia Bardhan, Aoune Barhoumi, Austin Baty, Sandra Bishnoi, Bruce Brinson, Lisa Brown, Allen Chen, Joe Cole, Jared Day, Jeremy Dumoit, Zheyu Fang, Tumasang Fofang, Muhammed Gheith, Serge Grabtchak, Nate Grady, Mel Hainey, Ivan Hernandez, Ryan Huschka, Amanda Jones, Nick King, Mark Knight, Janardan Kundu, Surbhi Lal, Laura Liu, Carly Levin, Zaw Lwin, Michael McClain, Nikolay Mirin, Shaunak Mukherjee, Oara Neumann, Andie Schlather, Ali Sobhani, Priya Sundararajan, Felicia Tam, Christyn Thibodeaux, Alexander Urban, Hui Wang, Zhipeng Wang, Fangfang Wen, Joe Young, Jian Ye, Bob Zhang, Dongmao Zhang, and Yu Zhang. Although they may not all realize it, I have learned something from each person on this list and each has helped me along the way.

I would also like to thank my physics department advisor, Professor Jason Hafner. For my first several years in graduate school, the majority of my spectroscopy

experiments were performed in Dr. Hafner's lab using his equipment. As a result, he answered the majority of my experimental questions during my first few years of graduate school. I am extremely grateful to Dr. Hafner for the opportunity to work in his lab. His patience and insight was truly critical in my development as a scientist. I must also thank all of Dr. Hafner's group members, and especially Colleen Nehl, for their experimental assistance and for their patience as I sometimes used their equipment for extended time periods.

I would also like to thank Professor Peter Nordlander. Dr. Nordlander is largely responsible for first piquing my interest in the field of plasmonics and nanophotonics. I had originally come to Rice intending to pursue an entirely different field, but was first persuaded to change by his "brown bag" lunch presentation that he gave to first year students. He and I have had innumerable discussions, and he has provided countless suggestions and insights that have drastically improved my research. Dr. Nordlander constantly approaches problems from a completely different point of view than my own and has taught me a great deal about how to think about physics. I have received help from Dr. Nordlander on virtually every project that I have worked on during graduate school. I have collaborated with Dr. Nordlander's group extensively as well, and I must thank each member of his group, but especially Daniel Brandl, Kui Bao, Tae-Ho Park, Heidar Sobhani, and Yanpeng Wu.

I would also like to thank my committee members, Professors Doug Natelson and Bruce Johnson. I am grateful to them for serving on my committee and for the many great research discussions I have had with them. I would also like to thank several other professors at Rice and other universities with whom I have collaborated during graduate

school: Professor Stephan Link, Professor Javier Aizpurua, Professor Federico Capasso, and Professor Dai-Sik Kim.

Finally, I wish to thank my wife and family. My mother, father, and sister have been extremely supportive of me as I have pursued a science career, and I cannot thank them enough for the encouragement and moral support they have provided. My wife has supported me from day one. She has constantly encouraged me and gives me the strength to do things that I would not be able to accomplish without her.

Table of Contents

List of Figures

Chapter 1: Introduction

The field of plasmonics has rapidly expanded over the previous decade, driven by an intense focus on applications.[1-3] Surface plasmons are oscillations of the free electron gas at the surface of a metallic structure. They couple efficiently to light and offer the ability to enable confinement and manipulation of light in the nanoscale size regime. Extended structures such as metal films, gratings,[4] nanowires,[5] and channel grooves[6] support propagating plasmons. Many of these structures have great potential for use as plasmonic waveguides that can carry information across computer chips at essentially the speed of light, much faster and with much higher bandwidth than electronic information transfer. Nanostructures, on the other hand, support localized plasmon modes, which have the ability to confine and greatly enhance the electric field of light.[7] These structures also have vast potential for a wide range of applications: enhanced spectroscopies such as surface enhanced Raman spectroscopy (SERS)[8-12] and localized surface plasmon resonance (LSPR) sensing,[13] building blocks for metamaterials,[14-16] and solar energy harvesting and infrared detectors.[17,18] As these applications have become more sophisticated, the required nanostructures have also become increasingly complex. For example, coupled nanostructures of two or more nanoparticles are used extensively in plasmon-enhanced spectroscopy techniques because they often exhibit extremely large optical nearfields.[19-21] These coupled structures have also been shown to support new phenomena such as Fano resonances,[22-24] or resonances with asymmetric lineshapes as a result of coupling between broad and narrow plasmon modes. These structures are extremely good sensors of the local refractive index.[25-28] Asymmetric nanostructures such as split ring resonators[14-16] and nanocups[29-31] have been shown to support magnetic

modes that could be used in metamaterials applications. This class of complex plasmonic nanostructures holds extremely high potential for both applications and new physical phenomena. This thesis will focus on the fabrication and characterization of several examples of these complex nanostructures.

Chapter 2 gives background information concerning several topics discussed throughout the thesis. First, plasmon hybridization theory is explained and then used to explain the optical properties of nanoshells as an example. Next localized surface plasmon resonance (LSPR) sensing is discussed and the figure or merit for LSPR sensors is defined. Then the underlying physics of Fano resonances in plasmonic systems is explained. Lastly, the nanocup geometry is defined and its potential for use in metamaterial applications is discussed.

Chapter 3 provides a detailed look at the experimental technique of darkfield spectroscopy, and how it is used to characterize individual plasmonic nanostructures. Complex nanostructures often cannot be characterized by ensemble methods because their properties are lost among randomly oriented or inhomogenous ensembles, making it imperative that individual nanostructures can be observed and characterized. Darkfield spectroscopy has become the most widely used technique for characterizing single structures, and will be used extensively throughout the remainder of this thesis. Several variations on this technique are discussed in detail in chapter 3.

In chapter 4, the darkfield spectroscopy technique is applied to characterize coupled nanoshell dimer structures. By polarizing the incident light in the darkfield microscope and correlating the spectra of a nanostructure to its precise geometry via

SEM imaging, a deep understanding is obtained of nanoshell dimers in both the cases of touching and nontouching dimers.

Chapter 5 examines planar nanoclusters of 6, 7, and 8 particles. These nanoclusters exhibit Fano resonances that can be precisely controlled by changing the cluster geometry. In particular, the heptamer, or a seven member hexagonally arranged nanocluster exhibits a sharp dip-shaped Fano resonance that is highly influenced by the nanostructure's dielectric environment. It is found that this structure makes an extremely sensitive LSPR sensor with the highest figure or merit recorded for any single structure.

Chapter 6 builds upon chapter 5 with a detailed examination of Fano resonances in coupled planar nanoclusters. It is found that by changing the number of particles in the cluster and the size of the center particle, the Fano resonance can be designed to have a specific width and depth. In larger clusters, the Fano dip achieves true EIT-like transparency over a range of wavelengths. The modes of these structures are examined in greater detail using cathodoluminescence spectroscopy and imaging. Under electron beam excitation, the Fano resonance disappears and is replaced by single modes that differ when the beam excites the structure at different locations. These phenomena are explained using a simple mass and spring oscillator model.

Finally, in chapter 7, the plasmon modes of nanoshell-based, reduced-symmetry structures are examined. Nanoeggs (nanoshells with an asymmetrically thinned shell) and nanocups (semishells) were fabricated by starting with a nanoshell and using an electron beam ablation process to thin and ultimately remove one side of the shell. Darkfield spectra of individual structures are obtained at several intervals during this

ablation process. Simulations are then used to assign the modes of nanocups in both the retarded and quasistatic regimes.

Chapter 2: Background

2.1 Plasmon Hybridization

The field of plasmonics has progressed rapidly with many new structures and devices introduced each year, each with unique properties for specific applications. As the demand for new applications grows and plasmonics is extended into new areas of science and technology, it is necessary to be able to rationally design functional plasmonic structures with specific optical properties. This demand has resulted in a trend of increasing complexity in plasmonic structures, which in turn has resulted in a need for advanced modeling techniques. Several different techniques exist for modeling plasmonic structures and advancements in these techniques have progressed rapidly in recent years.

Mie theory[32] is an example of an early technique for modeling plasmonic structures. First introduced in 1908 by Gustav Mie,[33] Mie theory is an analytical solution of Maxwell's equations which gives the scattering and absorption of spherically symmetric structures. However, spherical symmetry is relatively rare when considering the vast multitude of potential geometries and coupled plasmonic systems, and thus Mie theory is significantly limited in its applicability. Recent advances in numerical simulation methods such as the Finite Element method (FEM)[34] and the Finite Difference Time Domain (FDTD)[35] have allowed for electrodynamic simulations of almost arbitrarily complex geometries. These simulation methods work on the principle of discretizing all objects into very small elements of a geometry for which Maxwell's equations can be easily solved. The full solution to a particular problem can be

constructed from the solutions for each individual element. Thus these techniques are only limited by the amount of computational power and time at one's disposal. These numerical simulation techniques are brute force methods that give very little understanding of the underlying physics. Rational design requires more than simply plugging in a geometry and then getting back the plasmon energies or a spectrum associated with it. Instead, it requires a framework for both quantitative prediction and qualitative intuition of plasmonic properties.

These needs can be met by the plasmon hybridization method.[36-38] Plasmon hybridization is a relatively new way of modeling plasmonic systems that gives a much deeper understanding of the underlying physics. Plasmon hybridization provides an analytical solution of the dynamics of deformations of the electron gas in a metallic structure. In this formalism, metal nanoparticles are treated as an incompressible, irrotational liquid of negative charge (electrons) sitting on a positively charged, fixed background (atomic lattice). The Langrangian for a complex structure, consisting of multiple simpler components can be expressed in terms of the plasmon oscillation amplitudes of the simpler structures with an interaction term that describes the coupling between the components. Thus plasmon hybridization gives a framework for both a qualitative and quantitative understanding of the plasmons in a complex structure as hybridized modes of simpler constituent structures. This formalism is analogous to molecular orbital theory, where the electron orbitals of individual atoms hybridize to form molecular orbitals whenever two or more atoms are bonded together.

2.2 Nanoshells

An illustrative example for plasmon hybridization theory is the metallic nanoshell,[38] which will be used several times throughout this thesis. Nanoshells are spherical nanoparticles consisting of a SiO_2 core coated with a thin gold shell.[39] Typically, the core's size ranges from 50-200 nm and the shell ranges from 10-30 nm. Nanoshells are made by wet chemical fabrication where the SiO_2 core is functionalized with a linker molecule, aminopropyltriethoxysilane (APTES), which bonds to the SiO_2 core via the silane group. Small (1-2 nm) Au nanoparticles are then attached to the other end of this linker molecule via the amine group. These nanoparticles act as seed particles for the growth of additional Au on the surface by reduction from solution in order to create a complete, thin shell.[40]

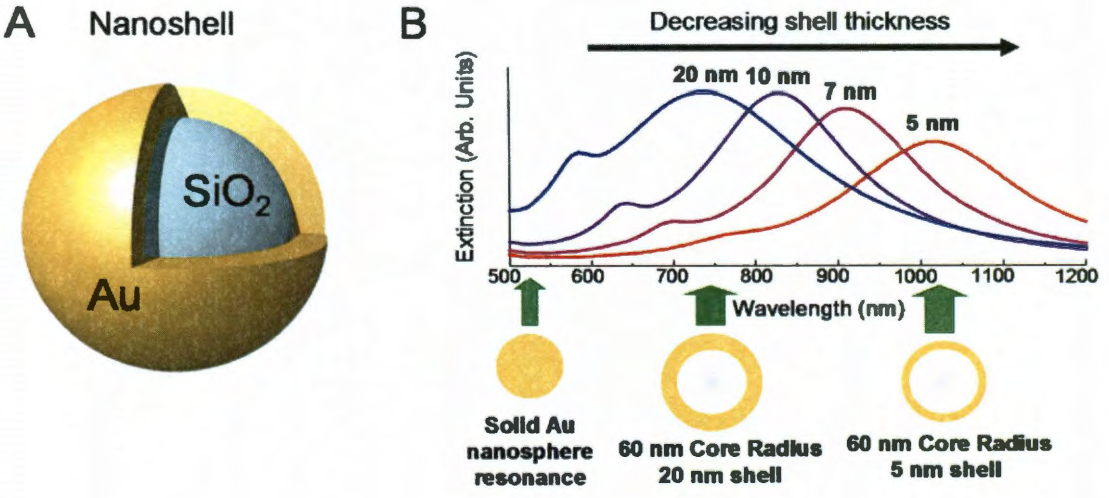

Figure 2.1: (A) Schematic showing the geometry of a nanoshell. (B) Calculated extinction spectra for several nanoshells with a constant core radius of 60 nm and four different shell thicknesses (indicated by the numbers above each curve.

Nanoshells have extremely versatile and highly applicable optical properties. Their plasmon resonances can be strongly tuned from visible to mid-infrared frequencies by precisely controlling the ratio of the size of the core to the thickness of the Au shell (figure 2.1).[39] This tunability can be exploited for a wide range of applications, from surface enhanced Raman scattering[41] to photothermal cancer therapy.[42] The plasmon modes of nanoshells, and their strong tunability, can be understood extremely well using plasmon hybridization theory.

In plasmon hybridization theory, the nanoshell plasmons can be thought of as hybridized modes between the primitive plasmons of a sphere and a cavity. The primitive dipole mode of the sphere and the cavity plasmon hybridize to create two nanoshell modes: an antibonding mode where the dipole moments of the sphere and cavity are anti-aligned and a bonding mode where the dipole moments of the sphere and cavity are aligned. As shown in figure 2.2, the antibonding mode is blueshifted to higher energies while the bonding mode is strongly redshifted to lower energies. The charge configuration of the antibonding mode causes the sphere and cavity dipole moments to oppose each other and subtract, resulting in a small total dipole moment for the nanoshell. This means that the antibonding mode cannot couple efficiently to light, and is sometimes referred to as a "dark" mode. The bonding mode, however, has a very large total dipole moment because the sphere and cavity dipole moments add together. Thus the bonding mode can couple to light very efficiently.

The resonance frequencies of the bonding and antibonding modes are determined by how strongly the primitive sphere and cavity modes interact. Both the geometry and relative spectral positions of the primitive plasmons play a role in the strength of this

interaction. Thus by changing the ratio of the core radius to the shell thickness, the nanoshell bonding resonance can be controllably tuned to any frequency throughout the visible and infraraed. When the shell is made thinner, the inner and outer surface of the nanoshell can interact more strongly, which strongly redshifts the bonding plasmon mode.

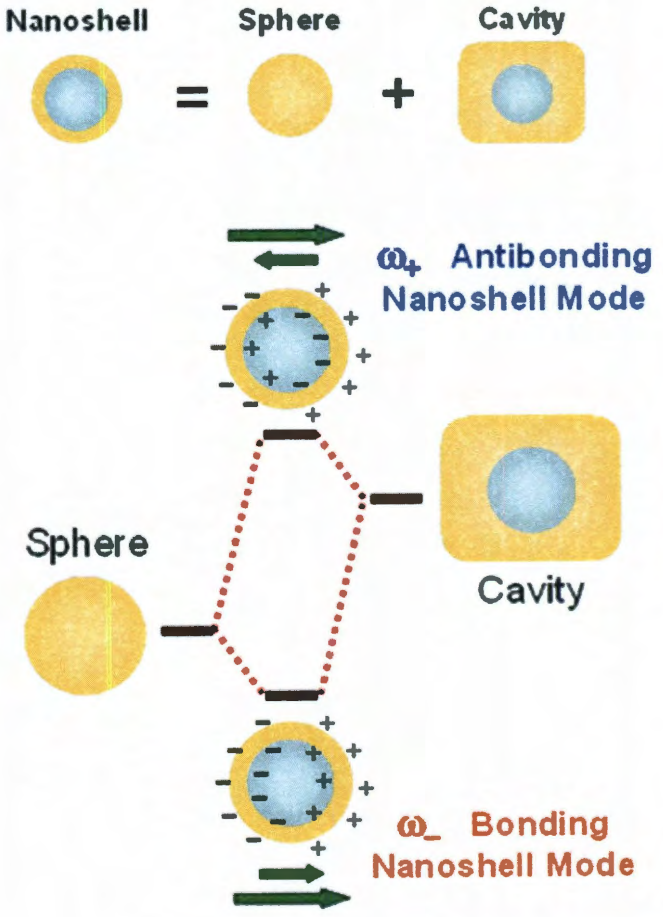

Figure 2.2: Schematic showing plasmon hybridization model applied to nanoshell dipolar plasmons.

Although the above explanation only discusses the dipole modes of the nanoshell, it is important to note that higher order angular momenta modes exist as well, and these modes hybridize in the same way as the dipole modes. Quadrupolar, octopolar, and higher order modes all interact and hybridize. However, different order modes are mutually orthogonal and thus only hybridize with modes of like angular momenta. Quadrupolar and higher order modes do not interact with light for small sizes of nanoshells because they have a near-zero dipole moment. It is important to note that these modes are seen in larger size nanoshells due to retardation effects, which allow higher order modes to become dipole-active.

2.3 Localized Surface Plasmon Resonance Sensing

Although the geometry plays a crucial role in determining the spectral location of the plasmon resonance in a metal nanoparticle, the properties of the materials that make up and surround the nanoparticle can also strongly influence the plasmon resonance.[7] The plasmon resonance results in a sinusoidally varying charge buildup at the surface of the nanoparticle. This surface charge creates a large electric field near the surface of the particle that has been exploited for use in many applications. If the particle is embedded in a dielectric medium, then this electric field can polarize the medium. The polarization of the embedding medium also acts on the nanoparticle surface charge, effectively reducing the restoring force that drives the charge back to equilibrium. This process results in a reduction of the plasmon resonance energy, or a redshift. The degree to which the medium can be polarized, or the polarizability, increases with increasing index

of refraction and thus the degree of redshift of the plasmon resonance depends on the index of refraction of the embedding medium.

This effect can be used as a sensing mechanism for chemical and biological applications, called localized surface plasmon resonance (LSPR) sensing.[13] Using this technique, one can measure the presence of any dielectric substance. In addition, it is possible to detect specific chemicals and biomarkers by functionalizing the surface of the nanoparticle with an appropriate molecular layer that binds both to the metal surface and to another specific analyte.[43] When the analyte binds to the nanoparticle complex, the plasmon resonance will shift in a predictable manner. This technique has been applied to sense biomarkers for the early detection of Alzheimer's disease.[44] It has even been shown that LSPR sensing can be used to measure binding kinetics and to detect extremely low concentrations of an analyte.[45]

For these applications, it is imperative that the plasmon is as sensitive to changes in the local refractive index as possible. A particular plasmon resonance's sensitivity depends both on the degree of resonance shift per unit of refractive index as well as on how easily this shift can be measured. The shift can be more easily measured with a narrow resonance than with a broad resonance. Thus a figure of merit (FOM) has been defined[46] to characterize the sensitivity of plasmonic particles for LSPR sensing:

$$\mathrm{FOM} = \frac{\left(\frac{\Delta E}{\Delta RI}\right)}{\mathrm{fwhm}} \qquad (2.1)$$

where ΔE (units of eV) is the amount by which the plasmon resonance energy has shifted as a result of the dielectric medium, ΔRI (unitless) is the change of refractive index

between two media for which the plasmon resonance energy was measured, and fwhm (units of eV) is the full width, in energy, of the plasmon resonance at half its maximum value. In practice, in order to characterize the FOM, one usually measures the plasmon resonance energy for several different embedding media with a range of refractive indices. In this case, these data points are plotted as the plasmon resonance energy vs. the refractive index, and the numerator in equation 2.1 simply becomes the slope of the linear regression line of these data points. Thus the sensitivity of a particular structure is proportional to the plasmon shift per refractive index unit and inversely proportional to the full width at half maximum of the plasmon resonance.

2.4 Fano Resonances

In 1961, Ugo Fano developed a mathematical framework for describing "shape resonances" in autoionization of He atoms.[47] He sought to explain the asymmetric lineshape in the energy spectrum observed in this system. He explained this phenomenon in terms of the interference between a narrow resonance and a continuum. Although Fano developed this theory in the narrow context of atomic autoionization, the interference between a narrow resonance and a continuum (or a broad resonance) is a general phenomenon that occurs throughout a broad range of physics disciplines. In plasmonics, most plasmon resonances have a Lorentzian profile, typical of general resonant phenomena. Recently, however, Fano resonances have been observed in a variety of plasmonic structures such as ring-disk cavities,[48] concentric spherical particles,[49] and nanoclusters.[22,23,50,51]

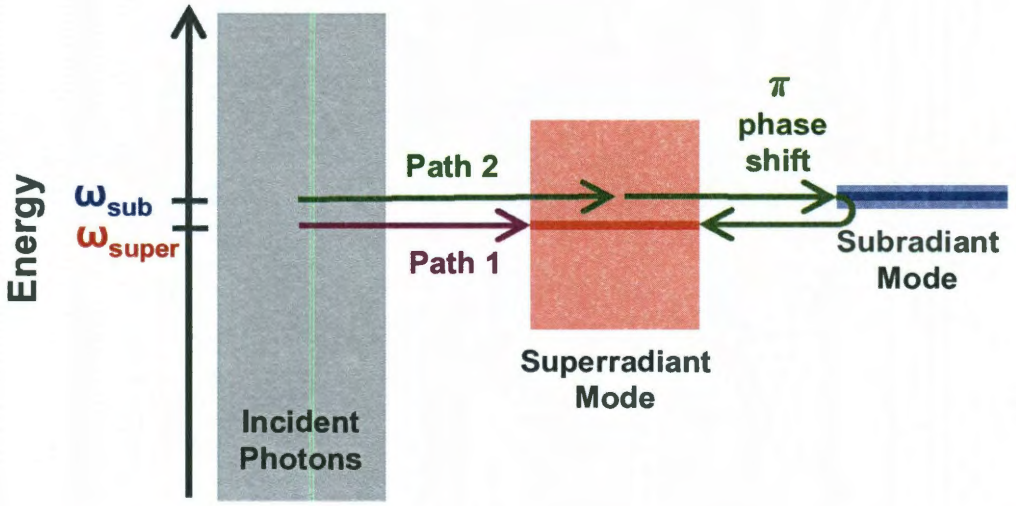

Figure 2.3: Energy diagram for the coupling of subradiant and superradiant modes to make a Fano resonance in a plasmonic system. Paths 1 and 2 represent two different routes for light to couple to the superradiant mode, directly (path 1) or via the subradiant mode (path 2). Note that the vertical width of the three bars represents the linewidth of the modes.

In each of these systems, a plasmon resonance with a narrow spectral linewidth overlaps with a resonance of a broad linewidth.[24] The broad mode interacts strongly with light and is called the superradiant mode, while the narrow mode interacts only weakly with light and is called the subradiant mode. When the subradiant mode overlaps in energy with the superradiant mode, the subradiant mode can "steal" energy from the superradiant mode via nearfield coupling. Note that the subradiant mode cannot be excited directly by light. Therefore the only way that the subradiant mode can be excited is by direct coupling to the superradiant mode. The Fano resonance arises due to interference between two paths by which the superradiant mode can be excited (figure 2.3). In path 1, a photon excites the superradiant mode and then the energy is transferred to the subradiant mode and then back to the superradiant mode, while in path 2, the

superradiant mode is excited directly. During the energy transfer process between the modes in path 1, a π phase shift is acquired, leading to destructive interference.[52] This destructive interference results in a spectral lineshape with a broad resonance (superradiant mode) with a narrow transparency window, or dip, at the frequency of the subradiant mode (see green spectrum in figure 2.4 b). In some cases, this dip feature extends to the baseline, resulting in complete transparency at the subradiant mode frequency, a special case that can be considered to be an analogue to electromagnetically induced transparency.[24]

A useful model for understanding Fano resonances in plasmonic systems is the classical mass and spring model, first suggested by Alzar et al.[53] In this model (figure 2.4), there are two masses, m_1 and m_2, each coupled to a rigid wall by springs with spring constants k_1 and k_2, respectively. The two masses are also coupled to each other via spring constant K. A sinusoidal driving force is applied to m_1 only. In this analogy, m_1 represents the superradiant mode and m_2 represents the subradiant mode. Like the superradiant mode, which is directly driven by light excitation, m_1 is directly driven by the applied force, F. Like the subradiant mode, m_2 can only be driven via coupling to m_1. If one solves the equations of motion for this system, there will be a specific frequency where m_1 moves very little and m_2 oscillates strongly. If the power dissipated by m_1 is plotted (figure 2.4 b, green), a characteristic Fano resonance/EIT lineshape consisting of a narrow transparency window, or dip, in the spectrum at the resonance frequency of m_2 (subradiant mode). The depth of the dip is determined by how strongly m_1 and m_2 couple through the coupling constant, K, and if they do not couple at all, then no Fano resonance is observed (figure 2.4 b, blue). Similarly in a plasmonic system, the coupling between

the subradiant and superradiant modes determines the lineshape of the Fano resonance. By appropriately choosing the values for the masses and spring constants in order to tune the oscillation frequencies and by choosing the appropriate values for damping in the system and the coupling between m_1 and m_2, plasmonic Fano resonances can be precisely fitted with the Alzar model. This model can give valuable insight into plasmonic Fano resonances and will be used later in this thesis.

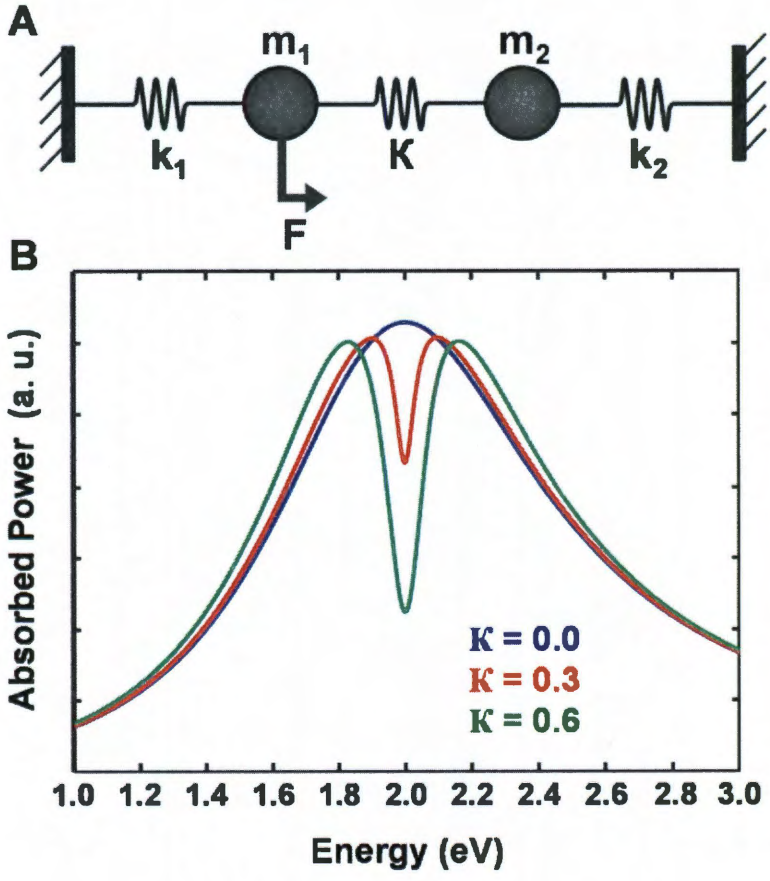

Figure 2.4: (A) Alzar mass and spring model for modeling Fano resonances. (B) Power absorption spectra for the power absorbed by m1 where m1 = m2 and k1 = k2. The resonance frequency for both m1 and m2 is 2.0 eV. Spectra for three different values for the coupling constant, K, are shown.

2.5 Nanocups

Nanocups are reduced-symmetry nanostructures consisting of a cup shaped semishell of Au, typically on a spherical SiO_2 or polystyrene core.[29-31,54,55] These particles have two fundamental dipolar modes: an axial (electric) plasmon mode that is excited by light polarized parallel to the cup's axis of symmetry and a transverse (magnetic) mode that is excited by light polarized perpendicular to the symmetry axis of the cup (figure 2.5). The transverse mode is a magnetic mode because a dipole moment is induced across the rim of the cup setting up a current flow around the outside of the metal semishell. This current induces a magnetic field in the interior of the nanocup that oscillates at the resonance frequency.

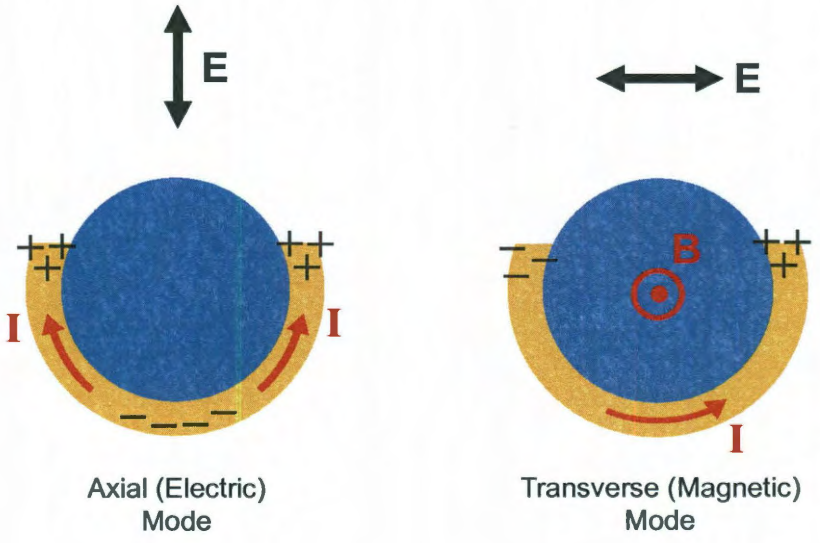

Figure 2.5: Schematic of the axial and transverse modes of nanocups.

These cups are similar to the split ring resonators used for metamaterials applications in the infrared and microwave frequency ranges.[14] The magnetic modes of split ring resonators are exploited to create media with a negative permeability at high frequencies in order to achieve negative refraction and cloaking properties. Similarly nanocups have attracted interest as a potential building block for metamaterials in the visible frequency range via their strong magnetic resonance. It has also been shown that this magnetic mode has the unique property of being able to "bend" light.[30] Light that is scattered by the magnetic mode tends to be reradiated according to the direction of the magnetic mode dipole moment, regardless of the incident direction. This property could hold promise for coupling light into waveguides and solar cells.

Chapter 3: Darkfield Spectroscopy of Plasmonic Nanostructures

3.1 Spectroscopy of Individual Nanostructures

When light impinges on a plasmonic nanostructure, it will either be elastically scattered or absorbed in proportion to the amplitude of the plasmon oscillation. Thus light is strongly scattered at the plasmon resonance frequencies, but the particle will not interact with light (transparent) at frequencies away from the resonances. As a result, one can discern the plasmon resonances of structures using optical spectroscopy.[56] The field of nanotechnology originally inherited spectroscopic techniques from the fields of chemistry and physics. However, these techniques typically involved measuring the optical spectra of a large ensemble of molecules or atoms simply because it was not possible to measure one atom or molecule, nor was it necessary. Similarly, most early experiments in plasmonics were also confined to the measurement of large ensembles of particles.

However, it soon became obvious that, in many cases, the plasmonic properties of a nanostructure were not necessarily always captured accurately by ensemble measurements. Chemical fabrication techniques essentially never produce a completely monodisperse ensemble of particles. From particle to particle, variations in the size and shape are virtually always present. This leads to a problem in that each particle in an ensemble has a slightly different spectrum, and thus the ensemble spectrum has broadened peaks such that some features cannot be observed. This problem has been

observed even for the simplest plasmonic structures such as spheres[57] and nanoshells.[58] Furthermore, even more problems with ensemble measurements arise for complex and asymmetric structures such as dimers, nanocups, or lithographically fabricated structures. Here the fabrication techniques are much more complicated leading to the twofold problem that the ensemble has an even more exaggerated inhomogeneity, plus the yield of final structures is often so small that conventional ensemble techniques cannot even register spectra for such low concentrations. Furthermore, debates existed in the plasmonics community over the origins of spectral broadening in many plasmonic structures.[56,58,59] Specifically, it was debated whether the broadened lineshape of small plasmonic particles was an intrinsic broadening caused by scattering of the electrons off the surface of the particle, or was this broadened lineshape due only to inhomogeneous broadening in an ensemble of particles. These debates could not be resolved by ensemble experiments.

These complications in measurement of plasmonic nanostructures led to the need for new characterization techniques. In particular, it was desirable to be able to measure the optical properties of one, individual nanostructure.[60] Several techniques have emerged for this purpose ranging from near-field scanning optical microscopy,[60] total internal reflection spectroscopy,[61] cathodoluminescence,[62,63] electron energy loss spectroscopy,[63] and dark-field spectroscopy.[57,58,64,65] However while each of these techniques gives extremely useful information at the single particle level, dark-field spectroscopy (DFS) is much cheaper and less complex to implement. As a result, several research groups began to use this technique extensively for characterizing single

nanostructures and for realizing new applications,[45,66-71] and currently DFS is a widely used technique in plasmonics.

3.2 Darkfield Microscopy

Dark-field spectroscopy is based on performing imaging and spectroscopy with only the light that is scattered by a nanostructure. In this technique, a darkfield microscope is used to image, and collect light from a nanostructure. This collected light is then routed to a spectrometer for analysis. Both the darkfield microscope and the spectrometer are critical pieces that will be discussed in detail below.

Dark-field microscopes of various forms have been used for over a century to improve contrast and to detect structures smaller than the wavelength of light. The first example of a dark-field microscopy technique was the ultramicroscope, originally developed by Zsigmondy for studying colloidal particles smaller than the wavelength of light.[72] In the ultramicroscope, light is introduced at a right angle of incidence with respect to the optical path of the imaging optics of the microscope. As a result, only the light scattered by a suspension of colloids is imaged, which allowed Zsigmondy to identify and study the individual colloids in a suspension, work that earned him the 1925 Nobel Prize in Chemistry. More modern variations on dark-field microscopy are now in widespread use across a broad range of disciplines from biology to materials science, and also nanotechnology.[73]

In darkfield microscopy, the illumination is incident at a large angle with respect to the sample substrate normal. This incidence angle is large enough that it is outside of the solid angle where the objective lens can collect the reflected or transmitted direct illumination. As a result, only the light scattered by the sample is collected. Because the direct illumination is not collected, the background appears dark, and the observer sees bright features that scatter the light into the solid angle that can be collected by the objective lens. This differs from brightfield microscopy where the illumination is incident on the sample at normal incidence and is either transmitted through a transparent sample or is reflected by a reflective sample (figure 3.1). The microscope objective then collects and images the transmitted or reflected light, and the observer sees an image of the light that has been removed from the field of view by scattering or absorption processes in features on the sample. In other words, the observer sees an extinction image, producing dark features on a bright background. The darkfield technique therefore offers significant advantages over brightfield microscopy for spectroscopy of nanostructures. It is possible to detect extremely small particles, using a darkfield microscope, that only interact weakly with light. Furthermore an extinction measurement, as in the case of brightfield microscopy, is extremely limited by shot noise since the amount of light removed from the image by a nanoparticle is very small with respect to the bright background. Darkfield measurements do not suffer from this problem, however, since there is a very low background signal level in the dark image backround, and can therefore typically achieve very good signal-to-noise ratios without much difficulty.

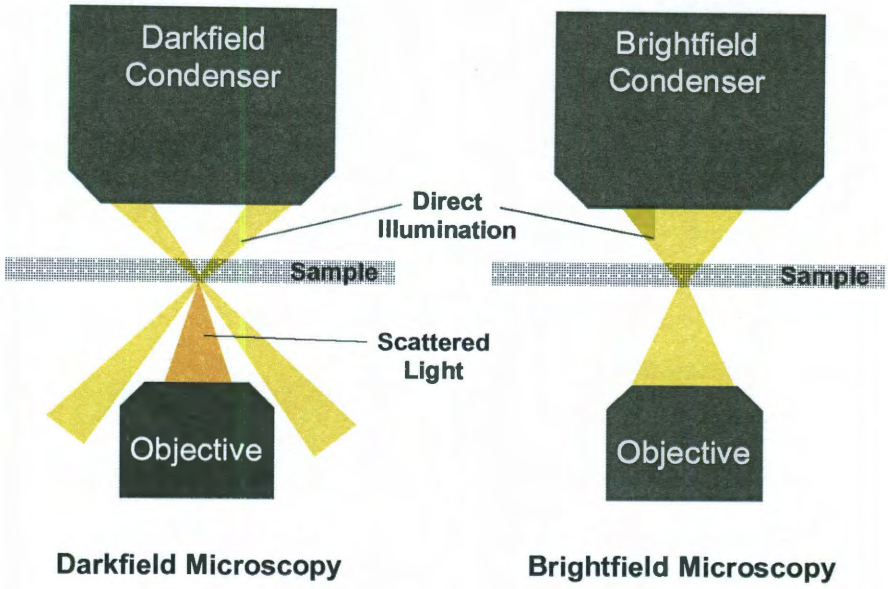

Figure 3.1: Schematics showing the differences in the light path between darkfield and brightfield microscopy

Dark field microscopes can be setup in either a reflection or transmission geometry (figure 3.2). In transmission darkfield, a darkfield condenser focuses light through the backside of a transparent sample at a large angle with respect to the substrate normal. The light is incident on the sample in a hollow cone. The direct light continues into free space while the light scattered by the sample is collected by the objective lens, which is on the opposite side of the sample from the condenser. Here it is important that the darkfield condenser has a larger numerical aperture (NA) than the objective lens. The numerical aperture of a lens is defined by NA = $n \sin(\theta)$ where n is the refractive index of the medium between the sample and the lens and θ is the largest angle of light that can be collected by the objective, measured from the substrate normal. By contrast, reflective darkfield configurations have the illumination source on the same side of the setup as the objective lens. Again, the illumination must have a larger NA than the collection optics.

In most commercial darkfield systems, the condenser is built into the objective itself such that illumination is routed through optics in the outside portion of the objective housing, and the collection optics are in the interior of the objective housing. In both cases, the direct illumination is either transmitted through the sample or specularly reflected by the sample.

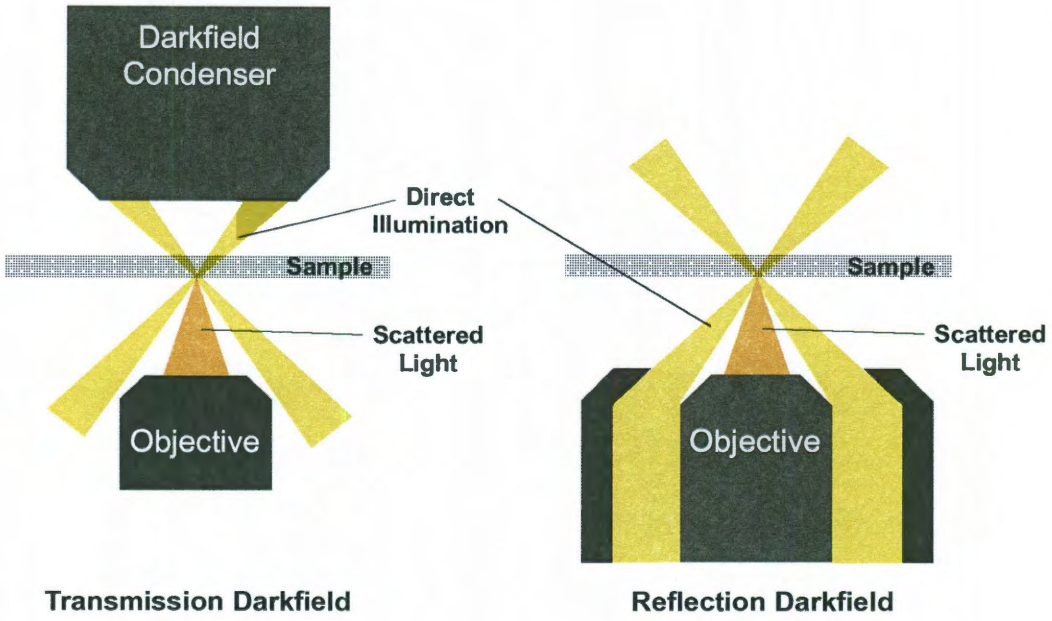

Figure 3.2: Schematic showing configurations for transmission and reflection darkfield

It is important to note, however, that darkfield conditions can be easily achieved using simple, homebuilt microscopes as well. An independent illumination source can provide light incident at an angle larger than the objective lens NA. In these systems, simple optics can be used to direct an illumination beam onto the sample from one direction only. Depending upon the location of this illumination source, these systems

can also be configured into a transmission or reflection geometry (figure 3.3). While this directional illumination causes somewhat degraded imaging due to the lack of even illumination, these configurations can provide some advantages for spectroscopy such as angular control of the illumination incidence direction and easy implementation of polarization-dependent measurements.

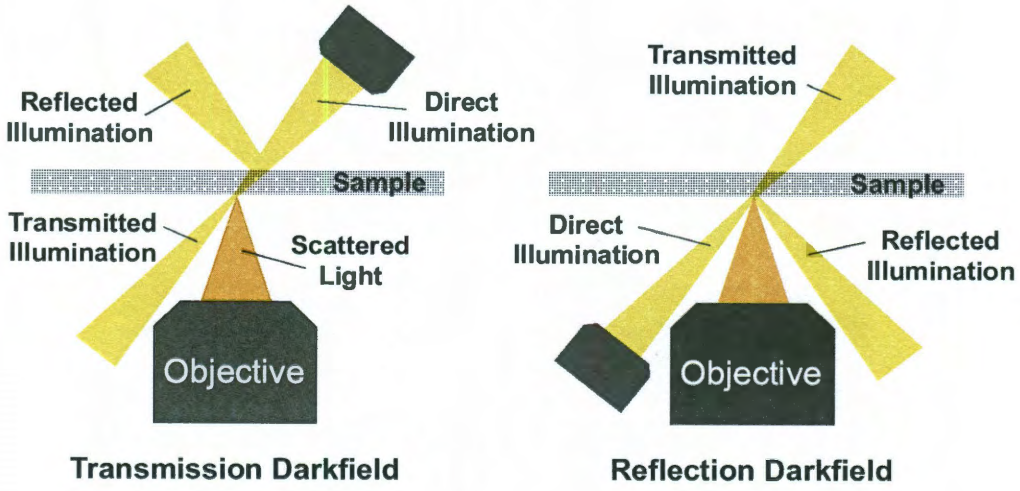

Figure 3.3: Schematic showing transmission and reflection configurations for homebuilt darkfield microscopy systems

3.3 Collection and Analysis of a Spectrum

Once the scattered light has been collected, the microscope optics route it toward a spectrometer for analysis. Specifically, the tube lens of the microscope focuses an image of the nanoparticle onto the entrance slit of a spectrograph coupled to a scientific CCD camera. The light is dispersed into a spectrum by a reflective grating, and the final spectrum is focused onto the CCD. The final spectrum appears as a streak on the CCD,

where the streak is a focused image of the dispersed light from (figure 3.4C). Each point along the spectrum peak is simply an image of the particle at a particular wavelength. Note that the spectrometer slit plays an unconventional role in this spectroscopy technique. Typically the slit serves to control the spectral resolution of features in a spectrum. However, here the image of the nanoparticle is a diffraction limited spot, and the size of the Airy disk of the nanoparticle image determines the spectral resolution. The slit simply serves to remove the images of nearby particles on the sample that could provide spurious spectral features. Figure 3.4A shows an image of a large sample of 100 nm Au colloid particles, while figure 3.4B shows how the slit is used to select a particular particle from the field. (Actually any line of particles parallel to the slit can be selected and analyzed simultaneously.) The size of the slit opening controls the amount of background signal that enters the spectrograph, and thus influences the signal-to-noise ratio of the final spectrum, but the background signal is typically low enough that this effect is minor.

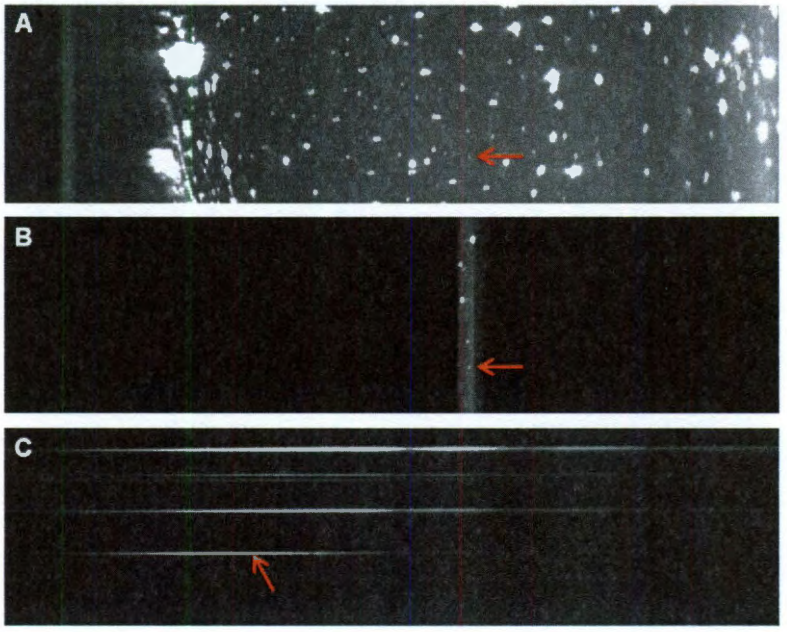

Figure 3.4: (A) Darkfield image of a field of particles on a glass substrate. (B) The same field of particles, except that the spectrograph slit has been moved into place to select a particular particle. (C) The grating in the spectrograph has been positioned to disperse the light into a spectrum. In all panels, the red arrow indicates the particular particle to be analyzed.

Once the spectrum has been acquired, it must be analyzed in order to get a final spectrum, typically done using custom analysis code. The spectrum streak must be selected out of the larger spectrum image (figure 3.4C), by choosing a small range of horizontal pixel rows over which the streak extends. Each vertical line of these rows is summed in order to get a raw spectrum R. Next the background must be subtracted out of the spectrum in order remove any signal that originates from the sample substrate but not from the specific nanoparticle being measured. This is done by either taking a separate image over a background area of the sample, or a background region from the original spectrum image (figure 3.4C) can also be used, given a sufficiently high quality CCD with minimal variations in sensitivity across the sensor array. In the latter case, two

ranges of rows from the image are selected that are directly above and below the spectrum rows and also identical in size to the spectrum rows. These background rows are summed across each vertical line of pixels to get two total background spectra from either side of the spectrum and are then averaged to give a final background spectrum B.

The background spectrum will be used to remove unwanted signal from the raw spectrum, but it cannot account for wavelength-dependent variations in the efficiency with which the spectrum was acquired. These variations are caused by the spectral variations in the output of the illumination lamp, the quantum efficiency of the CCD camera, and the spectral efficiencies of all of the optical components in the entire light path of the instrument. The raw spectrum is a convolution of each of these spectral efficiencies with the spectrum of the actual particle. These contributions must be deconvolved by dividing out the instrument's response to a spectrally flat signal. For this purpose, a white calibration spectrum, W, must be acquired by focusing the microscope onto a white (spectrally flat), diffuse reflection standard (Labsphere). A dark calibration spectrum, D, or a spectrum taken with no illumination in the optical path of the instrument, must also be acquired and subtracted from the white spectrum in order to remove any detector dark current contributions from the white calibration spectrum.

This data analysis can thus be expressed as the following equation for the final spectrum, S:

$$S = \frac{R-B}{W-D} \tag{3.1}$$

In figure 3.5, the components for each of these terms are shown for a test case colloidal gold particle along with the final spectrum after the above equation was applied. Here, it is evident if one subtracts R (red) – B (green), then the majority of remaining signal will be in the 500 – 700 nm range, since there is almost no different between the two in the near IR wavelengths. The yellow curve represents the white calibration spectrum with the dark signal already substracted out, or the denominator in equation 3.1. By inspecting this curve it is obvious that there is quite a lot of variation in this instruments spectral efficiency, with several maxima and minima appearing throughout. Most of this variation originates from the light source, in this case. However, when these components are processed via equation 3.1, it is obvious that a smooth and accurate final spectrum can be obtained (blue curve). This spectrum, with the peak position at 600 nm, is characteristic of large colloidal Au particles, and shows that the data analysis was performed properly.

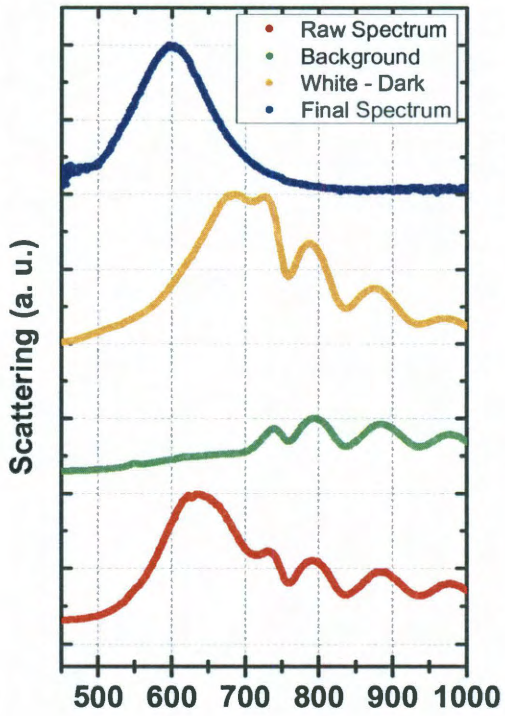

Figure 3.5: Construction of the darkfield spectrum for the 100 nm spherical Au nanoparticle selected in figure 3.4. Red curve is the raw spectrum, green curve is the background spectrum, yellow curve is the white calibration with the dark signal already subtracted. The blue curve is the real spectrum of the nanoparticle constructed from the red, green, and yellow curves according to equation 3.1.

3.5 Polarization-Dependent Darkfield Spectroscopy

For spherically symmetric plasmonic nanoparticles, the plasmon resonances that oscillate along any axis of the particle are all degenerate. However, this degeneracy is relaxed for particles with reduced symmetry, where modes of different energies can oscillate along each direction of the nanoparticle's geometry. As a result, reduced symmetry nanoparticles have polarization-dependent scattering spectra. For example, nanorods are elongated nanoparticles that support two resonances: one near 550 nm when excited by light polarized along the short axis of the nanorod and another redshifted

resonance that occurs from ~650 nm to ~900 nm (depending on the aspect ratio of the nanorod) when light is polarized along the long axis of the nanorod.[74] Other examples of polarization-dependent structures include nanoantennas, nanoparticle dimers,[69] and split-ring resonators.[16] This class of asymmetric nanostructures has become increasingly prevalent as their potential for applications has been realized. Complete characterization of individual asymmetric nanostructures requires polarization-dependent darkfield spectroscopy.

One form of polarization-dependent darkfield measurements requires simply placing an analyzer into the collection optics light path. For unpolarized illumination, all modes of the structure will be excited, and then the analyzer polarizes the scattered light that is collected by the objective lens. One can rotate the analyzer to align with particular axes of the nanostructure and obtain spectra corresponding to each polarization direction. This method works well for two dimensional structures where the only important modes are those that oscillate in the plane parallel to the substrate. In many cases, however, it is necessary to polarize the incident light. For example, one may need to isolate and measure plasmon modes that oscillate out of plane, such as measurements of three dimensional structures or structures that interact significantly with the supporting substrate.[75] In this case, one must be able to illuminate the nanostructure with S and P polarized light (with respect to the sample substrate).

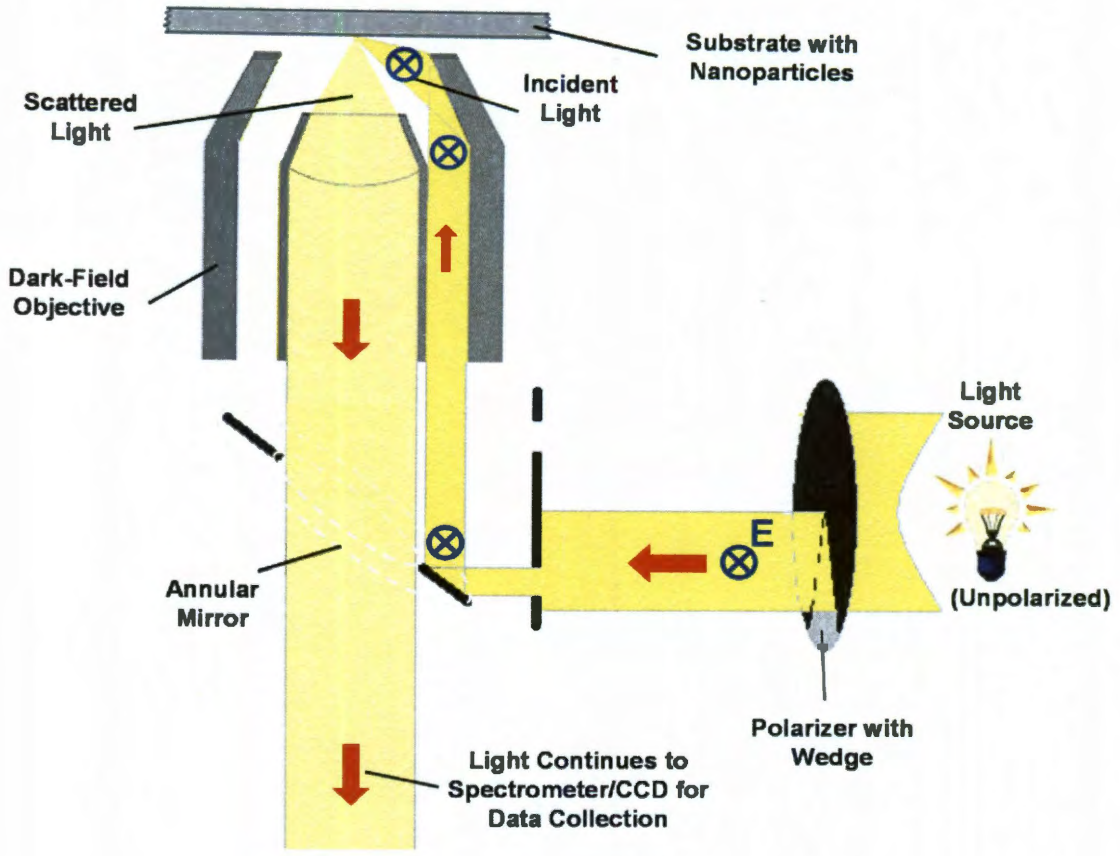

Figure 3.6: Polarization-dependent darkfield illumination in a commercial microscope, using a polarizer and wedge cutout (shown as S polarization at the sample plane)

In the case of homebuilt systems like those shown in figure 3.3, polarizing the incident light is simple by placing a polarizer in the illumination path. However, this is more complicated in commercial darkfield systems where the condenser is built into the objective housing. In this case, it is not enough to simply put a polarizer the optical path because there are multiple reflective surfaces in both the microscope and the objective housing that must be taken into account. In this case, the three dimensional geometry of the illumination path will result in mixed polarization at the sample plane. Light incident from different directions will be either S or P polarized, resulting in mixed and S and P

polarization at the sample. This problem can be solved by placing a wedge-shaped beam block in the optical path (figure 3.6). This allows some of the light to pass through the wedge-shaped cutout while the rest of the light is blocked, thereby selecting a single incidence direction and therefore a single polarization. When the polarization angle is parallel to the wedge cutout, the illumination will be P polarized with respect to the substrate, and when the polarization angle is perpendicular to the cutout, the illumination will be S polarized.

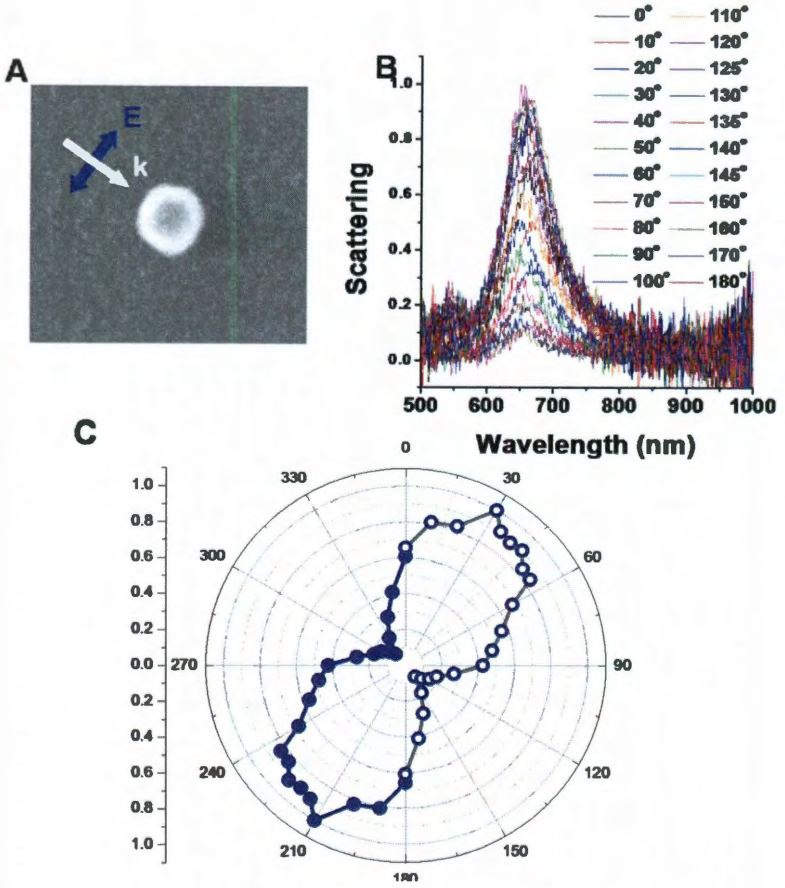

Figure 3.7: Determination of incidence angle for polarized illumination. (A) SEM image of a spherical nanoshell used to determine incidence and polarization direction. (B) Series of spectra for the nanoshell in A at analyzer angles from 0 to 180 degrees. (C) polar plot of the spectra amplitudes at 650 nm. The dipole pattern indicates that the polarization direction is 30 degrees.

If it is necessary to precisely control the exact angle of direction of the incident light, then an additional measurement is necessary to ascertain and calibrate this angle. This is accomplished by setting up the condition for S-polarization, as discussed above, and then measuring a spherically symmetric particle with a rotating analyzer. In this case, we will use a nanoshell with a dipole resonance at ~660 nm under all polarization angles (figure 3.7A). By keeping the illumination intensity, direction, and polarization constant as well as keeping the detector integration time constant and only varying the analyzer angle, one obtains a series of spectra that each have a peak at ~660 nm, but with different amplitudes. The spectrum with the highest amplitude peak should have occurred when the analyzer angle was aligned with the polarization of the incident light, and the lowest amplitude peak should occur when the two are perpendicular to each other. By plotting the maximum values of the plasmon peak on a polar plot vs analyzer angle, a dipole pattern emerges. The maximum of this dipole pattern determines the polarization angle. In this case the polarization angle is 30^{o} and the incidence angle of the light must then be -60^{o}.

Chapter 4: Plasmonic Coupling Between Two Nanoshells

4.1 Introduction

It is now well known that metallic nanostructures can support resonant oscillations of their conduction band electrons, termed localized surface plasmon resonances (LSPR), when illuminated with light of certain frequencies.[7] Plasmons give rise to large enhancements of the local electromagnetic field at the nanostructure surface, an essential aspect of surface-enhanced spectroscopies.[8-12,19,76,77] The plasmonic properties of a nanostructure depend dramatically on its size and shape, as has been demonstrated in studies of nanorods,[74,78] nanocubes,[46,79] nanostars,[71] nanoshells,[39] and numerous other structures. An understanding of how the plasmonic properties depend on geometry enables the rational design of nanostructures tailored for specific applications such as surface-enhanced spectroscopies,[21,41,80] where one seeks to maximize the electromagnetic field enhancement over specific frequency ranges, or LSPR sensing, where narrow spectral linewidths and a high sensitivity to the dielectric environment are desirable.[46]

Directly adjacent nanoparticle pairs, also known as "dimers", give rise to very large field enhancements in their junctions, which make them highly attractive as SERS substrates, with enhancements approaching single molecule sensitivities.[9-12,19] Coupling multiple nanoparticles together in chain-like structures has also been suggested as an approach to nanoscale optical waveguiding and focusing.[81-83] Advances in our understanding of plasmonic nanoparticle interactions will greatly facilitate our abilities to design, develop and optimize such coupled-nanoparticle systems.

Plasmonic dimers of various nanoparticles have been studied experimentally and theoretically,[21,68-70,84-90] with the general observation that for incident light polarized along the dimer axis, a redshift of the longitudinal plasmon resonance occurs with decreasing nanoparticle separation. Plasmon hybridization theory applied to nanoparticle dimers has led to the understanding of dimer plasmon modes as the bonding and antibonding hybridized modes of the characteristic plasmons of the constituent nanoparticles, which remain charge neutral.[36,37,91] Recent attention has begun to focus on the transition that occurs in a dimer as the interparticle separation is reduced to the onset of conductive overlap and beyond.[86,92,93] When a conduction channel is present between two nanoparticles, new longitudinal plasmon modes involving charge oscillations between the two nanoparticles become possible. In this situation, the total charge on each nanoparticle will oscillate in time. As the particles are merged further, these plasmon modes blueshift to values determined by the aspect ratio of the composite particle.

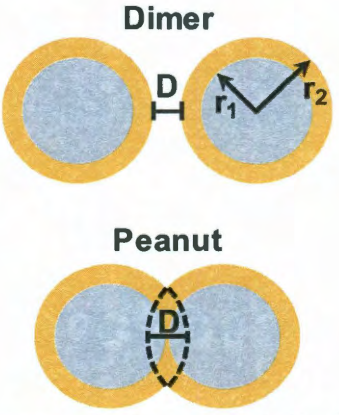

Figure 4.1. Schematic diagram of the nanoshell dimer and peanut geometries. Individual nanoshells are defined by the core radius r_1 and the overall radius r_2. The distance D is defined as the distance between the outer surfaces of the constituent nanoshells of a peanut or dimer. Thus for dimers, D takes on a positive value and represents the degree of separation, but for peanuts, D takes on a negative value and represents the degree of overlap.

Here, we examine the plasmon interactions of individual pairs of nanoshells in the adjacent and touching regimes (Fig. 4.1). The characteristic plasmon resonances of a nanoshell, already significantly more sensitive to changes in their dielectric environment relative to solid metallic nanoparticles,[94] interact strongly with the plasmon modes of the adjacent nanoshell. Using polarization dependent dark-field microspectroscopy, we examine the plasmon interaction for weakly and strongly interacting individual proximal nanoshell pairs and for individual touching nanoshell pairs, or "nanopeanuts". Strong polarization dependence for all modes of interaction is observed. With excitation polarization along the dimer axis, for strongly interacting nontouching nanoshell pairs we observe extremely large LSPR shifts and the excitation of hybridized higher order multipolar plasmon modes. In the touching regime, the plasmon spectrum provides a highly polarization and geometry-dependent signature of a plasmon mode involving electrons flowing back and forth between the two particles. High resolution SEM images reveal important structural details of each dimer and nanopeanut, permitting close comparison of theoretical simulations with experimentally observed plasmonic behavior in all cases.

4.2 Experimental Methods

Nanoshell dimers were fabricated by employing a multistep process similar to other recently developed dimer fabrication procedures.[95,96] Initially, nanoshells were fabricated as previously reported,[39] then deposited onto a glass coverslip functionalized with 1 wt. % poly(vinyl pyridine) (PVP) in ethanol.[97] Next, the nanoshell-coated

coverslips were immersed in a 1 mM ethanolic solution of 1-dodecanethiol for 12-24 hours, allowing self-assembled monolayers (SAMs) to form onto and passivate the nanoshell surfaces except for the small region of the nanoshell surface that touches the glass slide. The substrate was then removed from solution, rinsed, and sonicated for approximately 4 minutes in the presence of a 0.1 mM ethanolic solution of 1,9-nonanedithiol. This step removes the nanoshells from the glass surface, exposing the unpassivated surface area of the nanoparticles so that the nonanedithiol molecules can adsorb, linking the nanoshells together to form dimers. Because the majority of the nanoshell surface was passivated before exposure to the linker molecule, the number of nanoshells that can attach to each other is limited, resulting in the preferential formation of dimers rather than extended aggregate structures. The nanostructures were then deposited onto a glass substrate for microspectoscopy measurements. This fabrication procedure results in a mixed dilute ensemble of nanoshell monomers, dimers, some larger n-mers, and fused nanoshell dimers, or nanopeanuts. The nanopeanuts are most likely formed during the initial nanoshell fabrication procedure when two nanoshell precursor nanoparticles adhere to each other before or during the formation of the gold shell. The resulting nanoparticle distribution allows us to directly compare spectra of individual structures on the same substrate and therefore under virtually identical experimental conditions.

In order to directly compare a specific nanostructure's geometry to its associated spectra, individual structures were first located using environmental scanning electron microscopy (ESEM, FEI Quanta 400) on the glass substrate with respect to a gold finder grid evaporated onto the surface.[58] ESEM allows scanning electron microscopy to be

done in a low pressure (here ~2 Torr) water vapor environment so that excess charge can dissipate from the nonconductive substrate. Glass was chosen because it provides an unambiguous substrate for spectroscopy of plasmonic nanostructures that does not strongly modify the plasmon lineshape. The orientation angles of both nanoshell dimers and nanopeanuts were measured with respect to the finder grid, such that polarization orientations could be determined during subsequent optical measurements. Our optical setup for unpolarized and polarized dark-field microspectroscopy has been presented in previous works,[58,98] and was outlined in chapter 3.

For each structure studied experimentally, exact electrodynamical calculations of the optical response based on the boundary element method (BEM) were performed to examine agreement with experimental results.[99] First, the dimensions of each particle along the directions of the measured polarizations were recorded using ESEM. These dimensions served as an initial guide for fitting the experimental data. For dimers, a best fit was obtained by varying the core sizes and the interparticle distance slightly, and for peanuts, the size and separation distance of the cores were varied. The nanoshells were modeled with a core dielectric function for SiO_2[100] and with a shell dielectric function for Au[101].

A single nanoshell "monomer" was examined as a test case to ensure that the BEM simulations could match our experimental spectra well for a simple case and to verify that the expected plasmon spectrum was preserved for polarization-dependent illumination (Fig. 4.2). A monomer should theoretically have no polarization dependence due to its spherical symmetry. In our measurements we did observe a slight shift of the resonance under two different orthogonal polarizations (red and blue). However,

dimensional measurement of this nanoshell along the two polarization directions revealed a slight asymmetry of the nanoshell. By incorporating this asymmetry into our BEM simulations, a small polarization dependence was observed, yielding excellent agreement between simulations and experiment.

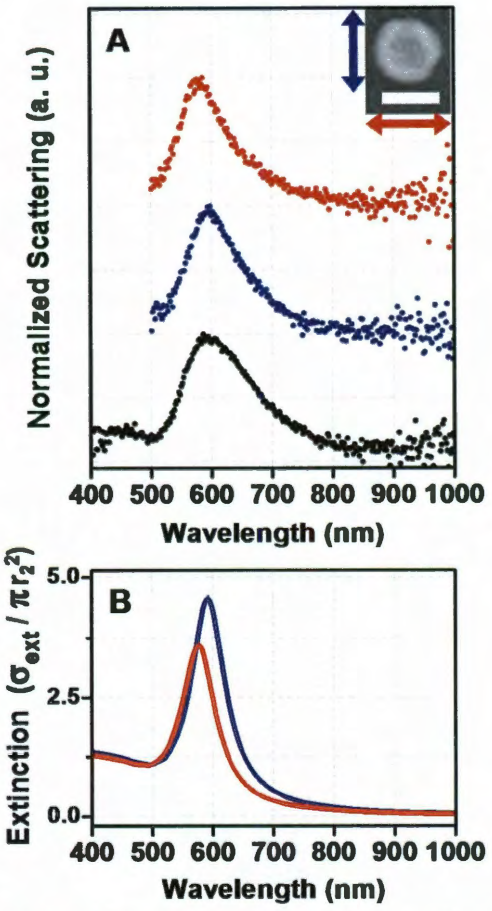

Figure 4.2. Normalized scattering spectroscopy of a single nanoshell . Black spectra correspond to unpolarized illumination; blue and red spectra correspond to polarization arrows of the same colors in insets. The inset ESEM image shows the specific nanoshell monomer for the presented data (scalebar = 100 nm). (A) Experimental data for a single nanoshell. (B) BEM simulations fitting data in A. This nanoshell was fit as having a core radius of 40 nm and a slightly elliptical shell where the short semi-axis measured 52 nm and the long semi-axis measured 57 nm. Simulations are normalized to the physical cross section of a nanoshell.

4.3 Nanoshell Dimers

Nanoshell dimers show dramatic and easily measurable interparticle plasmon coupling in their polarization-dependent spectra. In Figure 4.3A, the spectra and corresponding ESEM image of a nanoshell dimer with a relatively large interparticle separation distance on the order of the shell thickness is shown. Here and in the subsequent figures, the black spectrum represents illumination with unpolarized light while the blue (red) spectrum represents illumination that is polarized transverse (longitudinal) with respect to the dimer axis. The longitudinal polarization exhibits only a small redshift of the dipole plasmon (peak 1), characteristic of a weakly interacting dimer. The simulations reproduce the experimentally obtained spectra quite well (Fig. 4.3B). The small redshift of the longitudinal dipole plasmon observed experimentally is reproduced qualitatively in the simulations by modeling a dimer with a 20 nm separation distance, a relatively large distance consistent with the ESEM image in Figure 4.3A. In the weak coupling regime the shift of the dimer plasmon is small and insensitive to interparticle distance.

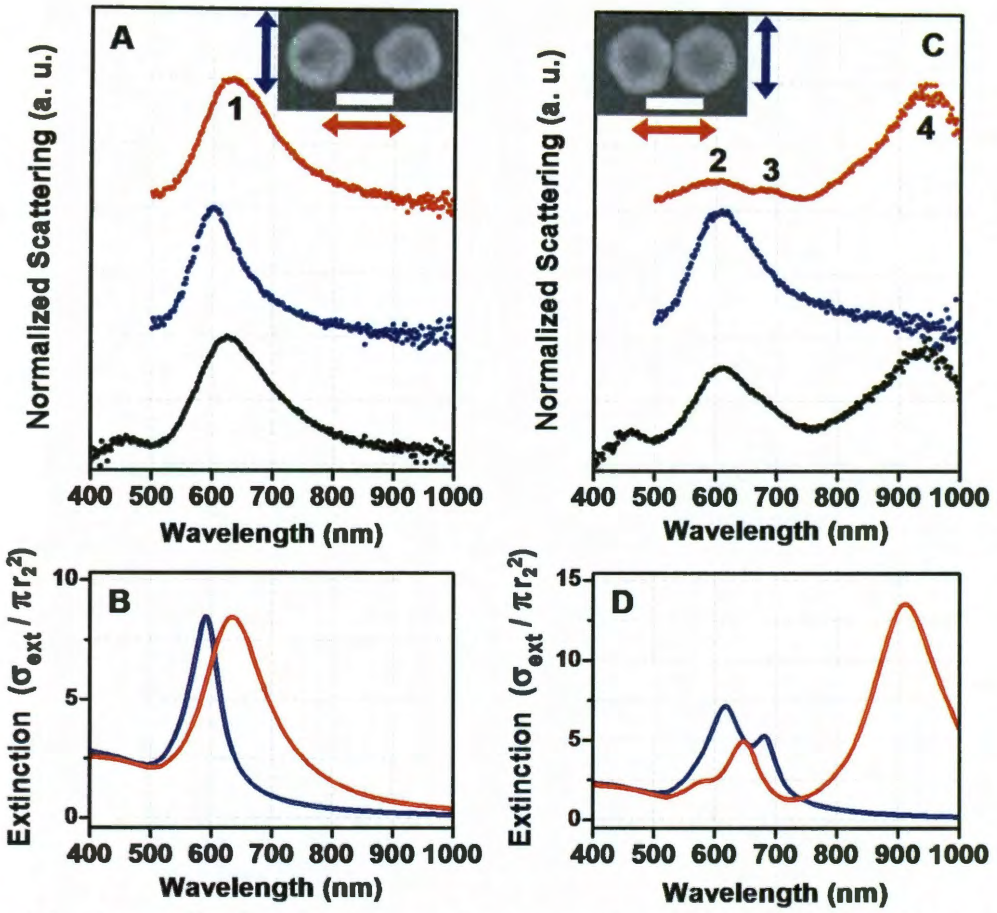

Figure 4.3. Normalized scattering spectroscopy of nanoshell dimers. Black spectra correspond to unpolarized illumination; blue and red spectra correspond to polarization arrows of the same color in the insets. The inset ESEM images show the specific dimers for the presented data (scalebar = 100 nm). Peak numbers correspond to numbered energy levels in Figure 4.4. (A) Experimental data for a weakly interacting dimer. (B) BEM simulations fitting data in A. Both shells were fit as $(r_1, r_2) = (42, 59)$ nm with D = 20 nm. (C) Experimental data for a strongly interacting dimer. (D) BEM simulations fitting data in C. Both shells were fit to be slightly elliptical, elongated in the transverse direction: The leftmost shell has a core with semi-axes 45 and 47 nm and an outer shell with semi-axes 58 and 60 nm while the rightmost shell has a core with semi-axes 42 and 48 nm and an outer shell with semi-axes 55 and 61 nm with D = 1 nm. Simulations are normalized to the physical cross section of a nanoshell.

For a nanoshell dimer with a much smaller separation distance the interaction is significantly stronger, exhibiting a much larger redshift (Fig. 4.3C). Here the ESEM image shows a nanoshell dimer with an interparticle spacing D~ 1-1.5 nm consistent with

the nanoshells being chemically linked by the nonanedithiol tether molecules.[102] For this dimer, the longitudinal dipolar plasmon mode has redshifted quite dramatically, to 930 nm. The drastic increase in the degree of redshifting in this case has two origins. One contribution results from the fact that the interaction is mediated by the electromagnetic near field, which increases rapidly towards the shell surface.[103] The second effect contributing to the magnitude of the plasmon shift is the presence of the linker molecules between the nanoshells of the dimer structure. In our simulations, to achieve quantitative agreement with the experiment required the introduction of a 1 nm thick dielectric layer with a refractive index of 1.42 (corresponding to the SAM) surrounding both shells and the interparticle junction. This effect, which has important implications for nanoparticle-based sensing, will be discussed further below.

Two higher energy modes are also clearly observable in the longitudinally polarized spectrum of the strongly interacting dimer, denoted peaks 2 and 3 (Fig. 4.3C). These features cannot be resolved in the unpolarized spectrum since the longitudinal quadrupolar and octupolar dimer plasmons overlap the transverse dipolar dimer plasmon. The calculated longitudinal polarization spectrum contains three peaks, in good agreement with the experimental observations. However, the transverse polarization spectrum has a double peak structure, which was not experimentally observed. The single mode observed in the transverse polarization for the weakly interacting dimer (Fig. 4.3A) is narrower than the transverse mode in the strongly interacting case (Fig. 4.3C). Therefore it is possible that the double peak structure is also present in the experimental data but cannot be resolved.

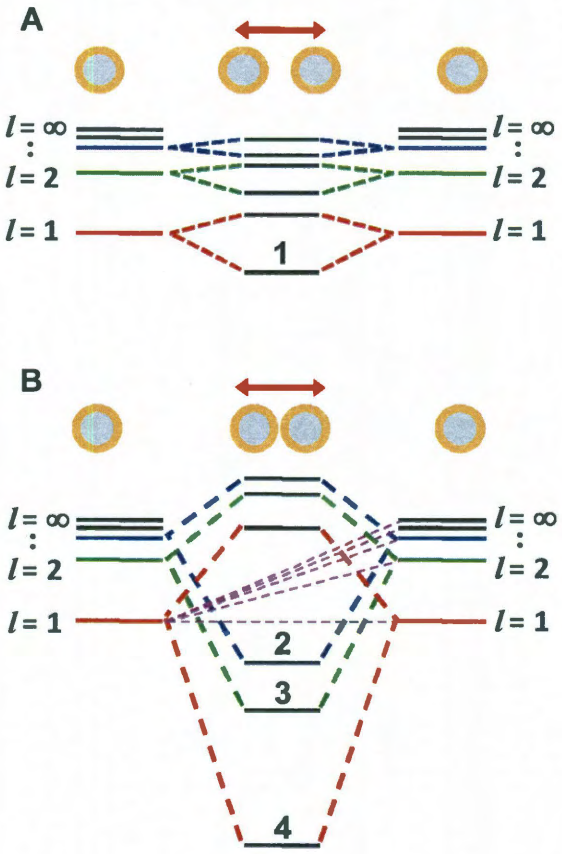

Figure 4.4. Energy level diagram for plasmon hybridization of nanoshell dimers, in the longitudinal polarization configuration. Numbered energy levels correspond to numbered peaks in Figure 4.3. (A) Weakly interacting dimer. (B) Strongly interacting dimer.

Both the plasmon redshift associated with the dimers and the observance of higher order modes can be understood in terms of the plasmon hybridization model.[36,37,91] Schematic diagrams for the plasmon hybridization of nanoshell dimers for these two regimes are shown (Fig. 4.4). While nanoshells themselves are hybridized structures,[36,38] this diagram shows how the bonding dipole modes of each nanoshell hybridize into longitudinal dimer modes. The weakly interacting dimer case, where the two nanoshells

are separated by a relatively large distance, is shown in Figure 4.4A. The weak interaction between the two nanoshells results in only a small splitting of the nanoshell modes into bonding and antibonding levels, which essentially retain the same multipolar index, l, as the nanoshell modes from which they originate. In this regime, only the lowest order dipolar $l=1$ dimer mode (mode 1) is excitable by light because only this mode has a strong dipole moment. However, as the interparticle distance is decreased and the interparticle coupling increases, the splitting into bonding and antibonding modes becomes much larger than for the weak interaction case (Fig. 4.4B). Also, due to the lack of spherical symmetry of the dimer geometry, the normal modes associated with each individual nanoshell are no longer normal modes in the reference frame of the other nanoshell. Thus the increased interaction between the two nanoshells results in the mixing (hybridization) of different multipolar order plasmons such that each dimer mode contains an admixture of different l nanoshell modes (illustrated by the dashed purple lines in Figure 4.4B). Despite the differences in energy between these modes, at small separation distances, they can interact significantly at small separation distances.[37,91] This increased coupling has two consequences. First, the lowest order plasmon mode (4) redshifts much more strongly than a dipole-only interaction would allow because it is, in a sense, repelled by all of the modes with which it interacts. Also, higher order dimer modes can now be excited by light due to the mixing of higher order modes with the dipolar modes of each nanoshell. These higher order features correspond to peaks 2 and 3 in the longitudinal spectrum of Figure 4.3C.

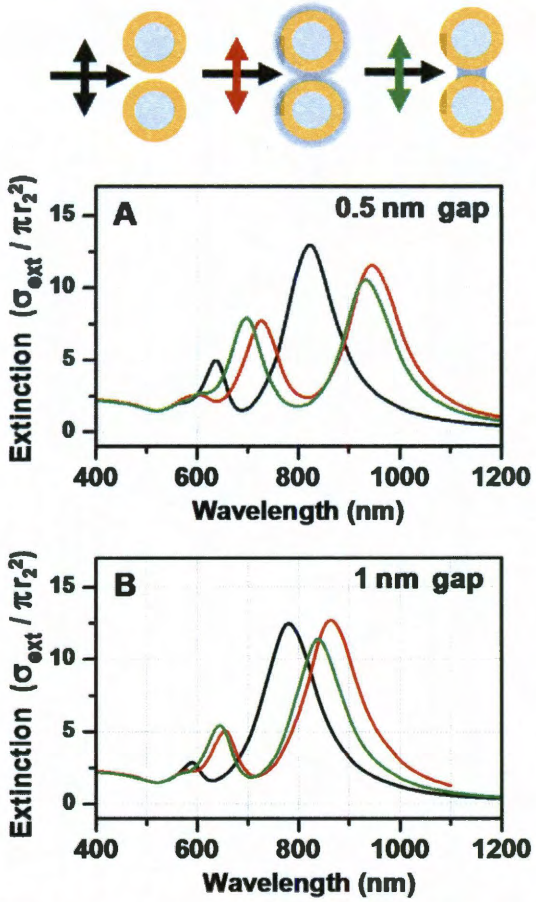

Figure 4.5. BEM calculations comparing the LSPR shift for nanoshell (longitudinal polarization) for three cases of dielectric surroundings: in vacuum (black), with a dielectric medium both in the interparticle junction and surrounding the outside of the nanoshells (red), and with the dielectric medium only inside the interparticle junction (green). Simulations use the nanoparticle sizes for the dimer in Figure 4.3C but with a slightly flatter gap size D of (A) 0.5 nm and (B) 1 nm.

In nanoshell dimers, the dielectric screening introduced by the molecular linker in the junction between the nanoparticles is remarkably large. In our simulations we can examine the relative contribution of this molecular layer to the bare coupled-nanoparticle case (Fig. 4.5). Here the strongly interacting nanoshell dimer case is shown for two interparticle distances of 0.5 nm and 1.0 nm, respectively. For each case, the dimer plasmon spectra are modeled with and without the dielectric spacer layer. Here we can

see quite clearly that the dielectric layer results in a very large redshift compared to the bare dimer case, an effect that increases with decreasing interparticle distance. In our simulations we also examine the extent to which local changes in the dielectric function in just the junction region contribute to this additional dielectric redshift. This corresponds to "loading" the interparticle junction with molecules, as in surface-enhanced spectroscopy applications. The calculation is performed by adding a finite dielectric volume confined to the junction and comparing this to the case of a complete dielectric coating for the dimer. For an accurate comparison of spectral shifts due to molecular screening, the geometry of the gap is kept exactly equal in the three cases, therefore shifts due to conformational differences can be completely discarded. Figure 4.5 shows that by far most of the redshift (90%) is due to the dielectric screening mediated by the molecules within the interparticle junction, with the molecules exterior to this region barely contributing to the shift. This observation has extremely important implications for the design of junction-based SERS or SEIRA sensors.[80] For SERS, the plasmon linewidth must span the frequencies of the Raman excitation laser and the excitable Stokes modes of the molecules; for SEIRA the plasmon frequencies must correspond directly to the dipole-active vibrational modes of the adsorbate molecule. Such large plasmon shifts that occur in this geometry must be accounted for when designing a nanosensor substrate, or the presence of the analyte molecules themselves will "detune" the plasmon resonance from the source. This highly sensitive effect may also be exploitable in the design of SPR sensors based on plasmonic junctions for single or few-molecule detection.

4.4 Nanoshell Peanuts

The nanopeanut geometry allows us to experimentally investigate nanoshell dimers in the unusual "merged" regime, in comparison with the nontouching dimer regime. Two cases of nanopeanuts, differing in degree of overlap, were examined (Fig. 4.6). For each case, the unpolarized spectrum contains two major peaks, which resolve into one redshifted longitudinal mode and a transverse mode located at shorter wavelengths. The two examples differ, however, in the size of the redshift of the longitudinal plasmon. When the overlap between the two nanoshells is small enough that a significant layer of gold separates the two cores from touching each other (Fig. 4.6A), the longitudinal plasmon remains strongly redshifted with respect to a monomer. Here, this mode was positioned at 820 nm, corresponding to a core separation of 8 nm (D = -20 nm) as fit using BEM calculations (Fig. 4.6B). We note that for this nanopeanut, the two constituent nanoshells do differ in size, but the degree of overlap plays a more significant role in determining the spectrum since the plasmon is highly localized in the junction region.[92] In our second example (Fig 4.6C) the ESEM image indicated that little or no gold separated the two cores. The longitudinal mode at 740 nm is therefore blueshifted in comparison to the previous case. The calculations fit the data very well in both cases, reproducing the positions of the longitudinal mode as well as the transverse mode, which lends confidence to the accuracy of the obtained D values. Despite the fact that one can generally distinguish a core and a shell in the contrast of the ESEM images, the precise separation distance between the cores inside a peanut cannot be determined from the images. It is interesting to note that, in this case, fitting the plasmon spectra with simulations provides the best route to determine this information. These two cases are

consistent with our picture of the merged regime, where the longitudinal plasmon blueshifts as the overlap of a nanopeanut increases, in agreement with previous theoretical[92] and experimental[86] findings for solid merged nanoparticles.

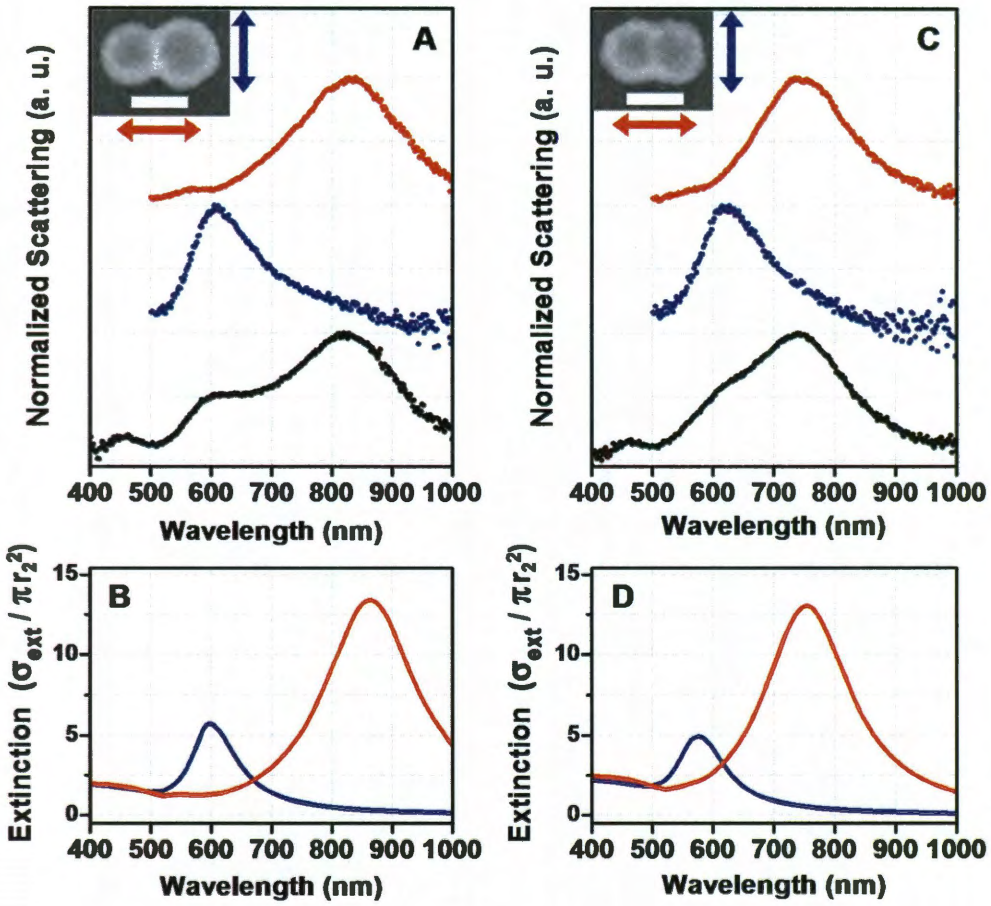

Figure 4.6. Normalized scattering spectroscopy of nanoshell peanuts. Black spectra correspond to unpolarized illumination; blue and red spectra correspond to polarization arrows of the same colors in the insets. Inset ESEM images show the specific peanuts for the presented data (scalebar = 100 nm). (A) Experimental data for a peanut with a relatively large separation distance between the two cores. (B) BEM simulations fitting data in A. This peanut was fitted where the leftmost shell is (r_1, r_2) = (44 , 58) nm and the rightmost shell is (r_1, r_2) = (51 , 65) nm and D = -20 nm corresponding to a core separation of 8 nm. (C) Experimental data for a peanut where the cores are almost touching. (D) BEM simulations fitting data in C. This peanut was fitted where both shells are (r_1, r_2) = (42 , 58) nm. D = -30 nm corresponding to a core separation of only 2 nm. Simulations are normalized to the physical cross section of a nanoshell.

In Fig. 4.7, we show the evolution of the longitudinal plasmon frequencies of two nanoshells as their separation D is reduced from positive to negative (overlapping) values. For nontouching dimers, the dipole peak redshifts and higher order modes begin to appear for the short separations. When the two shells cross over into the merged regime (negative D), the longitudinal mode starts to blueshift. The trends of both the nanoshell dimer and the peanut are consistent with the previous studies concerning solid metal nanoparticles.[86,92]

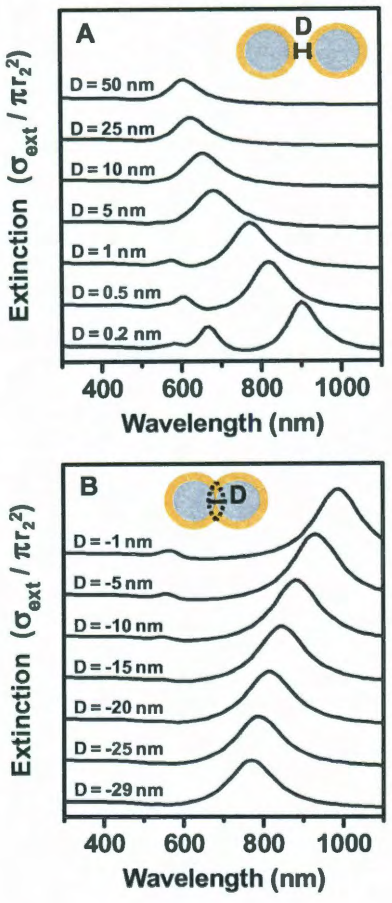

Figure 4.7. Boundary element method simulations for nanoshell dimers (A) and nanoshell peanuts (B). The constituent nanoshells have (r_1, r_2) = (40 , 55) nm. The distances D between the constituent nanoshells are listed for each spectrum. For dimers, D represents the separation distance between the two nanoshell surfaces. For peanuts, D represents the amount of overlap of the metal shells, and is therefore negative. Extinction cross sections are normalized to the physical cross section of a single nanoshell.

4.5 Conclusion

In conclusion, using polarization-dependent single nanostructure spectroscopy we have investigated the plasmon resonances of two nearby nanoshells as their separation is reduced from the nontouching to the touching regimes. The position and shape of the scattering spectra are found to be dramatically different in these regimes. In the nontouching regime, dimer plasmons are formed through hybridization of the individual multipolar nanoshell plasmons with each nanoparticle remaining neutral. For large separations, the spectra exhibit a single polarization-dependent resonance that can be identified as a bonding dimer resonance formed from the hybridization of the dipolar resonances of each nanoshell. For two nontouching nanoshells placed at close proximity to each other, the spectra exhibit several higher multipolar dimer resonances that become dipole-active through the mixing with the dipolar plasmon resonances of the individual nanoshells. In this regime, the dimer plasmons exhibit a remarkable sensitivity to the presence of dielectric media in the junction. When the nanoshells are touching, the spectra exhibit a single plasmon resonance which involves electrons flowing between the two particles. This charge transfer plasmon is found to blue shift as the nanoshells move closer together. The large variations in optical response due to slight conformational and environmental changes revealed in this study will transform this canonical structure into a very versatile system for plasmonic sensing and spectroscopy.

Chapter 5: Fano Resonances in Coupled Plasmonic Nanoclusters: Geometrical and Chemical Tunability

5.1 Introduction

The coupling between metallic nanoparticles in aggregates supports collective electronic oscillations, known as surface plasmons, of the entire structure: this is a topic of intense current interest.[23] Each type of nanoparticle cluster, such as a nanoparticle dimer,[104-106] trimer,[107-109] quadrumer,[110,111] tetramer,[112] etc.,[113-117] exhibits its own unique set of collective plasmon modes arising from the interaction between the plasmons supported by each nanoparticle in the cluster. These collective plasmon modes can be excited at distinct energies that depend on the relative phase of the plasmon oscillations in the individual nanoparticles of the complex. Since surface plasmons are well described as classical oscillators with resonances at optical frequencies, interacting nanoparticles are in essence systems of coupled oscillators, supporting a rich array of phenomena, such as electromagnetically induced transparency (EIT) and Fano Resonances (FRs).[118-125] Geometries ranging from mismatched nanoparticle pairs,[105] "dolmen" structures,[48] coupled ring-disk systems,[25,26,28] heptamers,[22,23,51,126] and layered nanoparticles,[49] have all been shown to support EIT and FRs. Because the coherent coupled oscillator response is essentially an interference phenomenon dependent upon the relative phase of the constituent oscillators, it is highly sensitive to perturbations such as symmetry breaking, local variations in geometry, and dielectric environment.[22,25,27] This inherent sensitivity has spurred interest in these systems of coupled structures, which promise to provide a higher sensitivity optical response than simple plasmonic systems.

Here we examine how the coherent properties of a nanoscale plasmonic cluster are affected by cluster size, geometry, and local dielectric environment. Our study focuses primarily on the seven-member, "heptamer", cluster. We examine the important case of how local changes in dielectric environment modify the frequency of the FR of the cluster. Heptamers have been predicted to have extremely large spectral shifts of their FR induced by changes in the surrounding refractive index.[22] Here, we show that, as predicted, the FR in heptamers exhibits an unusually large shift with changes in refractive index; in fact, this structure exhibits the largest localized surface plasmon resonance (LSPR) response of any known nanostructure, assessed in terms of the figure of merit (FoM) of the cluster aggregate.[13,46]

5.2 Methods

The plasmonic structures investigated here were fabricated by electron beam lithography and are composed of 30 nm thick Au disks on a 1 nm Ti adhesion layer, evaporated onto a Si substrate coated with a 100 nm thick silicon dioxide layer. The dielectric permittivity of the substrate is therefore similar to a typical glass substrate since the oxide layer is thick enough that the plasmonic near-field does not interact with the underlying Si. In Figure 5.1 we show the scattering spectra of three heptamers of increasing size. As can be seen from the SEM images of the clusters in the top panels, the dimensions of the particle radii are increased while the gap sizes are kept constant at ~15 nm (Fig. 5.1(A-C)(i)). The scattering spectrum of each cluster was collected using dark field microspectroscopy (Fig. 5.1(A-C)(ii)). (The microscope used was a Zeiss Axiovert 200 MAT, the CCD was a Princeton Instruments Pixis 400 BR, and the spectrograph was

an Acton 2156i imaging spectrograph.) The specific microscope objective used was critical to our ability to observe the FR. For all of the data reported here, the objective characteristics were: angle of incidence = ~50 degrees from the surface normal, numerical aperture (NA) = 0.4. The FRs were not as pronounced when using objectives with a higher incidence angle or numerical aperture. Because these structures are not in the quasistatic limit, retardation effects are present when light is incident from large angles, with respect to the substrate normal. In this case, the retardation effects allow direct excitation of the subradiant mode, effectively limiting the interference effect that causes the Fano resonance. This Fano interference effect is described below in detail.

Theoretical scattering spectra for these structures were obtained using the Finite-Difference Time-Domain (FDTD) method (Fig. 5.1(A-C)(iii)). The dielectric function used to model Au was obtained from the experimental data of Johnson and Christy (JC).[101] The clusters were simulated on an infinite dielectric substrate with $\epsilon = 2.04$ in order to represent the experimental supporting substrate, and illuminated with oblique incident light. The back scattered light in the simulation was recorded over a conical solid angle corresponding to the numerical aperture of the objective lens used in the experiment.

The optical properties of symmetric plasmonic heptamers composed of spherical and cylindrical nanoparticles have been analyzed and described in several recent publications.[22,23,51,126] The symmetry group of the heptamer is D_{6h}. Using the plasmon hybridization concept, the plasmon modes can be classified according to their irreducible representations. The collective modes that can couple efficiently to light are the E_{1u} modes. The two relevant modes for Fano interference are (1) a bonding bright

(superradiant) mode where the dipolar plasmons of all nanoparticles oscillate in phase and in the same direction, and (2) an antibonding dark (subradiant) mode, where the dipolar moment of the center particle opposes the dipole moment of the surrounding ring. In the quasistatic, nonretarded limit, the dark mode possesses nearly no net dipole moment and does not easily couple to light. In the retarded limit, the bright mode becomes superradiant, while the dark mode remains subradiant. Also in this limit, the weak coupling mediated by the plasmonic near field introduces an interaction between the sub- and super-radiant modes, inducing a FR in the superradiant continuum at the energy of the subradiant mode. Due to its D_{6h} symmetry, the optical properties of the cluster, including its FR, are isotropic, i.e., independent of the orientation of the in-plane polarization of light incident on the structure.

5.3 Fano Resonances in Plasmonic Heptamers

Figure 5.1 shows the evolution of the scattering spectrum of a heptamer as the cluster is scaled up from the near-quasistatic to the fully retarded limit. The Fano minimum is strongly dispersive towards lower energies with increasing cluster size, and the Fano lineshape becomes broadened. The smallest heptamer (A) exhibits a relatively narrow plasmon resonance near 700 nm, which is the bright superradiant bonding E_{1u} mode. Since the overall structure size is small, this mode does not radiate strongly and is quite narrow. Only a very weak FR appears in the theoretical spectrum, and appears only as a weak modulation (at nominally 690 nm) in the experimental spectrum of the cluster. For the intermediate size heptamer in (B), the bright mode is redshifted to approximately 750 nm and significantly broadened due to the increased radiation damping. The FR at

750 nm is now very pronounced. For the largest heptamer (C), the superradiant mode shifts to nominally 900 nm and is dramatically broadened. A strong FR is induced at 900 nm. For a heptamer this large, the subradiant mode radiates slightly, resulting in a slight broadening of the linewidth of the FR. Interestingly, the subradiant mode appears to redshift slightly more strongly than the superradiant mode with increasing size of the heptamers. This effect likely occurs because the subradiant mode consists of an admixture of higher order modes, while the superradiant is mostly dipolar in nature. Due to this stronger hybridization of higher order modes, the subradiant mode redshifts more strongly than the superradiant mode for increasing size of heptamers.

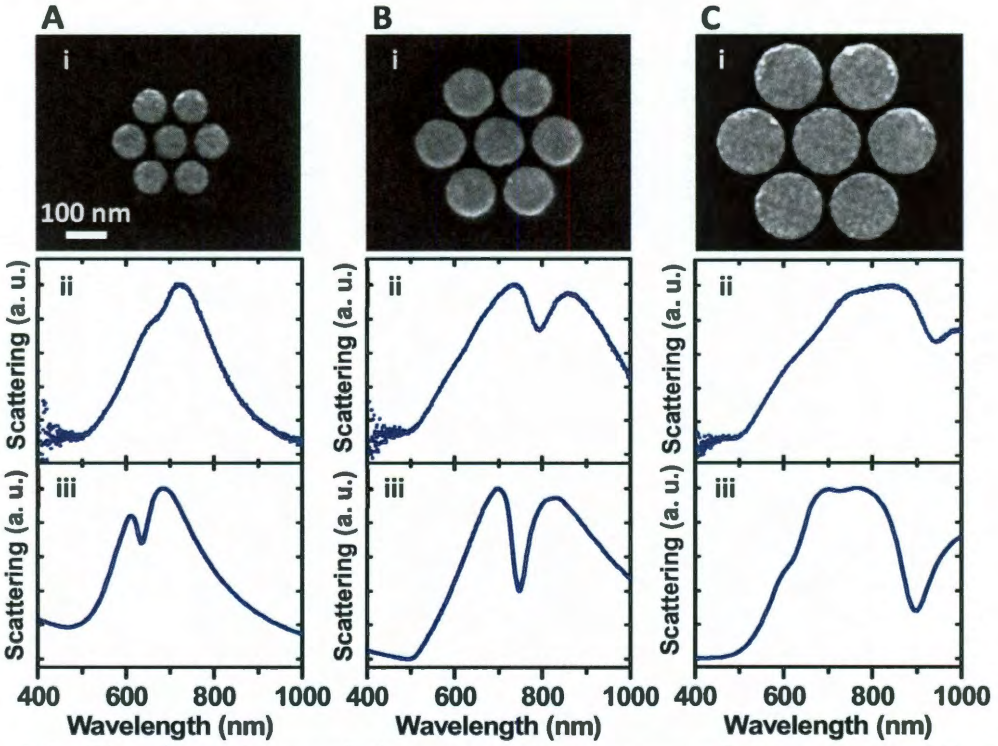

Figure 5.1. Size dependence of the scattering spectrum of a heptamer: (A) 85 nm diameter constituent particles; (B) 128 nm diameter particles; (C) 170 nm diameter particles. In all cases, the gap sizes between the particles in the heptamers were nominally ~ 15 nm.(i) SEM images obtained using an FEI Quanta 400 SEM. (ii) Experimentally obtained dark-field scattering spectra, obtained with unpolarized light, of each individual cluster shown in (i); (iii) FDTD calculations of the dark-field spectral response of the same structure.

In Figure 5.2, an example of the effect of symmetry breaking on the optical spectrum of the heptamer is shown. One of the peripheral particles of a heptamer is removed, resulting in an incomplete ring of nanostructures surrounding the center particle. The optical response of this reduced symmetry structure is no longer isotropic. To study the polarization dependence of the spectral response of this cluster, a rotating analyzer (Zeiss) is inserted in the collection optics of the microscope. Thus, the nanoparticle is still excited using unpolarized light, but the scattered light is polarized just before collection. In Figures 5.2B and C, we show the measured and calculated scattering spectra for different polarization collection angles. As for the case of the isotropic, complete heptamer, the spectrum is characterized by a broad superradiant mode centered around 700 nm. However, with reduced symmetry, the Fano interference displays a more complex behavior. For horizontal polarization (blue), a clear FR appears at 700 nm, and for vertical polarization (red), it appears at 740 nm. For other polarizations, the scattering spectra exhibit a mixture of these two resonances.

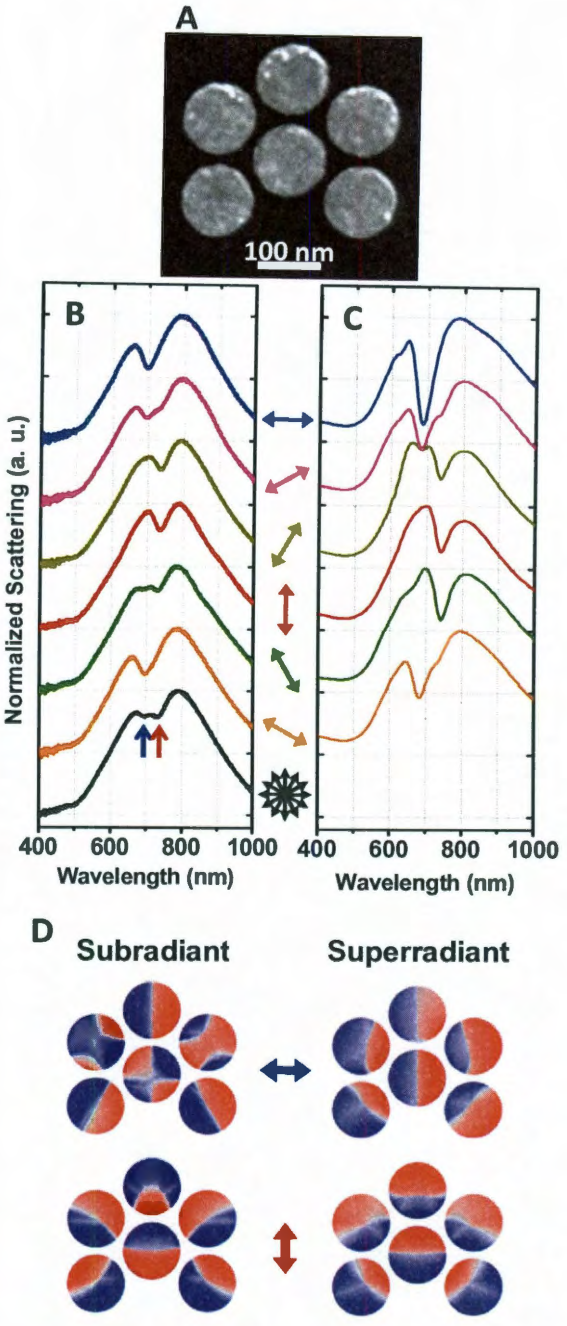

Figure 5.2. Asymmetric Heptamers: (A) SEM image of heptamer. The disk diameters are 128 nm with ~15 nm gaps. (B) Experimental dark field scattering spectra of the asymmetric heptamer, obtained with unpolarized incident and polarization-analyzed scattered light. Colored arrows show the polarization angle with respect to the particle, as in the SEM image. Polarized spectra were collected at 30-degree angular increments. Black curve is unpolarized data. (C) FDTD simulations corresponding to the experimental spectra in (B). (D) Charge plots calculated using FEM for the subradiant (left) and superradiant (right) modes, for the two fundamental polarizations of the structure depicted by the arrows.

A calculation of the induced charge densities of this reduced-symmetry cluster reveals the microscopic origin of the unusual split-FR observable in this structure (Fig. 5.2D). These calculations were performed using a commercial (COMSOL) implementation of the Finite Element Method (FEM). For both polarizations, the subradiant charge plots were calculated at the wavelength of the Fano minimum (Fig. 5.2D, left) and the superradiant charge plots were obtained for the maximum at the long-wavelength side of the Fano dip (Fig. 5.2D, right). The superradiant charge plots clearly show that the dipolar components of all constituent particles are oriented in the same direction, resulting in the enhanced radiative damping and resultant broadening characteristic of superradiant modes. For the subradiant modes, however, the charge plots are distinctly different. For horizontal polarization, the subradiant mode has a strong admixture of nanoparticle quadrupoles. Because the nanocluster does not have a symmetry axis along the polarization vector, higher order modes are allowed so that the subradiant mode is mostly quadrupolar in nature. For vertical polarization, the subradiant mode is a dipolar mode, with the in-phase dipolar contribution of the two center particles opposing the dipole moment of the surrounding four particles, similar to the case for the fully symmetric heptamer.

5.4 Fano Resonances in Plasmonic Octamers

Fano resonances can be realized in other symmetric clusters consisting of a center particle surrounded by a ring of particles. The reason for the very pronounced FR in the heptamer (Fig. 5.1) is the almost perfect cancellation of the total dipole moment of the

ring of particles and the (out-of-phase) center particle in the subradiant mode. For a larger ring, such as the homooctamer shown in Figure 5.3(A)(i), the dipole moment of the ring will become larger than that of the center particle. For such a structure, the antibonding mode will have a finite dipole moment and couple efficiently to incident light. The conditions for a FR are thus not satisfied. Neither the experimental nor the calculated spectra in Figure 5.3A show a pronounced FR. However, by making the diameter of the center particle larger, its dipole moment increases. For a sufficiently large center particle, its dipole moment can become equal to that of the surrounding ring. For such a heterooctamer consisting of particles of different sizes, the antibonding mode becomes subradiant, and a strong FR with a very deep minimum, approaching transparency, is induced around 800 nm as shown in Figure 5.3B.

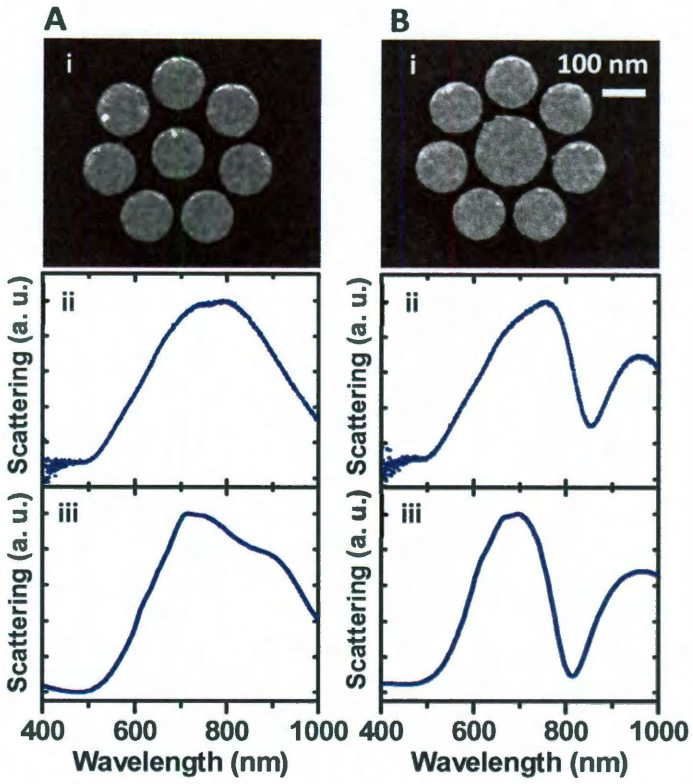

Figure 5.3. Scattering spectra of a octamers. (A) Homo-octamer: SEM image (i), dark-field scattering spectrum (ii) and FDTD simulation (iii). All particles have the same diameter = 128 nm. This results in a gap of ~15 nm between the outer particles and a gap of ~ 40 nm between the inner particle and outer ring. (B) Hetero-octamer SEM image (i), dark-field scattering spectrum (ii), and FDTD simulation (iii). Here, the inner particle was enlarged such that all gaps were the same size (~15 nm). This resulted in an inner particle diameter = 175 nm and the outer particle diameter = 128 nm. All fabrication and data collection procedures are the same here as for Figure 5.1. All data was obtained with unpolarized light.

5.5 LSPR sensing with the Fano Resonance

Much of the current interest in FR in plasmonic system stems from their potential as efficient LSPR sensors.[27,46,127-129] The complex interference phenomena underlying the formation of FRs in coupled plasmonic systems are highly sensitive to the dielectric environment in the junctions of the overall structure. In addition, FRs are typically very

narrow, which allows for a more precise measurement of small peak shifts induced by changes in the dielectric properties of the nanostructure environment. The LSPR efficiency of a plasmonic nanoparticle is typically evaluated by its figure of Merit (FoM), defined as the ratio of the plasmon energy shift per refractive index unit change in the surrounding medium, divided by the width of the spectral peak.[46] For asymmetric FRs, we define the energy of the resonance as the midpoint between the energy of first maximum and the energy of the minimum. The width is defined as the energy difference between those spectral features. This definition for the spectral width used to calculate the FoM has been suggested before[25] and is required because the asymmetric lineshape associated with Fano resonances leads to an ill-defined full width at half maximum (FWHM), as is usually used in the case of ordinary, or peak-like, plasmon resonances.[46] Theoretical predictions for FoM for individual plasmonic nanostructures range from 7 for coupled dipole-quadrupole antennas,[27] 8 for nonconcentric planar ring-disk cavities,[25] to 11 for a symmetric silver sphere heptamer.[22] The recent experimental demonstration of a FoM of 3.8 for a coupled dipole-quadrupole antennas[27] show the tremendous potential for FR-based LSPR sensing.

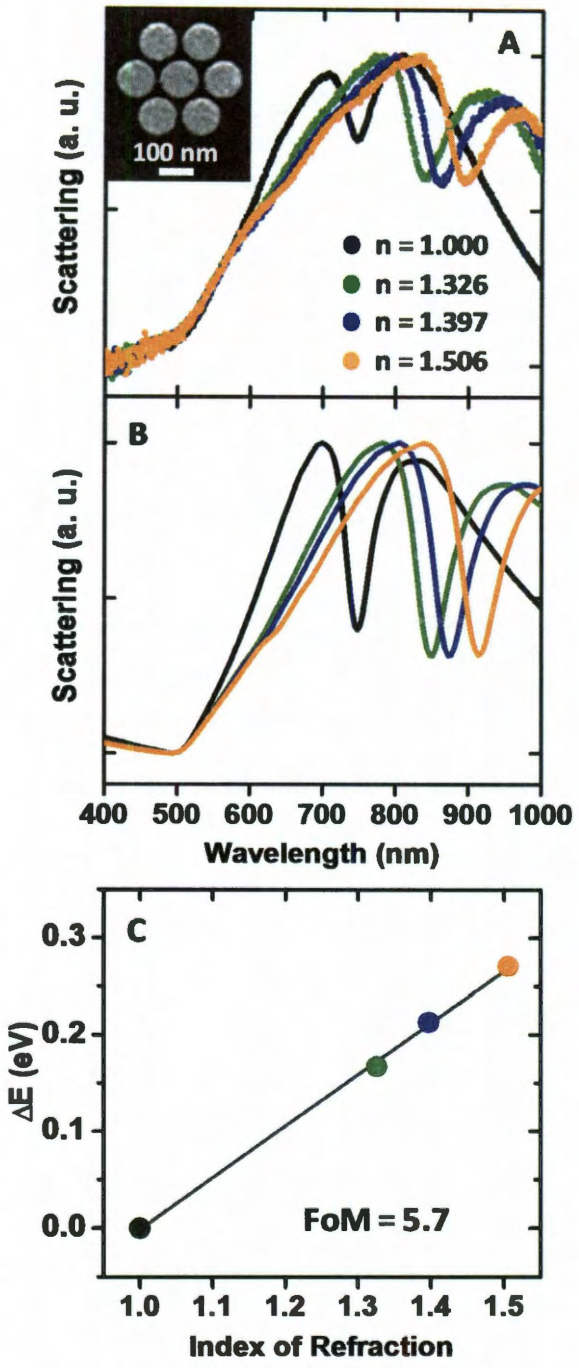

Figure 5.4. LSPR sensing in heptamers. (A) LSPR sensing for heptamer of same dimensions as reported in Figure 5.1. Four polarized scattering spectra are shown for different media (air, black), (methanol, green), (butanol, blue), (immersion oil, orange). The values for the refractive indices of each medium are shown in the figure. (B) FDTD simulations corresponding to the experiment. (C) Linear plot of the LSPR shifts of the FR vs. refractive index of the embedding medium.

To investigate the LSPR sensitivity of the planar heptamer, we performed dark-field scattering spectroscopy on individual heptamers embedded in various dielectric media: methanol (n = 1.326)[130], butanol (n = 1.397)[130], index matching oil (n = 1.506, Cargille Labs internal documentation). For each medium, the entire substrate was first rinsed in that medium, and then fully immersed in the medium in a glass-bottom petri dish (Ted Pella). The scattering spectra were obtained from the immersed samples. Figure 5.4 shows a very pronounced redshift of the FR with increasing refractive index of the surrounding medium. In air ambient, the FR appears at 750 nm, and in immersion oil with a refractive index n=1.5, the FR is shifted to 900 nm. To quantify the LSPR sensitivity, we obtain the slope of the best-fit line (linear regression with a slope = 0.53) for the energy of the FR as a function of surrounding dielectric permittivity, and divide by the Fano linewidth (0.093 eV). The resulting FoM is 5.7, which to our knowledge is the highest LSPR FoM reported so far for an individual finite nanostructure. The FoM calculated from the theoretical simulations (Fig. 5.4(B)) is slightly smaller (5.1). From this we can infer that the nanostructures were likely completely coated by each solvent medium. If this was not the case, the theoretical FoM would be larger than that obtained experimentally.

While this current result indicates great promise for significantly increasing LSPR sensitivities by focusing on FRs, the full potential for FR-based LSPR sensing is clearly not yet realized. In none of the structures studied in these initial experiments has the LSPR FoM been optimized. By using larger structures or structures with narrower gaps, it is highly likely that an even larger FoM can be achieved. Structures fabricated in silver instead of gold, should also yield even larger FoM than those reported here, since the lattice polarizability and electromagnetic screening of silver is significantly smaller than for gold. An advantage with lithographically fabricated clusters such as the present

structure is that the energies of the FRs can be tuned very accurately by varying the ratio of the disk thickness to cluster diameter.

5.6 Conclusion

In conclusion, we have shown that lithographically fabricated nanoscale plasmonic clusters exhibit pronounced FRs, which depend strongly on both the geometry and the dielectric environment of the complex. By changing the size of a heptamer, it is possible to tune the FR to different wavelengths. By symmetry breaking, one can further tune the wavelength of the FR and induce new resonances. A very deep FR, approaching transparency, can be induced in an octamer cluster consisting of a center particle surrounded by a ring of seven particles, if the size of the center particle is sufficiently large. We have also shown experimentally that FRs of heptamer clusters possess exceptional LSPR sensitivities. For a heptamer consisting of seven particles of the same size, we measure a FoM of 5.7. This unparalleled LSPR sensitivity, found in a cluster fabricated by readily available nanofabrication methods, is likely to stimulate increased interest and applications in sensing and detection based on coherent plasmonic phenomena.

Chapter 6: Designing and Deconstructing the Fano Lineshape in Coupled Plasmonic Nanoclusters

6.1 Introduction

Metallic nanostructures can support coherent oscillations of their free electrons, known as surface plasmons, at specific resonant frequencies.[3,131] This is a topic of intense current interest for a range of potential applications, including ultrasensitive chemical and biological sensors,[9,10,132] nonlinear optics,[93,133,134] and solar energy harvesting.[17,135] The route to achieving new and enhanced optical properties based on surface plasmons lies in the coupling of two or more simple plasmonic structures to create unique hybridized plasmon modes. This strategy has been shown to give rise to a wide range of coherent phenomena based on coupled-oscillator physics, such as electromagnetically induced transparency (EIT) and Fano resonances (FRs),[24] universal phenomena observed in systems as diverse as atomic physics, coupled mechanical oscillators and resonant electrical circuits. Coupled plasmonic nanostructures such as ring-disk cavities,[28] "dolmen" structures,[136] multilayer nanoshells,[49] stacked optical metamaterials,[137,138] and planar clusters of nanoparticles[50,51,139-145] have all been shown to support FRs. This behavior arises because these systems support both subradiant and superradiant modes: a subradiant mode has a small or negligible dipole moment preventing it from direct excitation by light, and a superradiant mode with a large dipole moment that is efficiently excited by light. A FR occurs when the subradiant and superradiant modes interact weakly and overlap in energy: this allows the superradiant and subradiant modes to couple and transfer energy to each other, giving rise to the

characteristic Fano lineshape.[146-148] The overall lineshape of these systems, a broadband extinction profile with a narrower spectral window of increased transparency, is a unique characteristic that is quite attractive for applications. For example, plasmonic FRs have been shown to be extremely sensitive to their local dielectric environment, leading to localized surface plasmon resonance (LSPR) sensors with improved sensitivities.[27,28,149] A hexagonally-arranged planar cluster of seven nanoparticles, or heptamer, has been shown to have one of the highest LSPR figures of merit for a nanostructure to date.[149]

Here we examine the plasmonic properties of planar nanoclusters, focusing on arrangements of coupled nanodisks consisting of a central particle surrounded by a ring of peripheral particles. We observe that the depth and width of the FR can be controlled by varying the relative size of the inner particle with respect to the surrounding particles. We also observe that the FR is characteristic of optical excitation of this structure. Excitation by a localized electron beam on various components of the structure does not result in a Fano resonance in the cathodoluminescence spectrum, but instead results in the selective excitation of the center disk mode or the peripheral ring mode of the complex. This contrasting behavior can be understood through the coupling between the superradiant and subradiant modes of the cluster, where the contrasting selection rules of optical and e-beam excitation give rise to different superpositions of radiant modes in the corresponding spectra. In this system, cathodoluminescence allows us to "deconstruct" the Fano resonance into distinct superpositions of superrradiant and subradiant modes not observable by optical means. This analysis gives new insight into the interplay between the subradiant and superradiant modes in coherent plasmonic systems.

6.2 Optical Spectroscopy of Nanoclusters

The plasmonic nanoclusters studied here were made by planar fabrication. Clusters of nanodisks were patterned by electron beam lithography and deposited by evaporation of 30 nm of Au with a 2 nm Ti adhesion layer. The substrate was a silicon wafer coated with a 100 nm thick oxide layer to insure that the plasmons did not interact with the conductive silicon surface. In Figure 6.1B, SEM images are shown of the specific structures, progressing from (bottom to top) heptamer to octamer, nonamer, decamer, and undecamer. The disks in the outer ring of each structure are nominally 85 nm in diameter, and the gaps between all particles are approximately 15 nm. As each new particle was added to the outer ring, the central disk was made larger in order to maintain this gap size and preserve coupling between the particles. Thus the inner particle diameters were 85, 115, 146, 177, and 209 nm for the heptamer, octamer, nonamer, decamer, and undecamer, respectively.

Individual scattering spectra for these structures (Fig. 6.1A) were obtained by dark field spectroscopy, using a homebuilt microscope. Unpolarized white light illumination was focused onto the sample from an angle of ~45 degrees with respect to the substrate normal. This angle was chosen to be just large enough so that no specularly reflected illumination was collected by the objective lens (Mitutoyo, Plan Apo NIR, NA = 0.4). The collected light was polarized by a linear polarizer and focused onto the entrance slit of a spectrograph/CCD (Acton SP2150i/Princeton Instruments PIXIS 400BR excelon) via a tube lens (Mitutoyo, MT-L). Each spectrum was also simulated (Fig. 6.1D) using Finite Difference Time Domain analysis (FDTD, Lumerical). For these simulations, care was taken to match the experimental conditions as closely as possible.

The structures were modeled as 30 nm tall cylindrical Au disks with an experimental dielectric function[101] on a 2 nm thick Ti layer. To include substrate effects,[75,150] the structures were placed on top of an infinite silica slab ($\epsilon = 2.04$). The dark field geometry was taken into account by injecting the excitation and collecting the scattered light at the appropriate angles to match the experimental conditions.

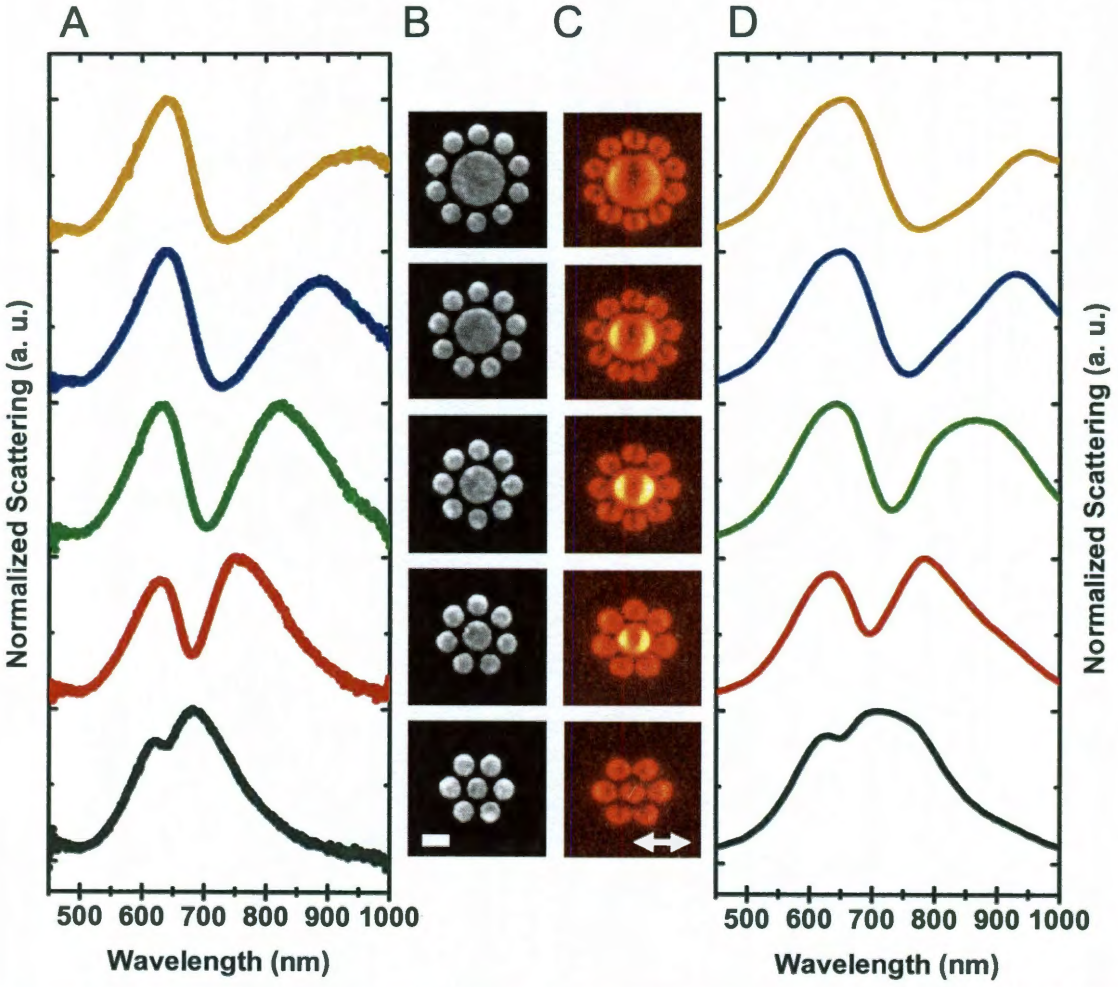

Figure 6.1. Scattering spectra of plasmonic nanoclusters. (A) Experimental dark field spectra of individual structures. (B) SEM images of the structures associated with each spectrum in panel A. Scale bar is 100 nm. (C) Pan-chromatic cathodoluminescence images for the same structures. Arrow indicates polarization of the collected light. (D) Finite difference time domain (FDTD) simulations of the scattering spectra for each geometry.

The experimental and simulated scattering spectra for these structures match each other extremely well. Both show a progression where the Fano resonance dip becomes deeper and broader with increasing size of the central disk structure, from heptamer to undecamer. For the heptamer, the Fano resonance occurs as a narrow, shallow dip at ~650 nm. The dip redshifts slightly and becomes broader and much deeper for the octamer. For the nonamer, the dip has become broader still, but its depth now extends to the baseline, making the nonamer essentially transparent at this wavelength. The decamer and undecamer spectra remain fully transparent at the Fano resonance, but continue to broaden even further. This effect illustrates the possibility of precisely engineering of the lineshape of a plasmonic Fano resonance spectrum, a remarkable prospect for applications requiring precisely controlled and tunable transparency windows. Just as tunable nanoparticles provided a general platform for plasmonic applications across the full optical and infrared spectrum, plasmonic Fano resonances with engineered depths and widths can provide a general framework for applications using Fano resonances.

6.3 Cathodoluminescence Measurements of Nanoclusters

To better understand the origin of the Fano resonance in this family of structures, we studied their response using cathodoluminescence (CL) imaging and spectroscopy.[63,151,152] In cathodoluminescence, the plasmon modes of a structure are excited using a focused, high-energy electron beam (30 keV in this experiment) impinging upon a localized region of choice on the nanoscale complex. The plasmons excited in this manner then radiatively decay and emit light, which is collected by a

parabolic mirror and directed into a spectrograph/detector system (Gatan, MonoCL4 Elite) for imaging and spectroscopy. This allows us to construct excitability maps and spectra which are proportional to the radiative local density of states (LDOS) of the structure.[62]

The polarized, panchromatic CL images of each structure are shown in Figure 6.1C. These images were constructed by changing the optical path of the CL system to bypass the spectrograph, instead routing the radiated light directly to the PMT detector through a linear polarizer. These images allow one to directly access the local density of states of the plasmon modes. In the case of the heptamer, the LDOS on the center particle is similar in strength to the outer particles, but as the center particle size is increased and extra particles are added to the outer ring, the intensity of the central disk becomes markedly stronger. This increase in radiative contribution from the central particle coincides with a deepening of the Fano dip, suggesting the importance of the central particle to the spectral lineshape. As the center particle is made larger, the strength of its induced dipole moment is increased, more closely matching the collective dipole moment strength of the outer ring of particles. This leads to complete destructive interference between the central disk and the outer ring of particles at the Fano resonance wavelength, and therefore complete transparency.

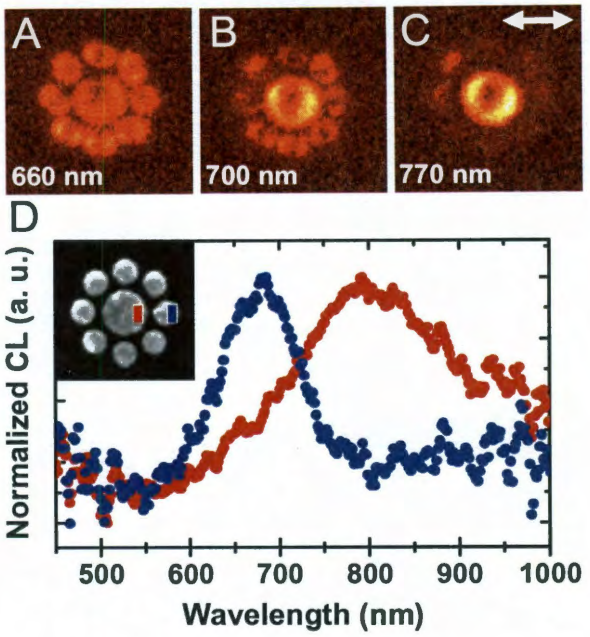

Figure 6.2. Polarized, wavelength-selected cathodoluminescence images of a nonamer at (A) 660 nm, (B) 700 nm, and (C) 770 nm. Arrow indicates analyzer angle. (D) Cathodoluminescence spectra where the electron beam is exciting the center particle (red) and a particle in the outer ring (blue). The inset shows an SEM image of a nonamer with blue and red squares to indicate the location of the beam for the blue and red spectra, respectively.

The panchromatic images shown in Figure 6.1C provide an intuitive visualization of the plasmon resonances at play in these structures. However, they do not provide wavelength-specific information that would permit us to identify the specific plasmon modes giving rise to the radiative response. To obtain this information, we performed wavelength selected CL imaging on the planar nonamer cluster (Fig. 6.2). In panels A, B, and C, we show polarized CL images obtained at the selected wavelengths of 660, 700, and 770 nm respectively. Here it is evident that as we move across the Fano resonance from shorter to longer wavelengths, the contribution of the particles in the outer ring diminishes while the contribution from the central particle increases

dramatically. Furthermore, cathodoluminescence spectroscopy reveals that, under electron beam excitation, there are actually two independent resonances associated with either the center particle or the outer ring (Fig. 6.2D). When the electron beam scans a small region on the side of the central particle (red region denoted in inset image), a lower energy "center particle resonance" is obtained in the spectrum (red), but if the structure is excited by electron beam scanning a small region of a peripheral particle (blue region in inset image), the CL spectrum obtained (blue) shows a higher energy "ring resonance." Most notably, no Fano resonance is observed in the CL response in either case.[153]

6.4 Analysis of Nonamer Modes

By directly comparing the dark field scattering spectrum of the nonamer, obtained with optical excitation, with the two CL spectra, obtained with localized electron beam excitation, we see that the crossover between the two resonances observed in CL is located at the same spectral position as the Fano resonance dip in the dark field case (Fig. 6.3). To understand this behavior, we invoke a coupled oscillator, mass-and-spring model used to describe Fano resonances (Alzar model) (Fig. 6.3B).[53]

A Fano resonance can be understood using the analogy of two masses, each connected to rigid walls by spring constants k_1 and k_2 and connected together by spring constant K . Here the masses represent the superradiant (m_1) and subradiant (m_2) modes while the spring constant K represents the coupling between them. By applying a sinusoidal force to m_1 only and plotting the power dissipated by m_1, a typical Fano resonance lineshape emerges. Here, the dip represents an energy where m_2 is "stealing" the oscillation

amplitude from m_1. This is directly analogous to the Fano resonances observed in plasmonic systems where plane-wave illumination can only excite superradiant modes, but, due to near-field coupling, energy is transferred to the subradiant mode from the superradiant mode at the Fano resonance frequency. During this transfer, the oscillation undergoes a π phase shift, resulting in destructive interference of the superradiant mode, resulting in a Fano resonance, in the spectrum. Thus by choosing the correct parameters for the spring constants and damping rates, the dark field nonamer spectrum (Fig. 6.3A, green) can be reproduced with remarkable agreement by the Alzar model (Fig. 6.3C, green).

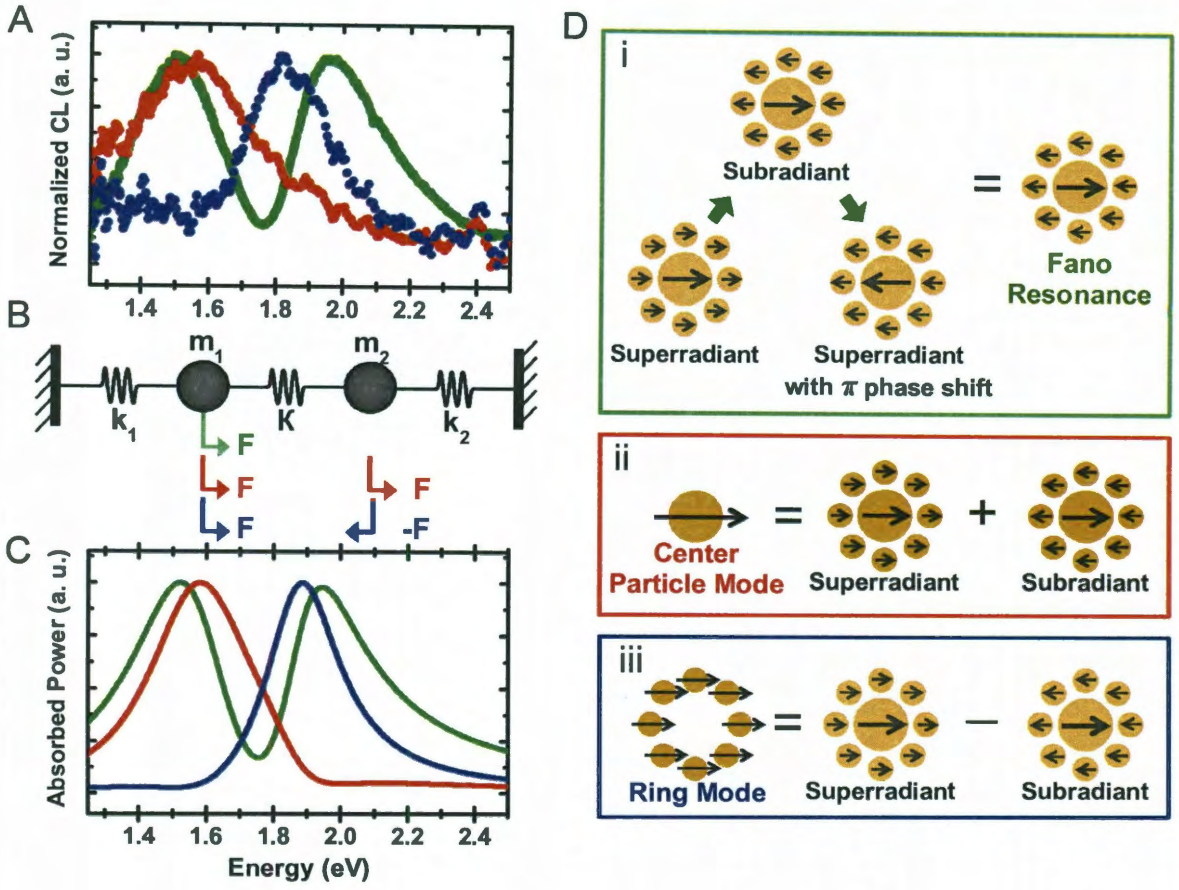

Figure 6.3. (A) Experimental spectra of the plasmonic nonamer plotted in energy units: plane wave excitation (green), excitation by electron beam impinging on an outer particle (blue), and the center particle (red). (B) Schematic representing the coupled oscillator model used to generate the spectra in (C). The arrows (colors corresponding to spectra in panel C) indicate how the forces are being applied in each case. (C) Theoretical spectra using the coupled oscillator model. (D) Schematics for the construction of the nonamer modes present in the case of optical excitation (i) and electron excitation (cathodoluminescence) of the center particle (ii) and the particles in the outer ring (iii). Here the arrows in (i) represent energy transfer between modes while addition and subtraction in (ii) and (iii) represents direct excitation of linear combinations of modes.

This simple picture can also be used to explain why the cathodoluminescence spectra (Fig. 6.3A, blue and red) do not display a Fano resonance. In contrast to plane wave optical excitation which excites the collective modes of the interacting

nanostructure, the localized electron beam will couple predominantly to the localized plasmons in the individual nanoparticle closest to where it impinges. Since the collective modes of the nanocluster can be described as superpositions of plasmon modes of the individual nanoparticles, an electron beam can excite both the superradiant and subradiant modes.[63] This situation is equivalent to simultaneously applying an oscillating force to both masses in our simple mass and spring model. However, an equal magnitude, sinusoidal force can be applied to both masses in two ways: as an in-phase excitation (red) or an out-of-phase excitation (blue). Using these two excitation conditions, we are able to reproduce the experimental CL spectra with exceptional agreement (Fig. 6.3C). Note that the slight redshifts of the experimental CL data, with respect to the coupled oscillator model, is caused by deposition of carbonaceous contamination during the CL experiment due to the high electron beam current. Here, all of the parameters for the masses and springs were kept equivalent to the one-force case (green), and only the excitation conditions were changed. Since in this model the two masses represent the subradiant and superradiant modes of the plasmonic system, applying forces to both masses is analogous to exciting a linear combination of these two modes in the nonamer. We can visualize these three different excitation conditions in the nonamer structure directly. For optical excitation (Fig. 6.3Di), only one mode is excited, but, characteristic of Fano-resonant systems, there is energy coupling between the superradiant mode excited and the subradiant mode of the structure, with energy transfer back to the superradiant mode occurring with a □ phase shift. For CL excitation, when the electron beam impinges on the center particle, the resulting instantaneous dipolar polarization of the disk is equivalent to a symmetric superposition of the sub- and super-

radiant modes and thus equivalent to in-phase driving of the two collective modes (Fig. 6.3Dii). When the electrons impinge on the ring, the resulting instantaneous polarization of the ring is equivalent to an out-of-phase superposition of the two collective modes (Fig. 6.3Diii). It is important to note that both the "ring mode" and the "center particle mode" are coupled modes of the nonamer and not uncoupled modes of the constituent particles. We have performed simulations showing that both of these modes observed in our CL spectra occur at different energies than the plasmon modes of uncoupled disks, identical to either the center or ring particles. This picture can now be applied to the CL images and spectra shown in Figure 6.2. At longer wavelengths, only the central particle is visible in the CL image because the red spectrum corresponds to the in-phase superposition, while at shorter wavelengths, the particles in the outer ring appear dominant because the blue curve represents the out-of-phase superposition. Note that the central disk is still visible in Figure 6.2A because the center particle mode is broad and overlaps with the ring mode at these wavelengths.

6.5 Conclusion

In conclusion, we have examined the plasmonic properties of planar nanoclusters. We have showed that optical excitation of this family of structures results in a Fano resonance with a spectral lineshape that can be precisely controlled, in a sense, "designed", by changes in geometry. By also studying the resonant properties of this structure under localized electron-beam excitation using CL imaging and spectroscopy, we have "deconstructed" the Fano resonance observed under optical excitation of this system. We found that under electron excitation, no Fano resonance is present, but rather

two independent modes appear, one associated with the central particle only and one associated with the outer ring of particles. The overall resonant behavior of this system can be explained using a coupled oscillator model, where optical and electron-beam excitation correspond to distinct excitation conditions in the coupled oscillator picture. This simple and intuitive approach may be useful in understanding, and ultimately predicting, both the optical and CL responses of additional plasmonic complexes.

Chapter 7: Reshaping the Plasmonic Properties of an Individual Nanoparticle

7.1 Introduction

Noble metal-based nanoparticles, whose vivid colors depend upon their plasmon resonances, are widely recognized for their shape-dependent optical properties.[7] The plasmonic properties of complex nanostructures arise from the hybridization of their primitive plasmon modes,[36] a paradigm that enables the predictive design of plasmonic nanoparticle "artificial molecules" with specific optical characteristics.[154] As nanoparticle synthesis and fabrication methods yield nanostructures of greater complexity, these more advanced nanoscale geometries have much to offer emerging new fields, such as optical frequency metamaterials[15,16,155-161] or ultrasensitive LSPR sensing.[26,162] Many of the unique electromagnetic properties of complex metallic nanostructures originate with their reduced symmetry. For example, split ring resonators[14,16,156] have been shown to be important metamaterial constituents due to their ability to support magnetic resonances at microwave frequencies, giving rise to materials with negative permeabilities in discrete spectral regions. While these components are being transitioned to the higher frequency optical regime,[163] new, reduced-symmetry nanoscale architectures that manipulate light in novel new ways are also becoming apparent.[29,30,106]

The family of core-shell metallic nanoparticles provides several paths towards reduced-symmetry nanostructures with tailorable optical properties at visible and near infrared frequencies. Nanoshells (spherical nanoparticles consisting of a dielectric core

and a thin metallic shell layer) support surface plasmon resonances that may be tuned to wavelengths ranging from the visible to the infrared region of the spectrum.[39] Symmetry-breaking in 3D shell and 2D ring geometries leads to large modifications of the plasmonic properties relative to the corresponding symmetric nanostructure.[29-31,54,98,164-168] For example, merely positioning a symmetric nanoparticle in an electromagnetically anisotropic environment, such as on top of a dielectric substrate, lifts the degeneracy of the plasmon modes and results in a splitting of mode energies.[75] Placing a nanoparticle on a metal surface or film allows its plasmon modes to hybridize with the propagating surface plasmons of the underlying substrate, giving rise to additional resonant "virtual state" plasmons at the nanoparticle-substrate junction.[169]

Even more dramatic changes in plasmonic properties result when the nanoparticle morphology itself is altered anisotropically. Increasing or decreasing the thickness of one side of a nanoshell results in a nonconcentric offset of the core with respect to the shell layer, a morphology known as a "nanoegg". [98] In this geometry, the selection rule that allows for the mixing of plasmon modes exclusively of the same angular momentum is relaxed, resulting in the appearance of new plasmon resonances in the optical spectrum.[98,167] A further reduction in symmetry would result in a partial shell structure, or nanocup, where the shell is entirely removed from one side of the spherical nanoparticle core (Fig. 7.1A). This geometry supports the appearance of both "electric" and "magnetic" (electroinductive) plasmon modes, with potential applications as constituents in optical frequency magnetic materials or in metamaterials.[29,30]

Here we examine, at the individual nanoparticle level, the changes in the optical properties of a nanoparticle as we progressively transform its morphology from a

nanoshell to a nanocup. This is accomplished by a unique electron beam-induced ablation process that allows us to carefully and systematically thin the top of an individual nanoshell in a highly controlled manner. By controllable, nanoscale modification of the nanoparticle geometry, we also alter its plasmonic properties. Optical spectra of the individual nanoparticle were obtained as its morphology was reshaped. Polarization-dependent dark-field microspectroscopy was used to probe the plasmon modes of the sculpted nanoparticle. To analyze and interpret our experimental nanoparticle spectra in terms of the plasmon modes supported by that geometry, we utilized finite element method (FEM) modeling of the nanostructure in its various morphologies. This allows us to definitively connect the resonances we observe in our spectra with the plasmon modes supported by this structure. It also enables us to discriminate between those plasmon modes inherent to this nanostructure geometry even in the quasistatic limit relative to those plasmon modes whose excitation relies on phase retardation effects.

7.2. Electron Beam Ablation of Au Nanoshells

The individual nanoparticle reshaping method we report here relies on the electron beam-induced ablation of Au nanoshells under a low pressure H_2O vapor atmosphere (Fig. 7.1a). Au nanoshells were first fabricated as previously reported[39,40] and immobilized in a submonolayer onto a poly(vinylpyridine)-coated glass coverslip, dispersed by spin-coating.[97] In order to facilitate identification of the same specific individual nanoparticle in each successive experimental step, the coverslip was numerically indexed with a Au finder grid deposited by e-beam evaporation through an indexed TEM grid (Ted Pella).[58] Individual nanoshells were then ablated by exposure to a

30 kV electron beam under a 2.25 Torr water vapor environment at an 8 mm working distance, using Environmental Scanning Electron Microscopy (ESEM, FEI Quanta 400). Typically, ESEM allows scanning electron microscopy to be performed on nonconductive samples through the introduction of H_2O vapor into the vacuum ESEM environment to stabilize surface charging,[170] an approach which is quite generally used for imaging nanostructures on nonconductive substrates. By exposing a nanoparticle to the electron beam for a longer time than required for imaging, we can slowly and controllably ablate a portion of the metallic layer of a nanoshell. The electron beam continuously scans a small area (~ 500 nm^2) of the sample containing a single nanoshell, allowing for simultaneous ablation and monitoring of the ablation progress by collection of video frames (where the electron beam scans the surface at a rate such that a single frame is acquired every seven seconds). Several frames from a video sequence showing the ablation of a representative nanoshell are shown in Figure 7.1(b). Here, the upper left frame shows the original nanoshell prior to ablation, while the lower right frame shows the resulting nanocup, after ablation has removed the top portion of the nanoshell. The intermediate frames show the dynamic ablation process from nanoshell to nanoegg to nanocup. The process begins with a decrease in thickness of the shell layer, which can be observed as a subtle reduction in the brightness in the broad central region of the nanoshell image following each subsequent period of ablative processing, as the nanoshell is being reshaped into a nanoegg (Fig. 7.1(b), frames 1, 10, 20, 25). At some point, the metallic layer on the nanoparticle surface begins to open, initiating the transition to a nanocup morphology. First, several separated perforations in the shell layer appear (Fig. 7.1(b), frames 30, 35, 38, 41), which then coalesce into a single continuous

hole with irregular edges (Fig. 7.1(b), frames 44, 47, 50). After additional exposure, this irregular hole transforms into a uniform opening with well-defined edges, resulting in a well-formed nanocup (Fig. 7.1(b), frame 70).

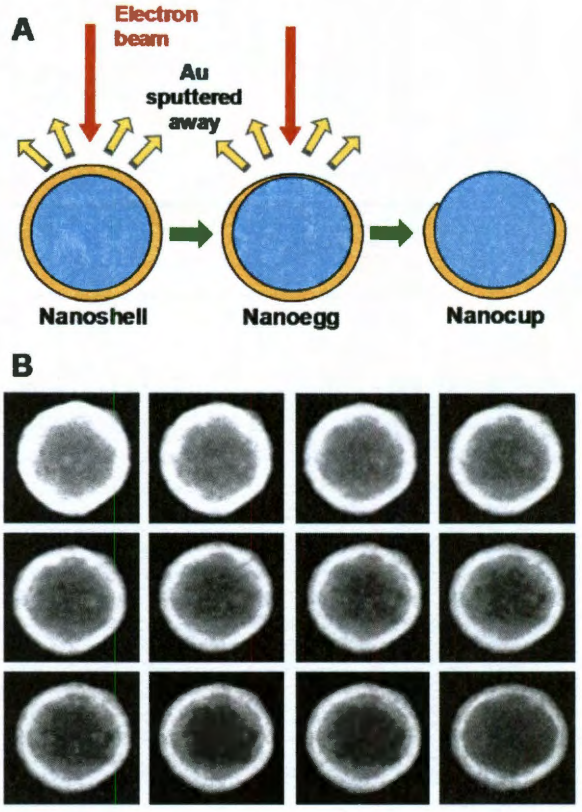

Figure 7.1. Electron beam-induced ablation of Au nanoshells. (a) Schematic illustrating nanoshell ablation process resulting in the transformation of a nanoshell to nanoegg to nanocup. (b) A selected representative sequence from 70 video frames (frame number is indicated in the upper left corner of each image) imaging the transition between the initial nanoshell and the final nanocup, where each frame represents one complete e-beam scan (requiring 7.09 seconds) of a 497 x 430 nm area of the sample. Upper left frame: nanoshell before ablation. The top row (1, 10, 20, 25) corresponds to the reshaping of a nanoshell into a nanoegg. The middle row (30, 35, 38, 41) corresponds to the appearance of small, irregular holes in the metallic shell layer. The bottom row (44, 47, 50, 70) corresponds to the coalescence of multiple small holes into one larger hole, which expands and develops smooth edges as a nanocup is formed. Lower right frame: final nanocup at the end of ablation process.

Several observations of the reshaping process provide information that allows us to deduce certain aspects of the ablation mechanism. This process is observed only for nanostructures on a nonconductive substrate. Therefore it is likely that surface charging and possibly local heating are important in the ablation process, since both local charge and heat dissipate slowly from isolated nanoparticles on a nonconductive substrate. Given the chemical constituents present, it is also not likely that chemical etching is occurring, as would proceed if the electron beam interacted with a reactive gas etchant species.[171-174] The ablation rate we observe is much faster at lower H_2O pressures (<1 Torr) and negligible at higher pressures (max ~4-5 Torr). This also suggests that surface charging plays a dominant role, since the presence of H_2O vapor stabilizes charging in ESEM imaging, and higher H_2O pressures would reduce the amount of surface charge on the sample. For long exposure times, nanoparticles completely disappear, whether they are silica core-gold shell nanoshells or commercially obtained 100 nm colloidal Au nanoparticles (Ted Pella), indicating that it is ablation, not melting, that occurs during the reshaping process. Where the interparticle separation is less than 1-2 microns, nearby nanoparticles not in direct contact with the e-beam can also be partially ablated, indicating that the highly focused e-beam itself is not the sole source of ablation. It is likely that both the electron beam and ionized H_2O molecules,[170] formed by interactions of the electron beam with the ambient H_2O vapor, induce localized ablation. A possible scenario is that the incident electron beam induces a net negative charge on the nanoparticle surface, which then attracts the positively charged H_2O ions to the nanoparticle, resulting in the sputtering of material from the nanoparticle. While further experiments would be needed to prove this mechanism definitively, it is important to note

morphology is accompanied by a dramatic spectral change, where two distinct peaks are now evident in the spectrum, one positioned at 700 nm in wavelength and the other near 890 nm. The following two ablation steps correspond to a reshaping of the cup to a more uniform, semishell structure, accompanied by modest blueshifts of both observed spectral features to 660 and 820 nm, and an increasing in intensity of the longer wavelength mode, until it is the dominant mode of the final nanocup (vi).

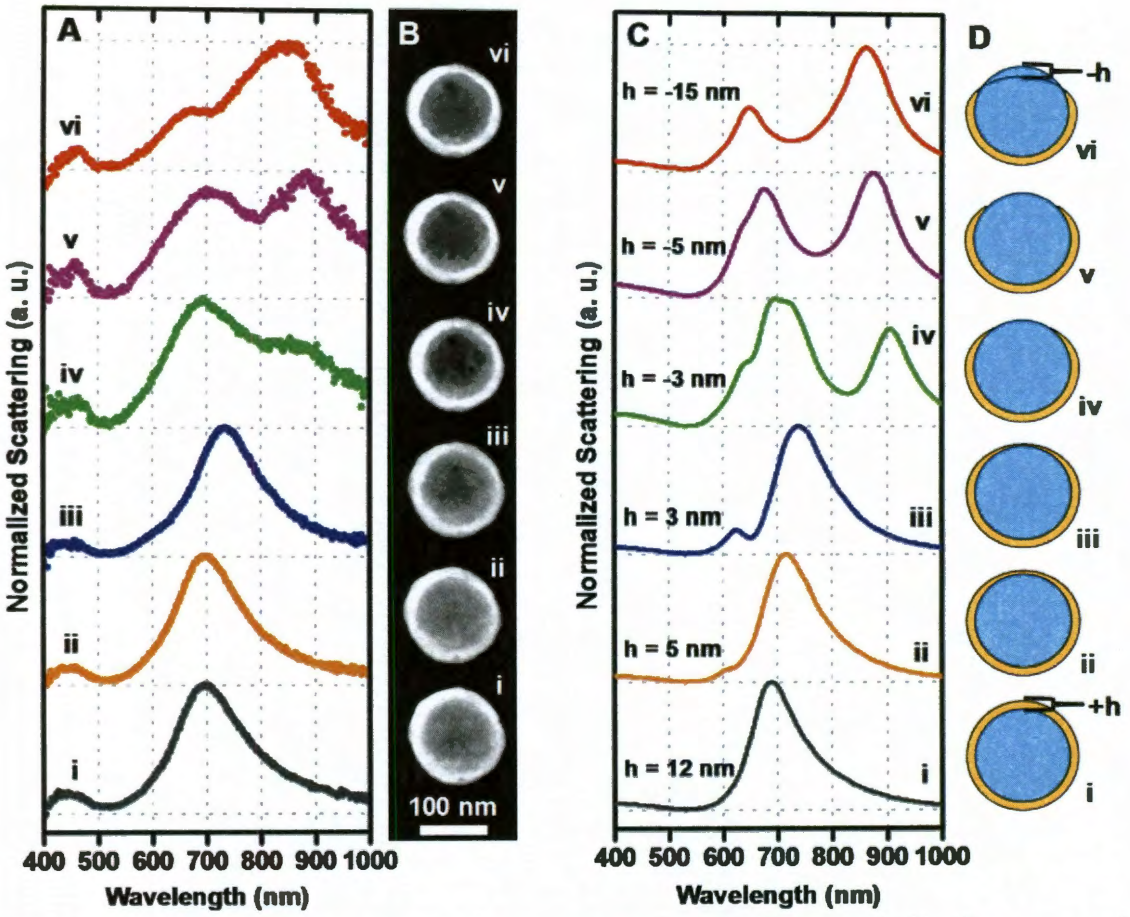

Figure 7.2. Scattering spectra and geometry of a single nanoshell after successive ablation steps. (a) Experimental scattering spectra after successive ablation steps. (b) ESEM images (i - vi) of the nanoparticle morphology corresponding to scattering spectra (i – vi) in part A. (c) Theoretically obtained spectra (Finite Element Method) corresponding to experimental spectra in a. (d) Schematic of simulated geometries corresponding to spectra shown in c.

To obtain greater insight into the relationship between morphology and plasmon response, finite element method simulations (COMSOL Multiphysics, Inc.) were performed on geometries corresponding to the modified nanostructures, consistent with the SEM images obtained during the ablation process (Fig. 7.2(c, d)). Simulations were performed using the empirical, bulk dielectric function for the Au shell[101] and $\epsilon = 2.04$ for the silica core. The conditions of the simulation were selected to closely match the experimental geometry observed in the SEM video images, as well as the geometry for optical excitation by unpolarized dark-field scattering spectroscopy.[58,175] The illumination is incident at 75° from the substrate normal and polarized 45° between the S and P-polarizations in order to reproduce the experimental unpolarized spectra. For simplicity, the substrate material was set to have a vacuum dielectric. The scattered light is collected only in the solid angle above the particle corresponding to the 0.9 numerical aperture objective used in the experiments. First, theoretical agreement with the pristine nanoshell spectrum was obtained, to determine as accurately as possible the precise nanoshell geometry from which the ablation-sculpted nanoegg and nanocup were formed. For this initial nanoparticle, an inner core radius of 68 nm and an outer shell radius of 80 nm agreed most consistently with the spectrum and the measured nanoshell morphology (SEM image) within experimental uncertainties. Next, nanoeggs were modeled by thinning the nanoshell on one side of the structure, flattening the upper half-sphere of the Au shell layer (Fig. 7.2d(ii, iii)). The resulting spectra for this geometry agree very well with the experimental spectra. For the thinnest nanoegg (iii), both the redshift of the dipole mode to 725 nm and the appearance of a higher order shoulder near 600 nm, resulting directly from the additional mode-mixing due to symmetry breaking,[98] were

reproduced well in the simulated spectra (Fig. 7.2c(iii). Agreement between theoretical and experimental spectra indicate that the metallic shell layer of the nanoegg is only 3 nm thick at its thinnest point for this nanostructure, which appears to be the minimum thickness experimentally achievable prior to an opening of the metallic shell layer. Despite the modest spectral changes, significant electromagnetic field enhancements just outside the thinnest region of the shell layer may already be present in this geometry (E/E0 ~ 23 for the proximal minimal-shell-thickness region of this specific nanostructure).[167] These large enhancements may be useful in SERS applications, especially in a configuration like that reported here, where the thin side of the nanoegg is facing up, and therefore the large electromagnetic fields are easily accessible at the open surface. However, the thin shell regime is also where quantum effects should become important, which may be responsible for significant reductions in the classical predictions of enhanced electromagnetic fields [176].

To simulate the nanocup spectra (iv-vi), the nanoegg simulation geometry was altered by further flattening the shell half-sphere such that it lies below the surface of the core on one side by 3 nm (iv), 5 nm (v), and 15 nm (vi) creating a "hole" in the shell, in qualitative agreement with the SEM images (Fig. 7.2b(iv-vi)). In order to avoid numerical artifacts due to unphysically sharp edges, the rim of the nanocup was truncated by 5 nm and given a 0.5 nm radius of curvature (iv) or was truncated by 10 nm and given a 1 nm radius of curvature (v, vi). The simulated nanocup spectra (Fig 7.2c (iv-vi)) show excellent agreement with the observed experimental spectra (Flg 2a(iv-vi)). Each of the simulated spectra has two dominant peaks, both of which blueshift as the cup opening becomes larger. Also, as the nanocup evolves to its final morphology, the relative

intensities of these two peaks change, a behavior observed in both the experimental and theoretical spectra with very good agreement.

7.4 Analysis of Nanocup Plasmon Modes

To assign the observed spectral resonances to the plasmon modes supported by a nanocup, polarization-dependent dark-field microspectroscopy (Fig. 7.3) was performed on the final nanocup morphology shown in Figure 7.2(b(vi)). The unpolarized spectrum (Fig. 7.3, gray) shows two peaks near 820 nm and 660 nm in wavelength, just as in Fig. 7.2(a(vi)), yet probing the nanostructure with polarized light reveals that these modes are anisotropic. (Here polarization will be defined as P- or S-polarization with respect to the substrate beneath the nanocup.) For S-polarized incident light (red), the electric field is polarized transverse with respect to the axis of symmetry of the nanocup. Only the redshifted (~820 nm) peak is excited in this orientation, confirming its assignment as a transverse plasmon mode. For P-polarized incident light (blue), both peaks of the unpolarized spectrum remain observable, a consequence of the dark-field geometry. Because the k-vector of the incident light is oriented at 75° from the substrate normal, P-polarization contains a mixture of both the axial (parallel to the nanocup axis of symmetry) and transverse orientations of the electric field. Since the 660 nm peak is not observable with S-polarized incident light but is observable with P-polarized light with a significant component of the E field along the axis of symmetry of the nanocup, this spectra feature corresponds to the nanocup axial mode.

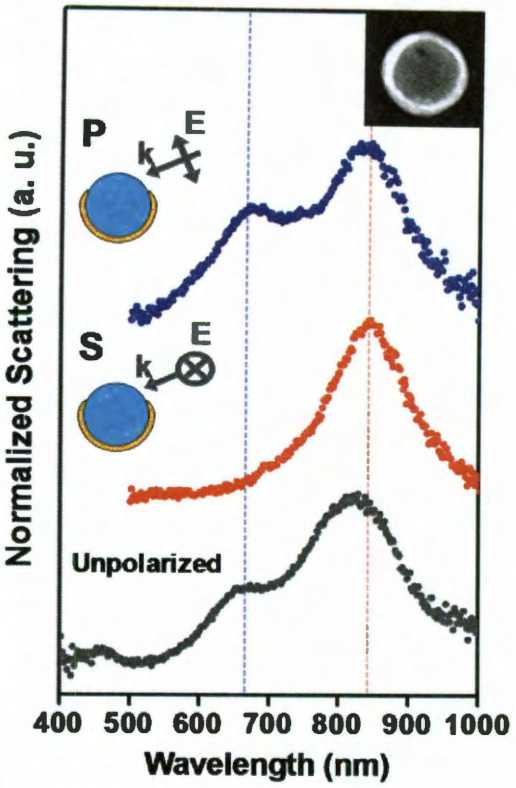

Figure 7.3. Polarization-dependent optical scattering spectroscopy of a single nanocup. Bottom: Unpolarized spectrum. Middle (top): spectra taken with S (P) polarized illumination, where associated schematic diagrams illustrate the orientation of the incident **k** and **E** vectors, as viewed from the side. Inset: ESEM image of the nanocup.

Simulations of the nanocup plasmon response conducted with polarized incident light reveal a great deal more information about the plasmon modes of nanocups (Fig. 7.4). Here, illumination is incident such that **k** is oriented perpendicular to the nanocup axis of symmetry, and **E** is either aligned in the pure axial or transverse polarization. By calculating the scattering and absorption spectra of an experimentally realized nanocup geometry (the same geometry used in Figure 7.2d, vi) for both transverse and axially polarized incident excitation (Fig. 7.4a, b respectively), it becomes evident that more modes are present than are observable in our dark field measurements, which measure the polarization-dependent scattering, not absorption, spectra. For both polarizations, the

corresponding absorption spectra reveal three distinct peaks, for which the plasmon modes may be assigned by examining the charge distribution at the surface of the nanocup (Fig. 7.4c, d), plotted in several orientations as defined by the **k**, **E**, and **H** vectors shown. In order to evaluate the surface charge on the metal-dielectric boundaries, Gauss's law was applied to the E-field near the boundary to account for both the bound and free surface charge densities. The surface charge density may be expressed as $\sigma = (\boldsymbol{E}_d - \boldsymbol{E}_m)\cdot\boldsymbol{n}_\sigma$, or the difference between the normal components of the electric field above and below the metal-dielectric boundary.[177] In order to show the correct charge configurations for each mode, the phase of the solution was swept at each peak wavelength to find the maximum local charge. Both the transverse mode at 854 nm and the axial mode at 649 nm are the dipolar modes (l = 1, two distinct charge lobes) observed experimentally in the polarized scattering spectra (Fig. 7.3). The broken symmetry of the nanocup geometry relaxes the threefold degeneracy of the dipole mode for a spherically symmetric nanoparticle, splitting it into the two observed dipole modes, one transverse at 854 nm and one axial at 649 nm. A physically intuitive understanding of this splitting may be obtained by noting that like charges around the rim of the nanocup tend to repel each other, blueshifting the axial dipole, whereas the transverse dipole occurs at a lower energy because opposite charges at the rim tend to attract each other. The transverse dipole is a magnetic mode, since opposite charges accumulate on opposing edges of the cup opening, setting up a current loop at optical frequencies. This electroinductive mode has the potential for many applications. For instance, it has been shown that this mode is capable of controllably redirecting light,[30] and it has been suggested that it could have potential for realizing negative refraction index and

metamaterial applications at optical frequencies.[29] A weak magnetic mode also occurs in the axial polarization at nearly the same wavelength. Although the charge distribution associated with this mode is skewed to one side and does not appear to be the same as the transverse magnetic dipole, its electroinductive nature and similar energy suggests that the two spectral features may in fact correspond to the same mode. It is likely that it is excitable in the axial polarization in this case since retardation effects in this size regime allow the two sides of the cup to be oppositely polarized with respect to each other. Therefore the broken symmetry of the nanocup geometry allows the magnetic dipole mode to be effectively independent of polarization.

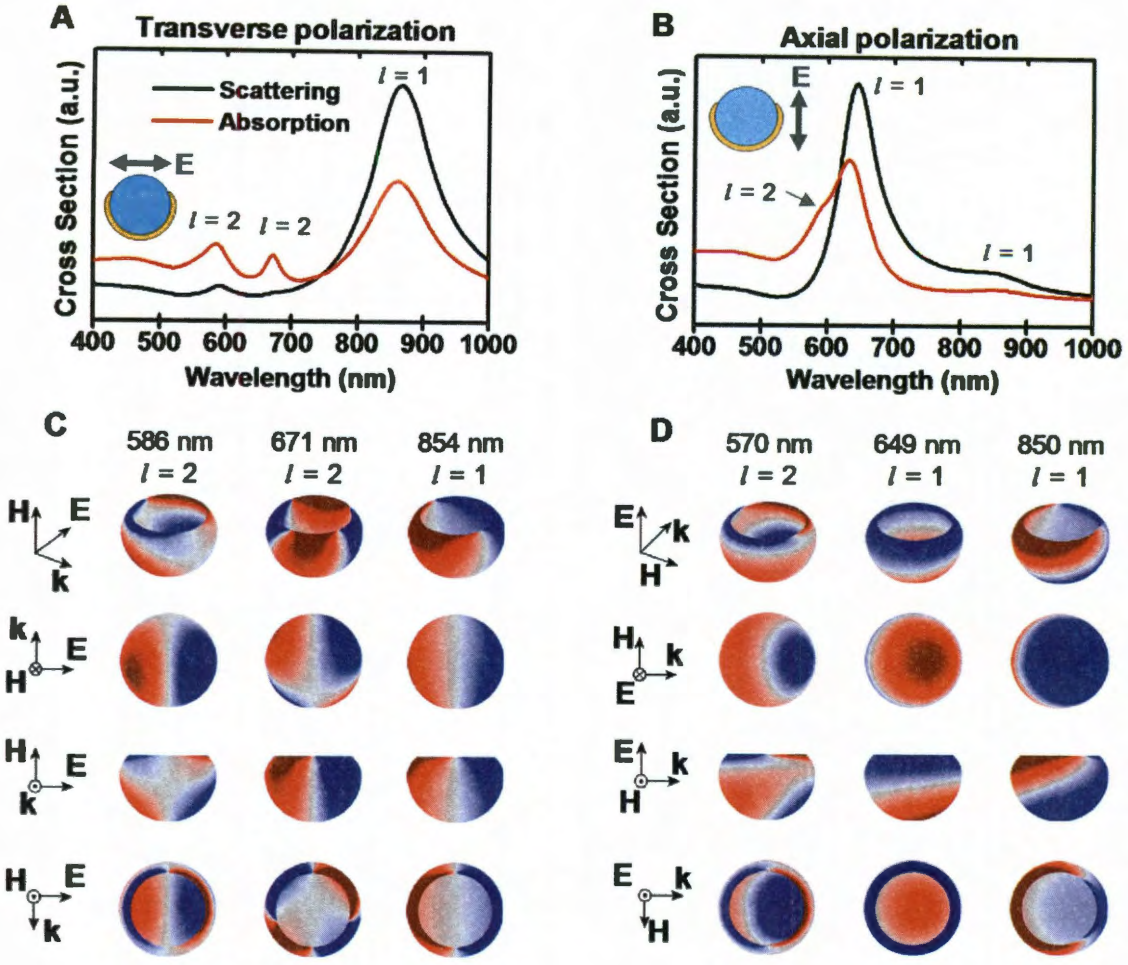

Figure 7.4. Polarization-dependent finite element method simulations for realistic nanocups (core radius = 68 nm and shell thickness = 80 nm). . (**a**) Scattering (black) and absorption (red) spectra for (**a**) transverse polarization and (**b**) axial polarization. (**c**) Surface charge plots at the specific wavelengths of the transverse spectral peaks. (**d**) Surface charge plots at the specific wavelengths of the axial spectral peaks. **E**, **H** and **k** vectors indicate the orientation of the polarization with respect to the nanocup in the four different views.

For transverse polarization, two additional peaks at 671 nm and 586 nm appear which have larger absorption cross sections than scattering cross sections, and which are therefore not observable in our dark-field measurements. The surface charge distributions reveal that both of these modes are quadrupolar (l = 2) since four distinct

charge lobes are present for each, albeit with different orientations. These two modes occur at different energies, since the broken symmetry of the nanocup allows the degeneracy of the quadrupole mode to be lifted. Interestingly, while the lifting of degeneracy for the dipole mode manifests as splitting between the two polarizations; here the two split quadrupolar modes are observable in the same, transverse polarization. While the 671 nm mode is allowed solely due to retardation effects, the 586 nm mode persists even when the nanocup size is reduced by eight times to the quasistatic limit (Fig. 7.5). This quadrupole mode (586 nm) is therefore excitable not by retardation effects, but due to the broken symmetry of the nanocup geometry. Physically, light can induce a dipolar charge separation across the rim of the nanocup while the overall mode remains characteristically quadrupolar. For axial polarization, the shoulder at 570 nm may also be identified as a quadrupolar mode, since four distinct charge lobes are evident, despite distortion from the background due to the edge of the nearby dipolar peak ($l = 1$). Here this axial quadrupole mode occurs due to retardation effects. However, it should be noted that this quadrupole is similar in energy and charge distribution to the 586 nm transverse quadrupole. In effect, these two quadrupoles are the same mode that can be excited in both polarizations due to the broken symmetry of the nanocup geometry.

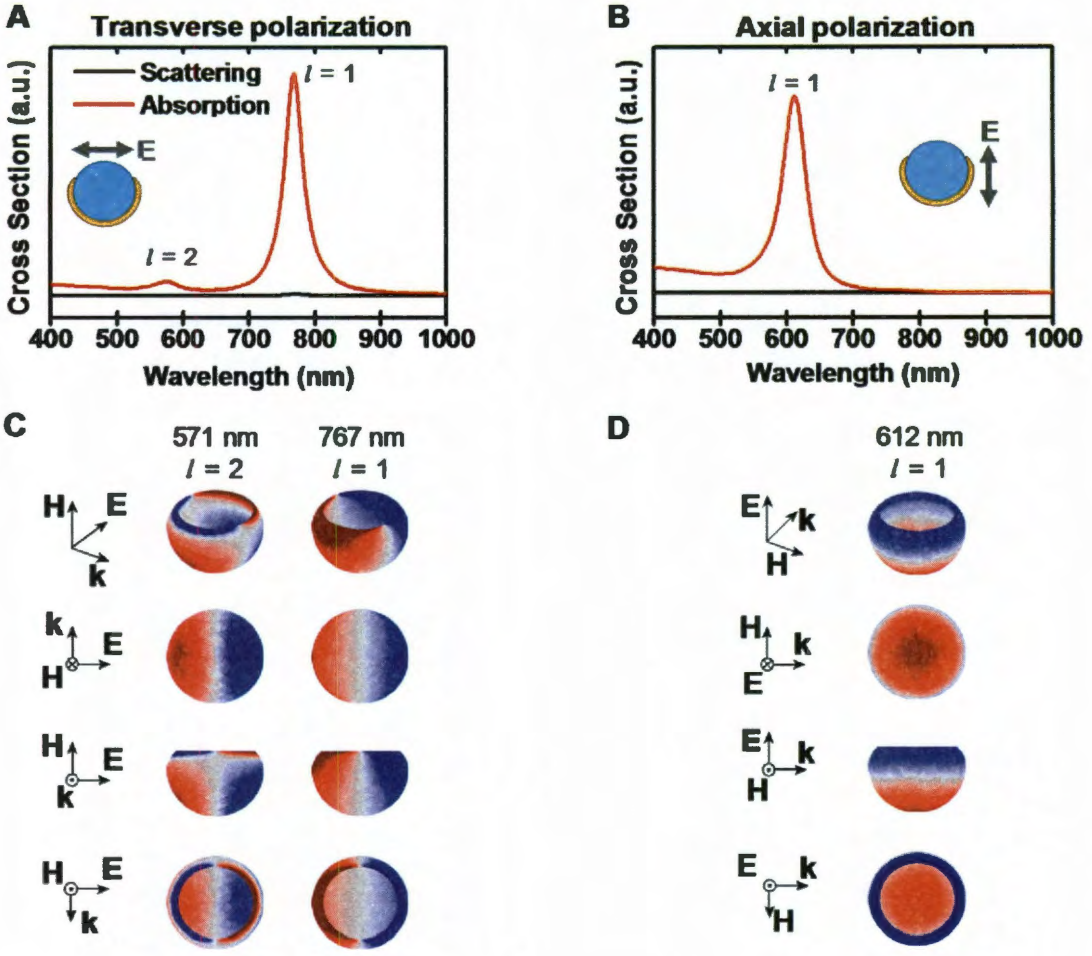

Figure 7.5. Polarization-dependent finite element method simulations for quasistatic nanocups (core radius = 8.5 nm and shell thickness = 1.5 nm). Scattering (black) and absorption (red) spectra for (**a**) transverse polarization and (**b**) axial polarization. (**c**) Surface charge plots at the specific wavelengths of the transverse spectral peaks. (**d**) Surface charge plots at the specific wavelengths of the axial spectral peaks. **E**, **H** and **k** vectors indicate the orientation of the polarization with respect to the nanocup in the four different views.

7.5 Conclusions

In conclusion, we have shown experimentally that nanoshells may be controllably reshaped using an electron beam in a water vapor environment (ESEM), thinning the top

of the shell by varying degrees to form either a nanoegg or nanocup morphology. The optical spectra of a single nanoparticle systematically modified in this manner was observed using polarization-dependent dark-field microspectroscopy, which, along with FEM simulations of these morphologies, allowed us to definitively assign the plasmon modes of a nanocup. This approach also enabled us to discriminate between the intrinsic plasmon modes of the nanocup, excitable in the quasistatic limit, and those modes excitable in larger structures due to phase retardation effects. The plasmon mode assignment obtained in this manner will be useful in developing applications of nanocups, whose plasmon modes have already been identified as having unusual and unique light-refracting properties.

Chapter 8: Bibliography

1. Barnes, W. L., Dereux, A. & Ebbesen, T. W. Surface Plasmon Subwavelength Optics. *Nature* **424**, 824-830 (2003).

2. Ozbay, E. Plasmonics: Merging Photonics and Electronics at Nanoscale Dimensions. *Science* **311**, 189-193 (2006).

3. Lal, S., Link, S. & Halas, N. J. Nano-optics from sensing to waveguiding. *Nature Photon.* **1**, 641-648 (2007).

4. Raether, H. *Surface Plasmons on Smooth and Rough Surfaces and on Gratings.* (Springer-Verlag, 1988).

5. Sanders, A. W. *et al.* Observation of Plasmon Propagation, Redirection, and Fan-Out in Silver Nanowires. *Nano Lett.* **6**, 1822-1856 (2006).

6. Bozhevolnyi, S. I., Volkov, V. S., Devaux, E., Laluet, J.-Y. & Ebbesen, T. W. Channel Plasmon Subwavelength Waveguide Components Including Interferometers and Ring Resonators. *Nature* **440**, 508-511 (2005).

7. Kelly, K. L., Coronado, E., Zhao, L. L. & Schatz, G. The Optical Properties of Metal Nanoparticles: The Influence of Size, Shape, and Dielectric Environment. *J. Phys. Chem. B* **107**, 668-677 (2003).

8. Moskovits, M. Surface-enhanced spectroscopy. *Rev. Mod. Phys.* **57**, 783-828 (1985).

9. Nie, S. & Emory, S. R. Probing Single Molecules and Single Nanoparticles by Surface-Enhanced Raman Scattering. *Science* **275**, 1102-1106 (1997).

10. Kneipp, K. *et al.* Single Molecule Detection Using Surface-Enhanced Raman Scattering (SERS). *Phys. Rev. Lett.* **78**, 1667-1670 (1997).

11. Xu, H., Bjerneld, E. J., Käll, M. & Börjesson, L. Spectroscopy of Single Hemoglobin Molecules by Surface Enhanced Raman Scattering. *Phys. Rev. Lett.* **83**, 4657 (1999).

12. Michaels, A. M., Nirmal, M. & Brus, L. E. Surface Enhanced Raman Spectroscopy of Individual Rhodamine 6G Molecules on Large Ag Nanocrystals. *J. Am. Chem. Soc.* **121**, 9932 (1999).

13. Liao, H., Nehl, C. L. & Hafner, J. H. Biomedical applications of plasmon resonant metal nanoparticles. *Nanomedicine* **1**, 201-208 (2006).

14. Shelby, R. A., Smith, D. R. & Schultz, S. Experimental Verification of a Negative Index of Refraction. *Science* **292**, 77-79 (2001).

15. Shalaev, V. M. Optical negative-index metamaterials. *Nature Photon.* **1**, 41-48 (2007).

16. Liu, N. *et al.* Three-dimensional photonic metamaterials at optical frequencies. *Nature Mater.* **7**, 31-37 (2008).

17. Atwater, H. A. & Polman, A. Plasmonics for improved photovoltaic devices. *Nature Mater.* **9**, 205-213 (2010).

18. Knight, M. W., Sobhani, H., Nordlander, P. & Halas, N. J. Photodetection with Active Optical Antennas. *Science* **332**, 702-704 (2011).

19. Michaels, A. M., Jiang, J. & Brus, L. Ag Nanocrystal Junctions as the Site for Surface-Enhanced Raman Scattering of Single Rhodamine 6G Molecules. *J. Phys. Chem. B* **104**, 11965 (2000).

20. Hao, E. & Schatz, G. C. Electromagnetic Fields Around Silver Nanoparticles And Dimers. *J. Chem. Phys.* **120**, 357-366 (2004).

21. Talley, C. E. *et al.* Surface-Enhanced Raman Scattering from Individual Au Nanoparticles and Nanoparticle Dimer Substrates. *Nano Lett.* **5**, 1569 (2005).

22. Mirin, N. A., Bao, K. & Nordlander, P. Fano Resonances in Plasmonic Nanoparticle Aggregates†. *J. Phys. Chem. A* **113**, 4028-4034 (2009).

23. Fan, J. A. *et al.* Self-Assembled Plasmonic Nanoparticle Clusters. *Science* **328**, 1135-1138 (2010).

24. Luk'yanchuk, B. *et al.* The Fano resonance in plasmonic nanostructures and metamaterials. *Nature Mater.* **9**, 707-715 (2010).

25. Hao, F. *et al.* Symmetry Breaking in Plasmonic Nanocavities: Subradiant LSPR Sensing and a Tunable Fano Resonance. *Nano Lett.* **8**, 3983-3988 (2008).

26. Hao, F., Nordlander, P., Sonnefraud, Y., Dorpe, P. V. & Maier, S. A. Tunability of Subradiant Dipolar and Fano-Type Plasmon Resonances in Metallic Ring/Disk Cavities: Implications for Nanoscale Optical Sensing. *ACS Nano* **3**, 643-652 (2009).

27. Liu, N. *et al.* Planar Metamaterial Analogue of Electromagnetically Induced Transparency for Plasmonic Sensing. *Nano Lett.* **10**, 1103-1107 (2010).

28. Sonnefraud, Y. *et al.* Experimental realization of subradiant, superradiant, and fano resonances in ring/disk plasmonic nanocavities. *ACS Nano* **4**, 1664-1670 (2010).

29. Cortie, M. & Ford, M. A plasmon-induced current loop in gold semi-shells. *Nanotechnology* **18**, 235704 (2007).

30. Mirin, N. A. & Halas, N. J. Light-Bending Nanoparticles. *Nano Lett.* **9**, 1255-1259 (2009).

31. Ye, J. *et al.* Fabrication and Optical Properties of Gold Semishells. *J. Phys. Chem. C* **113**, 3110-3115 (2009).

32. Bohren, C. F. & Huffman, D. R. *Absorption and Scattering of Light by Small Particles*. (Wiley, 1983).

33. Mie, G. Beitrage zur Optik truber Medien, speziell kolloidaler Metallosungen. *Ann. Phys.* **25**, 377-445 (1908).

34. Jin, J. *The Finite Element Method in Electromagnetics*. 2 edn, (Wiley-IEEE Press, 2002).

35. Taflove, A. & Hagness, S. C. *Computational Electrodynamics: The Finite-difference Time Domain Method.* (Artech House, 2000).

36. Prodan, E., Radloff, C., Halas, N. J. & Nordlander, P. A Hybridization Model for the Plasmon Response of Complex Nanostructures. *Science* **302**, 419-422 (2003).

37. Nordlander, P., Oubre, C., Prodan, E., Li, K. & Stockman, M. I. Plasmon Hybridization in Nanoparticle Dimers. *Nano Lett.* **4**, 899 (2004).

38. Prodan, E. & Nordlander, P. Plasmon hybridization in spherical nanoparticles. *J. Chem. Phys.* **120**, 5444-5454 (2004).

39. Oldenburg, S. J., Averitt, R. D., Westcott, S. L. & Halas, N. J. Nanoengineering of Optical Resonances. *Chem. Phys. Lett.* **288**, 243-247 (1998).

40. Brinson, B. E. *et al.* Nanoshells Made Easy: Improving Au Layer Growth on Nanoparticle Surfaces. *Langmuir* **24**, 14166-14171 (2008).

41. Jackson, J. B. & Halas, N. J. Surface-enhanced Raman scattering on tunable plasmonic nanoparticle substrates. *Proc. Natl. Acad. Sci. U.S.A.* **101**, 17930 (2004).

42. Hirsch, L. R. *et al.* Nanoshell-Mediated Near-Infrared Thermal Therapy of Tumors under Magnetic Resonance Guidance. *Proc. Natl. Acad. Sci. U.S.A.* **23**, 13549-13554 (2003).

43. Haes, A. J. & Duyne, R. P. V. A Nanoscale Optical Biosensor: Sensitivity and Selectivity of an Approach Based on the Localized Surface Plasmon Resonance Spectroscopy of Triangular Silver Nanoparticles. *J. Am. Chem. Soc.* **124**, 10596-10604 (2002).

44. Haes, A. J., Chang, L., Klein, W. L. & Duyne, R. P. V. Detection of a Biomarker for Alzheimer's Disease from Synthetic and Clinical Samples Using a Nanoscale Optical Biosensor. *J. Am. Chem. Soc.* **127**, 2264-2271 (2005).

45. McFarland, A. D. & Duyne, R. P. V. Single Silver Nanoparticles as Real-Time Optical Sensors with Zeptomole Sensitivity. *Nano Lett.* **3**, 1057-1062 (2003).

46. Sherry, L. J. *et al.* Localized Surface Plasmon Resonance Spectroscopy of Single Silver Nanocubes. *Nano Lett.* **5**, 2034-2038 (2005).

47. Fano, U. Effects of Configuration Interaction on Intensities and Phase Shifts. *Phys. Rev.* **124**, 1866 (1961).

48. Verellen, N. *et al.* Fano Resonances in Individual Coherent Plasmonic Nanocavities. *Nano Lett.* **9**, 1663-1667 (2009).

49. Mukherjee, S. *et al.* Fanoshells: nanoparticles with built-in Fano resonances. *Nano Lett.* **10**, 2694-2701 (2010).

50. Hentschel, M., Dregely, D., Vogelgesang, R., Giessen, H. & Liu, N. Plasmonic oligomers: the role of individual particles in collective behavior. *ACS Nano* **5**, 2042-2050 (2011).

51. Hentschel, M. *et al.* Transition from isolated to collective modes in plasmonic oligomers. *Nano Lett.* **10**, 2721-2726 (2010).

52. Fan, J. A. *et al.* Fano-like interference in self-assembled plasmonic quadrumer clusters. *Nano Lett.* **10**, 4680-4685 (2010).

53. Alzar, C. L. G., Martinez, M. A. G. & Nussenzveig, P. Classical analog of electromagnetically induced transparency. *Am. J. Phys* **70**, 37-41 (2002).

54. Ye, J., Dorpe, P. V., Roy, W. V., Borghs, G. & Maes, G. Fabrication, Characterization, and Optical Properties of Gold Nanobowl Submonolayer Structures. *Langmuir* **25**, 1822-1827 (2009).

55. Ye, J., Lagae, L., Maes, G., Borghs, G. & Dorpe, P. V. Symmetry Breaking induced optical properties of gold open shell nanostructures. *Opt. Express* **17**, 23765-23771 (2009).

56. Kreibig, U. & Vollmer, M. *Optical Properties of Metal Clusters.* (Springer-Verlag, 1995).

57. Sonnichsen, C., Franzl, T., Wilk, T., Plessen, G. v. & Feldmann, J. Plasmon resonances in large noble-metal clusters. *New. J. Phys.* **4**, 93 (2002).

58. Nehl, C. L. *et al.* Scattering Spectra of Single Gold Nanoshells. *Nano Lett.* **4**, 2355-2359 (2004).

59. Link, S. & El-Sayed, M. A. Size and Temperature Dependence of the Plasmon Absorption of Colloidal Gold Nanoparticles. *J. Phys. Chem. B* **103**, 4212-4217 (1999).

60. Klar, T. *et al.* Surface Plasmon Resonances in Single Metallic Nanoparticles. *Phys. Rev. Lett.* **80**, 4249-4252 (1998).

61. Sonnichsen, C. *et al.* Spectroscopy of single metallic nanoparticles using total internal reflection microscopy. *Appl. Phys. Lett.* **77**, 2949-2951 (2000).

62. Kuttge, M. *et al.* Local density of states, spectrum, and far-field interference of surface plasmon polaritons probed by cathodoluminescence. *Phys. Rev. B* **79**, 113405 (2009).

63. García de Abajo, F. J. Optical excitations in electron microscopy. *Rev. of Mod. Phys.* **82**, 209-275 (2010).

64. Mock, J. J., Barbic, M., Smith, D. R., Schultz, D. A. & Schultz, S. Shape effects in plasmon resonance of individual colloidal silver nanoparticles. *J. Chem. Phys.* **116**, 6755-6759 (2002).

65. Sonnichsen, C. *et al.* Drastic Reduction of Plasmon Damping in Gold Nanorods. *Phys. Rev. Lett.* **88**, 077402 (2002).

66. Muller, J. *et al.* Electrically controlled light scattering with single metal nanoparticles. *Appl. Phys. Lett.* **81**, 171-173 (2002).

67. Mock, J. J., Smith, D. R. & Schultz, S. Local Refractive Index Dependence of Plasmon Resonance Spectra from Individual Nanoparticles. *Nano Lett.* **3**, 485-491 (2003).

68. Prikulis, J. *et al.* Optical Spectroscopy of Single Trapped Metal Nanoparticles in Solution. *Nano Lett.* **4**, 115 (2004).

69. Gunnarsson, L. *et al.* Confined Plasmons in Nanofabricated Single Particle Pairs: Experimental Observations of Strong Interparticle Interactions. *J. Phys. Chem. B* **109**, 1079 (2005).

70. Sönnichsen, C., Reinhard, B. M., Liphardt, J. & Alivisatos, A. P. A molecular ruler based on plasmon coupling of single gold and silver nanoparticles. *Nature Biotech.* **23**, 741 (2005).

71. Nehl, C. L., Liao, H. & Hafner, J. H. Optical Properties of Star-Shaped Gold Nanoparticles. *Nano Lett.* **6**, 683-688 (2006).

72. Zsigmondy, R. A. *Properties of colloids*, <http://www.nobelprize.org/nobel_prizes/chemistry/laureates/1925/zsigmondy-lecture.pdf> (1926).

73. Murphy, D. B. *Fundamentals of Light Microscopy and Electronic Imaging.* (Wiley, 2001).

74. Link, S. & El-Sayed, M. A. Spectral Properties and Relaxation Dynamics of Surface Plasmon Electronic Oscillations in Gold and Silver Nanodots and Nanorods. *J. Phys. Chem. B* **103**, 8410 (1999).

75. Knight, M. W., Wu, Y., Lassiter, J. B., Nordlander, P. & Halas, N. J. Substrates Matter: Influence of an Adjancent Dielectric on an Individual Plasmonic Nanoparticle. *Nano Lett.* **9**, 2188-2192 (2009).

76. Xu, H., Aizpurua, J., Käll, M. & Apell, P. Electromagnetic contributions to single-molecule sensitivity in surface-enhanced Raman scattering. *Phys. Rev. E* **62**, 4318 (2000).

77. Osawa, M. Surface-Enhanced Infrared Absorption. *Top. Appl. Phys.* **81**, 163 (2001).

78. Murphy, C. J., Sau, T. K., Gole, A. & Orendorff, C. J. Surfactant-Directed Synthesis and Optical Properties of One-Dimensional Plasmonic Metallic Nanostructures. *MRS Bull.* **30**, 349-355 (2005).

79. Sun, Y. & Xia, Y. Shape-Controlled Synthesis of Gold and Silver Nanoparticles. *Science* **298**, 2176-2179 (2002).

80. Wang, H., Kundu, J. & Halas, N. J. Plasmonic Nanoshell Arrays Combine Surface-Enhanced Vibrational Spectroscopies on a Single Substrate. *Angew. Chem. Int. Ed.* **46**, 9040 (2007).

81. Maier, S. A. *et al.* Plasmonics - A Route to Nanoscale Optical Devices. *Adv. Mat.* **13**, 1501-1505 (2001).

82. Maier, S. A. *et al.* Local detection of electromagnetic energy transport below the diffraction limit in metal nanoparticle plasmon waveguides. *Nature Mater.* **2**, 229 (2003).

83. Li, K., Stockman, M. I. & Bergman, D. J. Self-Similar Chain of Metal Nanospheres as an Efficient Nanolens. *Phys. Rev. Lett.* **91**, 227402 (2003).

84. Tamaru, H., Kuwata, H., Miyazaki, H. T. & Miyano, K. Resonant light scattering from individual Ag nanoparticles and particle pairs. *Appl. Phys. Lett.* **80**, 1826 (2002).

85. Rechberger, W. *et al.* Optical properties of two interacting gold nanoparticles. *Opt. Commun.* **220**, 137 (2003).

86. Atay, T., Song, J.-H. & Nurmikko, A. V. Strongly Interacting Plasmon Nanoparticles Pairs: From Dipole-Dipole Interaction to Conductively Couples Regime. *Nano Lett.* **4**, 1627 (2004).

87. Reinhard, B. M., Siu, M., Agarwal, H., Alivisatos, A. P. & Liphardt, J. Calibration of Dynamic Molecular Rulers Based on Plasmon Coupling between Gold Nanoparticles. *Nano Lett.* **5**, 2246 (2005).

88. Wang, H. & Halas, N. J. Plasmonic Nanoparticle Heterodimers in a Semiembedded Geometry Fabricated by Stepwise Upright Assembly. *Nano Lett.* **6**, 2945 (2006).

89. Ringler, M. *et al.* Moving Nanoparticles with Raman Scattering. *Nano Lett.* **7**, 2753 (2007).

90. Jain, P. K., Huang, W. & El-Sayed, M. A. On the Universal Scaling Behavior of the Distance Decay of Plasmon Coupling in Metal Nanoparticle Pairs: A Plasmon Ruler Equation. *Nano Lett.* **7**, 2080-2088 (2007).

91. Brandl, D. W., Oubre, C. & Nordlander, P. Plasmon hybridization in nanoshell dimers. *J. Chem. Phys.* **123**, 024701 (2005).

92. Romero, I., Aizpurua, J., Bryant, G. W. & Abajo, F. J. G. d. Plasmons in nearly touching metallic nanoparticles: singular response in the limit of touching dimers. *Opt. Express* **14**, 9988 (2006).

93. Danckwerts, M. & Novotny, L. Optical Frequency Mixing at Coupled Gold Nanoparticles. *Phys. Rev. Lett.* **98**, 026104 (2007).

94. Sun, Y. & Xia, Y. Increased Sensitivity of Surface Plasmon Resonance of Gold Nanoshells Compared to That of Gold Solid Colloids in Response to Environmental Changes. *Anal. Chem.* **74**, 5297 (2002).

95. Zhao, J. *et al.* Alkanethiol Mediated Release of Surface Bound Nanoparticles Fabricated by Nanosphere Lithography. *Mat. Res. Soc. Symp. Proc.* **900E**, 0900-O0913-0908.0901-0900-O0913-0908.0906 (2006).

96. Sardar, R., Heap, T. B. & Shumaker-Parry, J. S. Versatile Solid Phase Synthesis of Gold Nanoparticle Dimers Using an Asymmetric Functionalization Approach. *J. Am. Chem. Soc.* **129**, 5356 (2007).

97. Malynych, S., Luzinov, I. & Chumanov, G. Poly(Vinyl Pyridine) as a Universal Surface Modifier for Immobilization of Nanoparticles. *J. Phys. Chem. B* **106**, 1280-1285 (2002).

98. Wang, H. *et al.* Symmetry breaking in individual plasmonic nanoparticles. *Proc. Natl. Acad. Sci. U.S.A.* **103**, 10856-10860 (2006).

99. Garcia de Abajo, F. J. & Howie, A. Relativistic Energy Loss and Electron-Induced Photon Emission in Inhomogeneous Dielectrics. *Physical Review Letters* **80**, 5180-5183 (1998).

100. Palik, E. D. *Handbook of Optical Constants of Solids.* (Academic Press, 1985).

101. Johnson, P. B. & Christy, R. W. Optical Constants of the Noble Metals. *Phys. Rev. B* **6**, 4370-4379 (1972).

102. Porter, M. D., Bright, T. B., Allara, D. L. & Chidsey, C. E. D. *J. Am. Chem. Soc.* **109**, 3559 (1987).

103. Lal, S., Grady, N. K., Goodrich, G. P. & Halas, N. J. Profiling the Near Field of a Plasmonic Nanoparticle with Raman-Based Molecular Rulers. *Nano Lett.* **6**, 2338-2343 (2006).

104. Rycenga, M., Camargo, P. H. C., Li, W., Moran, C. H. & Xia, Y. N. Understanding the SERS Effects of Single Silver Nanoparticles and their Dimers, One at a Time. *J. Phys. Chem. Lett.* **1**, 696-703 (2010).

105. Brown, L. V., Sobhani, H., Lassiter, J. B., Nordlander, P. & Halas, N. J. Heterodimers: Plasmonic Properties of Mismatched Nanoparticle Pairs. *ACS Nano* **4**, 819-832 (2010).

106 Pakizeh, T. & Kall, M. Unidirectional Ultracompact Optical Nanoantennas. *Nano Lett.* **9**, 2343-2349 (2009).

107. Mastroianni, A. J., Claridge, S. A. & Alivisatos, A. P. Pyramidal and Chiral Groupings of Gold Nanocrystals Assembled Using DNA Scaffolds. *J. Am. Chem. Soc.* **131**, 8455-8459 (2009).

108. Li, Z. P., Shegai, T., Haran, G. & Xu, H. X. Multiple-Particle Nanoantennas for Enormous Enhancement and Polarization Control of Light Emission. *ACS Nano* **3**, 637-642 (2009).

109. Shegai, T., Li, Z. P., Dadosh, T., Zhang, Z. Y. & Xu, H. X. Managing Light Polarization via Plasmon-Molecule Interactions within an Asymmetric Metal Nanoparticle Trimer. *Pro. Nat. Acad. Sci. U.S.A.* **105**, 16448-16453 (2008).

110. Brandl, D. W., Mirin, N. A. & Nordlander, P. Plasmon modes of nanosphere trimers and quadrumers. *Journal of Physical Chemistry B* **110**, 12302-12310, doi:10.1021/jp0613485 (2006).

111. Zhang, Z. *et al.* Manipulating Nanoscale Light Fields with the Asymmetric Bowtie Nano-Colorsorter. *Nano Letters* **9**, 4505-4509, doi:10.1021/nl902850f (2009).

112. Urzhumov, Y. A. *et al.* Plasmonic nanoclusters: a path towards negative-index metafluids. *Opt. Express* **15**, 14129-14145 (2007).

113. Chen, H. J. *et al.* Plasmon Coupling in Clusters Composed of Two-Dimensionally Ordered Gold Nanocubes. *Small* **5**, 2111-2119 (2009).

114. Gomez, D. E., Vernon, K. C. & Davis, T. J. Symmetry effects on the optical coupling between plasmonic nanoparticles with applications to hierarchical structures. *Phys. Rev. B.* **81**, 075414 (2010).

115. Liu, H. *et al.* Coupled magnetic plasmons in metamaterials. *Physica Status Solidi B-Basic Solid State Phys.* **246**, 1397-1406 (2009).

116. Hossain, M. K., Huang, G. G., Kaneko, T. & Ozaki, Y. Surface-enhanced Raman scattering and plasmon excitations from isolated and elongated gold nanoaggregates. *Chem.Phys. Lett.* **477**, 130-134 (2009).

117. Jin, R. Nanoparticle Clusters Light Up in SERS. *Angew. Chem. Int. Ed.* **49**, 2826-2829 (2010).

118. Liu, N., Kaiser, S. & Giessen, H. Magnetoinductive and Electroinductive Coupling in Plasmonic Metamaterial Molecules. *Adv. Mater.* **20**, 4521-4525 (2008).

119. Liu, N., Liu, H., Zhu, S. N. & Giessen, H. Stereometamaterials. *Nature Photonics* **3**, 157-162, doi:10.1038/nphoton.2009.4 (2009).

120. Chen, Y. T., Chern, R. L. & Lin, H. Y. Multiple Fano resonances in metallic arrays of asymmetric dual stripes. *Appl. Opt.* **49**, 2819-2826 (2010).

121. Burrows, C. P. & Barnes, W. L. Large spectral extinction due to overlap of dipolar and quadrupolar plasmonic modes of metallic nanoparticles in arrays. *Opt. Express* **18**, 3187-3198 (2010).

122. Yang, Z. J., Zhang, Z. S., Zhang, W., Hao, Z. H. & Wang, Q. Q. Twinned Fano resonances induced by hybridized plasmons in Au-Ag nanorod heterodimers. *Appl. Phys. Lett.* **96**, 13113 (2010).

123. Fedotov, V. A. *et al.* Spectral Collapse in Ensembles of Metamolecules. *Phys. Rev. Lett.* **104**, 223901 (2010).

124. Su, X. R. *et al.* Plasmonic interferences and optical modulations in dark-bright-dark plasmon resonators. *Appl. Phys. Lett.* **96**, 743113 (2010).

125. Pakizeh, T., Langhammer, C., Zoric, I., Apell, P. & Kall, M. Intrinsic Fano Interference of Localized Plasmons in Pd nanoparticles. *Nano Lett.* **9**, 882-886 (2009).

126. Le, F. *et al.* Metallic nanoparticle arrays: A common substrate for both surface-enhanced Raman scattering and surface-enhanced infrared absorption. *ACS Nano* **2**, 707-718 (2008).

127. Jonsson, M. P., Dahlin, A. B., Jonsson, P. & Hook, F. Nanoplasmonic biosensing with focus on short-range ordered nanoholes in thin metal films. *Biointerphases* **3**, FD30-FD40 (2008).

128. Vo-Dinh, T. *et al.* Plasmonic Nanoparticles and Nanowires: Design, Fabrication and Application in Sensing. *J. of Phys. Chem. C* **114**, 7480-7488 (2010).

129. Mayer, K. N., Hao, F., Lee, S. H., Nordlander, P. & Hafner, J. H. A Single Molecule Immunoassay by Localized Surface Plasmon Resonance. *Nanotechnology* **21**, 255503 (2010).

130. El-Kashef, H. The necessary requirements imposed on polar dielectric laser dye solvents. *Physica B* **279**, 295-301 (2000).

131. Schuller, J. A. *et al.* Plasmonics for Extreme Light Concentration and Manipulation. *Nature Mater.* **9**, 193-204 (2010).

132. Liu, N., Mesch, M., Weiss, T., Hentschel, M. & Giessen, H. Infrared perfect absorber and its application as plasmonic sensor. *Nano Lett.* **10**, 2342-2348 (2010).

133. Kim, S. *et al.* High-harmonic generation by resonant plasmon field enhancement. *Nature* **453**, 757-760 (2008).

134. Zhang, Y., Grady, N. K., Ayala-Orozco, C. & Halas, N. J. Three-Dimensional Nanostructures as Highly Efficient Generators of Second Harmonic Light. *Nano Lett.* **11**, 5519-5523 (2011).

135. Munday, J. N. & Atwater, H. A. Large integrated absorption enhancement in plasmonic solar cells by combining metallic gratings and antireflection coatings. *Nano Lett.* **11**, 2195-2201 (2011).

136. Zhang, S., Genov, D. A., Wang, Y., Liu, M. & Zhang, X. Plasmon-Induced Transparency in Metamaterials. *Phys. Rev. Lett.* **101**, 047401 (2008).

137. Liu, N. *et al.* Plasmonic analogue of electromagnetically induced transparency at the Drude damping limit. *Nature. Mater.* **8**, 758-762 (2009).

138. Artar, A., Yanik, A. A. & Altug, H. Multispectral Plasmon Induced Transparency in Coupled Meta-Atoms. *Nano Lett.* **11**, 1685-1689 (2011).

139. Bao, K., Mirin, N. a. & Nordlander, P. Fano resonances in planar silver nanosphere clusters. *Appl. Phys. A* **100**, 333-339 (2010).

140. Dregely, D., Hentschel, M. & Giessen, H. Excitation and tuning of higher-order fano resonances in plasmonic oligomer clusters. *ACS Nano* **5**, 8202-8211 (2011).

141. Yan, B., Boriskina, S. V. & Reinhard, B. M. Optimizing Gold Nanoparticle Cluster Configurations (n < 7) for Array Applications. *J. Phys. Chem. C* **115**, 4578-4583 (2011).

142 Rahmani, M. *et al.* Influence of Plasmon Destructive Interferences on Optical Properties of Gold Planar Quadrumers. *Nanotechnology* **22**, 245204 (2011).

143. Rahmani, M. *et al.* Generation of Pronounced Fano Resonances and Tuning of Subwavelength Spatial Light Distribution in Plasmonic Pentamers. *Opt. Express* **19**, 4949-4956 (2011).

144. Alonso-Gonzalez, P. *et al.* Real Space Mapping of Fano Interference in Plasmonic Metamolecules. *Nano Lett.* **11**, 3922-3926 (2011).

145. Artar, A., Yanik, A. A. & Altug, H. Directional Double Fano Resonances in Plasmonic Hetero-Oligomers. *Nano Lett.* **11**, 3694-3700 (2011).

146. Gallinet, B. & Martin, O. J. F. Ab Initio Theory of Fano Resonances in Plasmonic Nanostructures and Metamaterials. *Phys. Rev. B* **83**, 235427 (2011).

147. Gallinet, B. & Martin, O. J. F. Influence of Electromagnetic Interactions on the Lineshape of Plasmonic Fano Resonances. *ACS Nano* **5**, 8999-9008 (2011).

148. Giannini, V., Francescato, Y., Amrania, H., Phillips, C. C. & Maier, S. A. Fano Resonances in Nanoscale Plasmonic Systems: A Parameter-Free Modeling Approach. *Nano Lett.* **11**, 2835-2840 (2011).

149. Lassiter, J. B. *et al.* Fano resonances in plasmonic nanoclusters: geometrical and chemical tunability. *Nano Lett.* **10**, 3184-3189 (2010).

150. Chen, H. *et al.* Observation of the Fano Resonance in Gold Nanorods Supported on High-Dielectric-Constant Substrates. *ACS Nano* **5**, 6754-6763 (2011).

151. Yamamoto, N., Araya, K. & García de Abajo, F. Photon emission from silver particles induced by a high-energy electron beam. *Phys. Rev. B* **64**, 205419 (2001).

152. Vesseur, E. J. R., de Waele, R., Kuttge, M. & Polman, A. Direct observation of plasmonic modes in au nanowires using high-resolution cathodoluminescence spectroscopy. *Nano Lett.* **7**, 2843-2846 (2007).

153. Frimmer, M., Coenen, T. & Koenderink, A. F. Signature of a Fano-resonance in a plasmonic meta-molecule's local density of optical states. *arXiv:1109.5407v1* (2011).

154. Wang, H., Brandl, D. W., Nordlander, P. & Halas, N. J. Plasmonic Nanostructures: Artificial Molecules. *Acc. Chem. Res.* **40**, 53-62 (2007).

155. Pendry, J. B. Negative Refraction Makes a Perfect Lens. *Phys. Rev. Lett.* **85**, 3966-3969 (2000).

156. Linden, S. *et al.* Magnetic Response of Metamaterials at 100 Terahertz. *Science* **306**, 1351-1353 (2004).

157. Shalaev, V. M. *et al.* Negative index of refraction in optical metamaterials. *Opt. Lett.* **30**, 3356-3358 (2005).

158. Grigorenko, A. N. *et al.* Nanofabricated media with negative permeability at visible frequencies. *Nature* **438**, 17-20 (2005).

159. Dolling, G., Enkrich, C., Wegener, M., Soukoulis, C. M. & Linden, S. Simultaneous Negative Phase and Group Velocity of Light in a Metamaterial. *Science* **312**, 892-894 (2006).

160. Dolling, G., Wegener, M., Soukoulis, C. M. & Linden, S. Negative-index metamaterial at 780 nm wavelength. *Opt. Lett.* **32**, 53-55 (2007).

161. Soukoulis, C. M., Linden, S. & Wegener, M. Negative Refraction Index at Optical Wavelength. *Science* **315**, 47-49 (2007).

162. Hao, F., Nehl, C. L., Hafner, J. H. & Nordlander, P. Plasmon resonances of a gold nanostar. *Nano Letters* **7**, 729-732 (2007).

163. Sarychev, A. K., Shvetz, G. & Shalaev, V. M. Magnetic plasmon resonance. *Phys. Rev. E* **73**, 036609 (2006).

164. Shumaker-Parry, J. S., Rochholz, H. & Kreiter, M. Fabrication of Crescent-Shaped Optical Antennas. *Adv. Mater.* **17**, 2131-2134 (2005).

165. Wu, Y. & Nordlander, P. Plasmon hybridization in nanoshells with a nonconcentric core. *J. Chem. Phys.* **125**, 124708 (2006).

166. Wang, H., Brandl, D. W., Le, F., Nordlander, P. & Halas, N. J. Nanorice: A Hybrid Plasmonic Nanostructure. *Nano Lett.* **6**, 827-832 (2006).

167. Knight, M. W. & Halas, N. J. Nanoshells to nanoeggs to nanocups: optical properties of reduced symmetry core-shell nanoparticles beyond the quasistatic limit. *New J. Phys.* **10**, 105006 (2008).

168. Bukasov, R. & Shumaker-Parry, J. S. Highly Tunable Infrared Extinction Properties of Gold Nanocrescents. *Nano Lett.* **7**, 1113-1118 (2007).

169. Nordlander, P. & Prodan, E. Plasmon Hybridization in Nanoparticles near Metallic Surfaces. *Nano Lett.* **4**, 2209-2213 (2004).

170. Thiel, B. L. & Toth, M. Secondary electron contrast in low-vacuum/environmental scanning electron microscopy of dielectrics. *J. Appl. Phys.* **97**, 051101 (2005).

171. Randolph, S. J., Fowlkes, J. D. & Rack, P. D. Focused, Nanoscale Electron-Beam-Induced Deposition and Etching. *Crit. Rev. in Solid State and Mater. Sci.* **31**, 55-89 (2006).

172. Utke, I., Hoffman, P. & Melngailis, J. Gas-assisted focused electron beam and ion beam processing and fabrication. *J. Vac. Sci. Technol. B* **26**, 1197-1276 (2008).

173. Toth, M. *et al.* Nanostructure Fabrication by Ultra-High-Resolution Environmental Scanning Electron Microscopy. *Nano Lett.* **7**, 525-530 (2007).

174. Lobo, C. J., Toth, M., Wagner, R., Thiel, B. L. & Lysaght, M. High resolution radially symmetric nanostructures from simultaneous electron beam induced etching and deposition. *Nanotechnology* **19**, 025303 (2008).

175. Lassiter, J. B. *et al.* Close Encounters between Two Nanoshells. *Nano Lett.* **8**, 1212-1218 (2008).

176. Zuloaga, J., Prodan, E. & Nordlander, P. Quantum Description of the Plasmon Resonances of a Nanoparticle Dimer. *Nano Letters* **9**, 887-891 (2009).

177. Landau, L. D., Lifshitz, E. M. & Pitaevskii, L. P. *Electrodynamics of Continuous Media*. 2 edn, Vol. 8 (Pergamon Press, 1984).